Computational Studies of Actinide Adsorption on Two-Dimensional Materials

By Payal

A Thesis Submitted to the Faculty of Graduate Studies of the

University of Manitoba in Partial Fulfillment of the

Requirements of the Degree of

Master of Science

Department of Chemistry

University of Manitoba

Winnipeg, Manitoba

Table of Contents

List of Figures

List of Tables

List of Abbreviations

2D	Two-Dimensional
CNT	Carbon Nanotubes
GO	Graphene Oxide
DFT	Density Functional Theory
FET	Field Effect Transistors
HOMO	Highest Occupied Molecular Orbital
LUMO	Lowest Unoccupied Molecular Orbital
U	Uranium
Np	Neptunium
Pu	Plutonium
ADF	Amsterdam Density Functional
PWSCF	Plane-Wave Self-Consistent Field
QM	Quantum-Mechanical
PES	Potential Energy Surface
HF	Hartree-Fock
MO	Molecular Orbital
SCF	Self-Consistent Field
CI	Configuration Interaction
LDA	Local Density Approximation
HEG	Homogeneous Electron Gas Model
GGA	Generalized Gradient Approximation
PBE	Perdew Burke Ernzerhof
PW	Plane Wave
TPSS	Tao-Perdew-Staroverov-Scuseria
B3LYP	Becke 3-parameter Lee–Yang–Parr
STO	Slater-Type Orbitals
GTO	Gaussian-Type Orbitals
AO	Atomic Orbitals
SZ	Single Zeta

DZ	Double Zeta
TZ	Triple Zeta
QZ	Quadruple Zeta
ZORA	Zero-Order Regular Approximation
ECP	Effective Core Potential
PP	Pseudopotentials
PCM	Polarized Continuum Model
COSMO	Conductor Like Screening Model
PAW	Projector Augmented Wave
US	Ultra-Soft
MBO	Mayer Bond Order
Ac	Actinides
TZ2P	Triple-ζ Double Polarized
QTAIM	Quantum Theory of Atoms In Molecules
PBC	Periodic Boundary Conditions
vdW	van der Waals

Abstract

First-principles calculations were used to investigate previously unexplored adsorption of actinide (Ac) complexes with environmentally relevant ligands on a silicene, germanene, and borophene surface by using density functional theory to determine the geometrical, energetic and electronic properties. Three types of ligands for each central metal atom are considered: OH^-, NO_3^- and CO_3^{2-} with common oxo ligands in all cases. Two types of models, cluster and periodic models, have been considered to include the short- and long-range effects for silicene and germanene. For borophene, the comparison between line-defective planar and buckled phases has been done.

Among different complexes, carbonate complexes show the strongest adsorption followed by hydroxide and nitrate. Calculations were done in the gas phase and water solvent for silicene and germanene surface. Based on the adsorption energy, for the CO_3^{2-} and OH^- ligands, the bond position between two Si atoms in the silicene sheet is the most strongly adsorbed site in the cluster model for silicene whereas in the periodic model these complexes exhibit strong binding on the Si atom of the silicene surface. The Ac-complexes with the NO_3^- ligand show strong affinity at the hollow space at the center of a hexagonal ring of silicene in both models. The H-site is most favorable for the binding of complexes on germanene cluster whereas, these sites vary in the periodic model. Electronic structure and density of states calculations show that the contribution of the nitrate complexes is small near the Fermi level but it is larger for the carbonate complexes in silicene's case.

All the possible adsorption sites for both types of borophene have been investigated for each adsorbate. Comparing the different actinides, periodic trends were established which indicate strong affinity in case of Pu complexes as compared to Np and U complexes. The presence of buckling in borophene contributes towards the strength of adsorption, thus, buckled borophene is a highly suitable candidate for adsorption of actinide complexes in comparison to planar borophene.

The calculated results reveal the presence of strong interactions due to the formation of chemical bonds between Si/ B and the oxo ligand of the adsorbate which leads to the reduction of the central actinide metal atom. Such type of bonding lacks on the germanene surface.

Acknowledgements

Foremost, I would like to express my sincere gratitude to the **Almighty** from the core of my heart who enabled me to successfully complete this work.

I would like to express the deepest appreciation towards my supervisor Dr. Georg Schreckenbach, for his financial support, constant encouragement, sharp interest, and highly creative supervision throughout the course of this work. Without his guidance and persistant help this thesis and work would not have been possible.

I would also like to thank my advisory committee Dr. Scott Kroeker, and Dr. Robert Stamps for their productive involvement, advice, criticism and support during the work towards this thesis.

In addition, a thank you to all my lab mates, Xiaobin, Saumya, Yang Gao, Laura and Varathan, for their constant inspiration and help. I am also grateful to Dr. Grigory Shamov, the former member of Dr. Schreckenbach group for the invaluable technical support. I would like to thank Dr. James Xidos and Dr. Thaneshwor P. Kaloni for fruitful discussions.

It is my privilege to thank my fiancé Nishant Kalia and my family, for rendering me love, encouragement and moral support during my research period.

Chapter 1: Introduction

1.1 Background and motivation

Over the past few decades, two-dimensional (2D) materials are rising stars on the horizon of materials science. 2D materials are crystalline materials composed of a single atomic plane whereas hundreds of such planes stacked together should be referred to as a 3D material. The research area of 2D materials has occupied a position at the crossroad of chemistry, physics, and material sciences. The "birth" of the 2D materials field is connected to the discovery of fullerene (C_{60}) in 1985 by Kroto and his coworkers.[1] In 1991, carbon nanotubes (CNT) were discovered by Iijima[2], while the isolation of a flat monolayer of sp^2-bonded carbon atoms packed tightly in a 2D honeycomb lattice, from graphite, was achieved by two researchers of the University of Manchester, Prof. Andre Geim and Prof. Konstantin Novoselov, in 2004.[3,4] This material was named ‘Graphene'. More than 50 years ago, it had been proposed theoretically material with no actual existence in the free state.[3,5] Graphene was considered highly unstable in terms of forming curved structures such as fullerenes and nanotubes but the unexpected occurred and the free-standing graphene was found, thus, the vintage model turned into reality. Immediately after the confirmation of the presence of massless charge carriers in graphene, the ‘race’ began.[6,7]

Since graphene’s discovery, a wide range of 2D materials have been predicted theoretically and the exploration of alternative 2D materials that can be easily integrated with the current generation of electronic technologies has been increased experimentally as well.[5,8] The reason behind the immense attention of researchers on this particular field is due to the extraordinary physical and chemical properties of graphene such as exceptional electrical conductivity[9], thermal[10],

mechanical[11], optical properties[12] and the large surface area, thus making it highly suitable for super-capacitors[13], bio-medical applications such as precise biosensing through graphene-quenched fluorescence, graphene-enhanced cell differentiation and growth, and graphene-assisted laser desorption/ionization for mass spectrometry[14], as sorbent or photocatalytic materials for environmental decontamination, as building blocks for next-generation water treatment and desalination membranes, and as electrode materials for contaminant monitoring or removal[15] and other green energy devices. Further, one of the most popular approaches to graphene-based nanomaterials is to use graphene oxide (GO), due to its lower production costs. The oxidized form of graphene sheets consists of high density of oxygen functional groups such as carboxyl, hydroxyl, carbonyl, and epoxy in the carbon lattice.[16] It has been reported that the oxidation of the graphite structure results in an increase in interlayer distance from 0.34 nm to 0.65 nm, thus decreasing the energy required to separate the graphene layers.[17] Many other applications of graphene are mentioned in **Figure 1.1**, where the geometrical structure of 2D graphene is also shown.

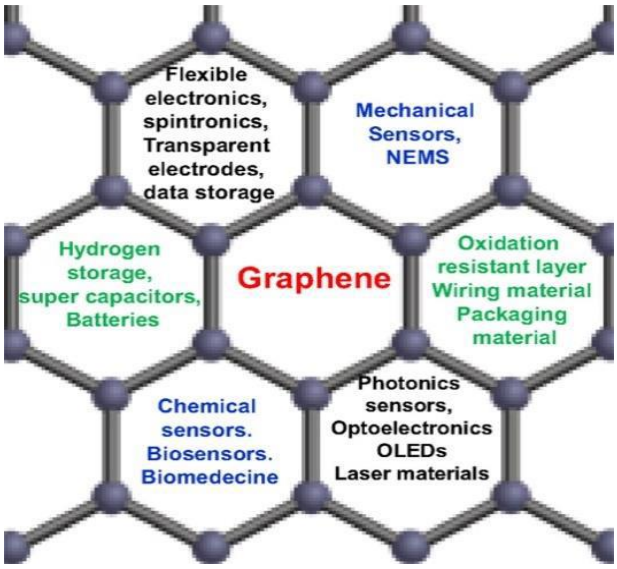

Figure 1.1 depicts some of the potential applications of graphene[18].

In recent years, the elemental sheets of the neighboring atoms of C such as Si and Ge in the form of silicene and germanene respectively have emerged as strong candidates in the domain of 2D materials.[19,20] With the experimental studies for well-defined fabrication of these 2D sheets still in their infancy, several theoretical studies are assessing their fundamental properties. In line with the continuous advances of locating and fabricating the 2D materials, borophene came into picture recently, when 2D boron sheets where characterized both experimentally and theoretically.[21,22] Detail of the studies done on these three types of 2D materials (silicene, germanene, and borophene) will be discussed in the following.

Silicene - The outstanding properties and fruitful results for graphene inspired extraordinary efforts to explore other materials that can form 2D layers such as transition metal oxides, silicon, germanium, etc. Among them, 'silicene' (Figure 1.2) which is a one-atom-thick silicon sheet is a prominent one as its building block is from the same group as carbon in the periodic table (group 14). Theory predicted similar properties for silicene as for graphene such as the presence of charge carriers which behave like massless Dirac Fermions and various other physical properties which makes it relatively easy to use the material within silicon-based electronics[23]. In 1994, theoretical studies by Takeda and Shiraishi demonstrated the 2D Si analogue of graphite and discussed the planarity of Si by the first-principle calculations[24]. Later in 2007, the name "silicene" was given by Guzmán-Verri and Lew Yan Voon[25], who showed that silicene is essentially a zero-gap semiconductor (very small, finite gap). It wasn't until 2009 that silicene with the presence of buckling in the structure was suggested dynamically stable by ab initio molecular dynamics simulations on the basis of Density functional theory (DFT)[26]. It was found that there is a presence of a low buckled hexagonal structure where half of the sublattices are above the plane which is not the case in graphene. Thus, silicene has a two-dimensional honeycomb lattice with a buckling

height (defined as the vertical distance between two sub-lattices) of 0.44Å which differentiates it from graphene[23]. This buckling is quite advantageous, as it results in tunability of the bandgap by applying an external field without any chemical modification. Growth of silicene nano-ribbons has been observed experimentally on Ag(110)[27], Ag(111)[28], Ir(111)[29]. Attempts at isolating a free-standing silicene sheet have so far been unsuccessful because of the absence of a naturally layered silicon allotrope structure analogous to graphite. In spite of the differences in the structure of silicene and graphene, the former has a similar band structure like graphene thus, the π and π^* bands cross linearly at the Fermi level (E_F), forming the famous "Dirac cone" at the symmetric point *K* in the reciprocal space[30]. Such dispersions at the Fermi level makes them both equivalent in terms of electronic properties[31]. Also, silicene has better tunability of the band gap which is highly useful for operating Field Effect Transistors (FET) at room temperature[32], and much stronger spin-orbital coupling than graphene because of the buckled structure and heavier atoms in silicene has been reported[33]. The stability of the silicene lattice up to a strain of 17% has been reported by the study of vibrational properties from phonon dispersion calculations[34]. Thus, the theoretical predictions of silicene are slowly turning into experimental observations.

Germanene – In 2009, after the impressive rise of graphene , another member from group 14 in the periodic table, Ge, was predicted to form a 2D material called germanene (Figure 1.2). In the same year, first-principle calculations reported a low buckled stable structure for germanene similar to silicene[26]. Although, the first quantum mechanical ab initio calculations were done by Takeda and Shiraishi on graphite-like germanium sheets who concluded it as a 'semi-metal' from their energy band structure investigation[35]. The variation in the structures of graphene and its cousins silicene and germanene is attributed to orbital hybridization whereby in graphene, a carbon atom forms three bonds with adjacent carbons with sp^2 hybridization thus leaving the p_z orbital

half occupied. π-bonds are formed by the coupling of the p_z orbitals and there is a short distance between C—C atoms, hence, strong π-bonding. Due to the large atomic radii of Si and Ge as compared to C, the p_z overlap is comparatively less effective and, therefore, there is weak π-bonding in silicene and germanene. Despite this, the bonding in silicene and germanene is stable because of puckering-induced dehybridization and thus, the p_z orbital overlaps with an s orbital[34,36]. The buckling, Δ, has been reported in the range of 0.64-0.74 Å for germanene by DFT studies[37]. Just like for silicene, freestanding germanene has not been isolated yet but the hydrogenated form of germanene was fabricated in 2013 by using wet chemistry,[38] and later, the growth of a germanene layer on Pt(111)[39] on Au(111)[40] was reported in 2014. Just like in the case of silicene, germanene has stronger spin-orbital coupling than graphene due to its larger atomic number and buckled structure. The gap opened by strong spin-orbit coupling in buckled germanene has been reported to be approximately 24 meV i.e. much larger than for graphene (<0.05 meV) as well as silicene (1.55 meV) thus making it an efficient candidate for showing the Quantum Spin Hall effect at experimentally approachable temperatures[41].

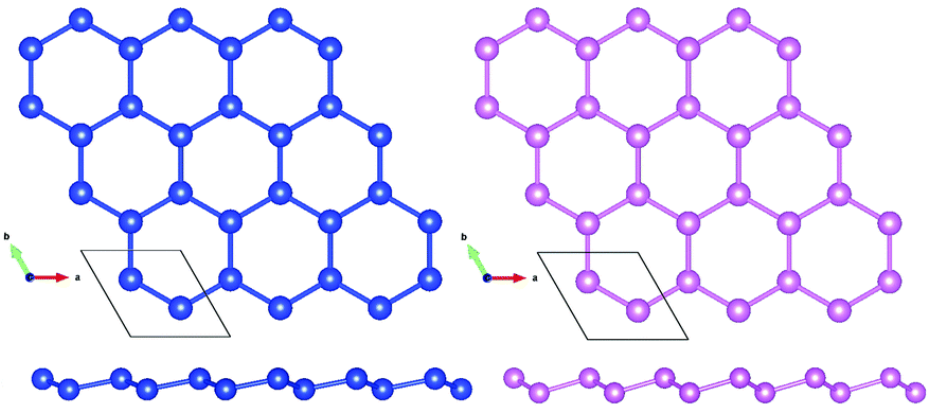

Figure 1.2 Ball and stick model (top view and side view) for silicene and germanene[42].

Borophene – In recent years, borophene has joined the family of 2D materials. Boron, a nearest neighbor to carbon in the periodic table, shows many properties similar to the carbon atom such as the flexibility to have sp^2 hybridization, small covalent radius, planar structures, etc., thus, making it efficient to have a graphene-like structure. Theoretical studies have shown the existence of borophene[43] (Figure 1.3) but there has been no experimental proof of it until 2015, when borophene was grown under ultra-high vacuum conditions on an Ag (111) substrate[44]. The electronic structure of freestanding borophene is predicted to have anisotropic metallic character[44], however, borophene has not been seen in isolated form yet. In boron ($1s^2\ 2s^2\ 2p^1$) there is a lower number of electrons than atomic orbitals. Hence, it is electron-deficient and there are not enough electrons to form chemical bonds as in the case of graphene (two-centered two-electron). So, the coexistence of localized two-centered two-electron and delocalized multicenter two-electron bonds (i.e. mc-2e) is essential for the stability of boron crystals[45]. These results made 2D boron synthesis more challenging, but this property of boron led to many nanoscopic crystals and a wide variety of complexes with other elements. In 2014, the boron cluster B_{36} with a hexagonal hole at the center was found to have a more stable quasi-planar structure as compared to the other types, for example, B_{22}, B_{24}, because of the large HOMO-LUMO gap (Highest occupied molecular orbital – lowest unoccupied molecular orbital)[46]. Recently in 2017, the electronic properties of boron sheets have been investigated and the presence of a gapless Dirac cones was confirmed, thus making it highly relevant for various high-speed electronic devices[47]. In total, 16 forms of borophene have been confirmed so far. Among them, the β-rhombohedral, α-rhombohedral, α-tetragonal, β- tetragonal forms and recently founded γ-rhombohedral[48] form exist as pristine allotropes of boron[48]. Three other structures of boronnamely β12, X3 and striped borophene (see Figure 1.3) have been observed by scanning tunneling microscopy[49]. The buckled triangular

structures of boron nanosheets are found to be more prominent in the literature and, consequently, are utilized to build boron nanotubes[50,51].

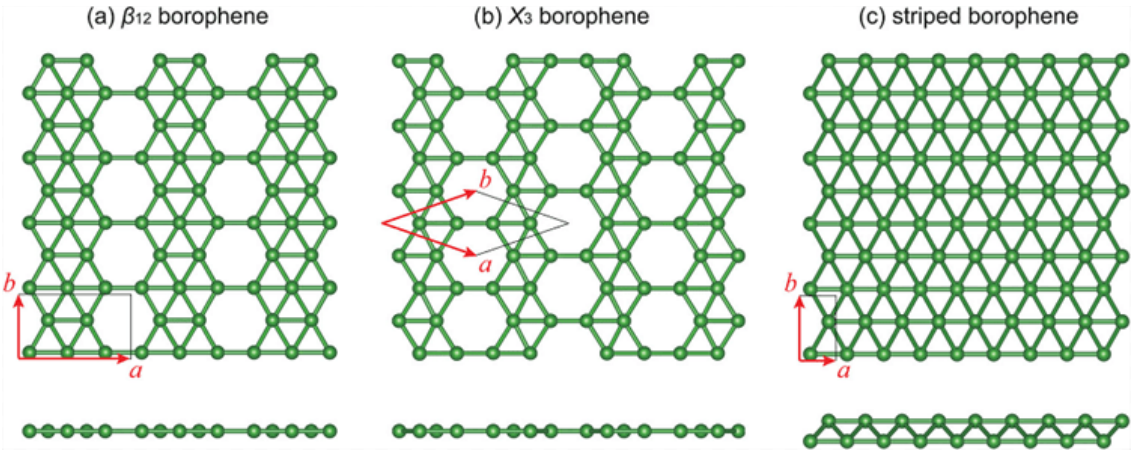

Figure 1.3 Top and side view of experimentally found (a) β12, (b) X3, and (c) striped borophene[52].

Functionalization- The discovery of graphene has fueled attempts at the isolation of other 2D materials. Computational chemistry, and, especially, density functional theory computations serve as a powerful tool to determine the properties and structures of 2D materials. In the present study, silicene, germanene as well as borophene are considered because of their competitive properties with respect to graphene. The potential applications due to the interaction between graphene and different chemical functional groups have resulted in new dimensions in the field of 2D materials[53]. The physiosorption of various molecules on graphene has been reported to enhance as well as further improve the electronic properties of graphene[54]. Thus, the functionalization of 2D materials by adsorbing different elements and exploring the resulting modifications in the properties have gained a lot of attention in the 2D community. The field of environmental monitoring has seen a lot of advances using 2D materials as gas sensors. Due to their high surface to volume ratio, low noise and sensitivity of electronic properties to the variations in the surroundings have made 2D materials highly useful for gas sensing, metal sensing, and bio-molecular sensing applications[55,56]. Various studies in the literature have been reported for testing the sensing power of different 2D

materials. One of the most common approaches in this regard is by adsorption/doping of a foreign moiety onto the 2D sheet[55,57]. The comparison of the interaction of small organic molecules adsorbed on silicene and on graphene has shown the strong adsorption in the former case[58]. Two types of charge-transfer mechanisms have been observed in the case of adsorption of small molecules such as NH_3 and NO_2 on graphene. One is due to orbital hybridization which is very common, and the other depends on the positions of the HOMO and LUMO of the molecule with respect to the Dirac point of graphene. The latter occurs in paramagnetic materials[59]. Further, in 2014, various small organic molecules such as acetone, acetonitrile, methane, benzene, etc. were studied on a silicene surface along with the inclusion of the effect of doping of Li atoms in pristine silicene and acetone-adsorbed silicene by means of DFT calculations[58]. The high reactivity of silicene to nitrogen-based gas molecules can be understood with the frontier orbitals of molecules and the corresponding electronic states of the p_z electrons in silicene[60]. In the literature, various modulations in the structure of 2D materials such as by doping or by including vacancy defects have been investigated to detect the effect on the interactions between host molecules and 2D materials. Dissociation of small molecules such as H_2, O_2, and CO at the defect sites of silicene and graphene has been investigated[61]. The molecules which have been otherwise inert to pristine silicene and graphene can be bonded to the 2D surface by involving defect sites[61]. The adsorption characteristics of alkali, alkaline-earth, and transition metal atoms have been analyzed by Sahin et al., and their studies indicated that the reactive crystal structure of silicene provides a rich playground for functionalization at the nanoscale[62]. Similar studies have been conducted for germanene and borophene showing stronger binding interactions in germanene as compare to silicene as well as borophene[63–67].

The field is progressing and one of the paths still unexplored includes the adsorption of heavier elements including lanthanides and actinides onto relatively new 2D materials other than graphene. The deposition and safe storage of the "waste" generated by the nuclear fuel cycle and nuclear weapons production is one of the most pressing, and potentially costly, environmental problems for the 21st century[68]. Actinides being the most important part of the nuclear fuel cycle and due to their long half-lives account for most of the radiotoxicity of nuclear waste after the first 500 years of disposal. After several hundred years, radiotoxicity is dominated by ^{239}Pu (half-life = 24,100 years) and ^{237}Np (half-life = 2,000,000 years)[68,69]. The treatment of groundwater containing radionuclides has become a major task associated with the mining, milling, and processing of materials for the nuclear power industry[70]. The mobility of these radioactive materials in groundwater is dependent on the water-mineral interfaces[71]. The adsorption of these radionuclides with different adsorbents having large adsorption tendencies has been widely investigated[72]. Among various adsorbents, graphene oxides (GOs) have been investigated as a highly efficient system for contaminants[73–75]. With the advancement of other types of 2D materials beyond graphene, we can extend this study to other new members of the 2D family. This study will not only quantify novel properties of 2D materials and electronic structures, but it will also be relevant for the detection and absorption of harmful radioactive waste. It is rightly said that "Only the very tip of the iceberg has been uncovered so far"[4], and our work is a small contribution to the overall effort.

1.2 Objective and Approach

The overall goal of the thesis is **to use quantum chemistry methods such as DFT and band structure approaches to study and understand the interaction of heavy elements (actinides)**

with 2D materials. This work specifically addresses the structural parameters, adsorption strengths and electronic properties of the systems under study.

Complexes of actinides such as uranium (U), neptunium (Np) and plutonium (Pu) have been considered. The choice of ligands for the complexes was done by keeping the focus on environmentally relevant ligands such as CO_3^{2-}, NO_3^-, OH^- and the oxo ligand. Since we are dealing with the periodic model in the present work, the coordination number was set in a way so as to have neutral complexes of actinides. The interaction of graphene with U complexes and other heavy elements has been taken as a reference point[76,77]. Two methodological approaches have been considered:

1.2.1 Metal-Centered Approach: This approach includes a central metal atom which along with other ligands in its first coordination sphere will be chemically decorated by the 2D material. The primary question concerns the strengths of adsorption for different complexes with a view of mitigating environmental damage of metal-contaminated sites. Hence, strong interactions are desirable. The secondary question involves the influence of complexes on the structural parameters of 2D material (that is, the influence of oxidation state of the metal, the influence of ligands around the metal atom) and amount of charge transfer between the complex and 2D sheet.

1.2.2 Materials-Centered Approach: In this approach, the metal is considered as chemically decorating the 2D material. The main question is concerned with the effect of adsorption on the electronic structure (band gap) of the material.

This work is strongly driven by environmental problems as well as the potential for discovering and developing materials with novel properties.

1.3 Organization of this Thesis

The aim of this study is to provide detailed comparative studies on the interactions occurring between heavier actinide atoms and different 2D materials such as silicene, germanene and borophene. The results are not only expected to be highly advantageous in the understanding of sensing capacities of these three 2D layers for radioactive materials but also, to understand periodic trends for actinide complexes along with testing the ability of different ligands to adsorb on 2D materials.

A brief introduction to the background and advancement in the field of 2D materials along with the importance of actinides for this study have been mentioned in Chapter 1.

The details of various quantum chemical methods and different softwares used in the study are contained in Chapter 2. Discussion on relativistic effects as well as Mayer bond order analysis is also provided.

The work in Chapter 3 describes a thorough study done for the adsorption of $MO_2(OH)_2$, $MO_2(NO_3)_2$, $MO_2(CO_3)$ where M= U, Np, Pu on 2D silicene and germanene. Two types of models have been considered for each type of 2D surface depending on the sheet size. Cluster and periodic approaches have been employed; thus, results from ADF and PWSCF softwares (see Chapter 2) have been investigated. Different 2D layers in the study have been compared with each other for sensing similar types of actinide complexes and trends have been observed.

Chapter 4 summarizes a study of the binding interactions of the same molecules on two types of borophene structures (striped borophene and β_{12}-borophene, see Figure 1.3). In this chapter, only the periodic model has been employed to provide a comparative study between the planar and buckled 2D sheets.

Finally, in chapter 5, a conclusion of the thesis is provided along with an outlook for future studies.

Bibliography

1. Al-Hartomy, O. A. *et al.* Properties of Natural Rubber-Based Composites Containing Fullerene. *Int. J. Polym. Sci.* **2012**, 1–8 (2012).
2. Iijima, S. Helical microtubules of graphitic carbon. *Nature* **354**, 56–58 (1991).
3. Geim, A. K. & Novoselov, K. S. The rise of graphene. *Nat. Mater.* **6**, 183–91 (2007).
4. Sur, U. K. Graphene: A Rising Star on the Horizon of Materials Science. *Int. J. Electrochem.* **2012**, 1–12 (2012).
5. Novoselov, K. S. *et al. Two Dimensional Atomic Crystals*.
6. Partoens, B. & Peeters, F. M. From graphene to graphite: Electronic structure around the K point. *Phys. Rev. B* **74**, 075404 (2006).
7. Novoselov, K. S. *et al.* Two-dimensional gas of massless Dirac fermions in graphene. *Nature* **438**, 197–200 (2005).
8. Balendhran, S., Walia, S., Nili, H., Sriram, S. & Bhaskaran, M. Elemental Analogues of Graphene: Silicene, Germanene, Stanene, and Phosphorene. *Small* **11**, 640–652 (2015).
9. Castro Neto, A. H., Guinea, F., Peres, N. M. R., Novoselov, K. S. & Geim, A. K. The electronic properties of graphene. *Rev. Mod. Phys.* **81**, 109–162 (2009).
10. Balandin, A. A. Thermal properties of graphene and nanostructured carbon materials. *Nat. Mater.* **10**, 569–581 (2011).
11. Suk, J. W., Piner, R. D., An, J. & Ruoff, R. S. Mechanical Properties of Monolayer Graphene Oxide. *ACS Nano* **4**, 6557–6564 (2010).
12. Falkovsky, L. A. Optical properties of graphene. *J. Phys. Conf. Ser.* **129**, 012004 (2008).
13. Huang, Y., Liang, J. & Chen, Y. An Overview of the Applications of Graphene-Based Materials in Supercapacitors. *Small* **8**, 1805–1834 (2012).
14. Chung, C. *et al.* Biomedical Applications of Graphene and Graphene Oxide. *Acc. Chem. Res.* **46**, 2211–2224 (2013).
15. Perreault, F., Fonseca de Faria, A. & Elimelech, M. Environmental applications of graphene-based nanomaterials. *Chem. Soc. Rev.* **44**, 5861–5896 (2015).
16. Dreyer, D. R., Park, S., Bielawski, C. W. & Ruoff, R. S. The chemistry of graphene oxide. *Chem. Soc. Rev.* **39**, 228–240 (2010).
17. Hontoria-Lucas, C., López-Peinado, A. J., López-González, J. . d. D., Rojas-Cervantes, M. L. & Martín-Aranda, R. M. Study of oxygen-containing groups in a series of graphite oxides: Physical and chemical characterization. *Carbon N. Y.* **33**, 1585–1592 (1995).
18. Aïssa, B., Memon, N. K., Ali, A. & Khraisheh, M. K. Recent Progress in the Growth and Applications of Graphene as a Smart Material: A Review. *Front. Mater.* **2**, 58 (2015).
19. Yan Voon, L. C. L. & Guzmán-Verri, G. G. Is silicene the next graphene? *MRS Bull.* **39**, 366–373 (2014).
20. Tang, Q. & Zhou, Z. Graphene-analogous low-dimensional materials. *Prog. Mater. Sci.* **58**, 1244–

1315 (2013).

21. Piazza, Z. A. *et al.* Planar hexagonal B36 as a potential basis for extended single-atom layer boron sheets. *Nat. Commun.* **5**, 3113 (2014).

22. Mannix, A. J. *et al.* Synthesis of borophenes: Anisotropic, two-dimensional boron polymorphs. *Science* **350**, 1513–6 (2015).

23. Jose, D. & Datta, A. Structures and Chemical Properties of Silicene: Unlike Graphene. *Acc. Chem. Res.* **47**, 593–602 (2014).

24. Takeda, K. & Shiraishi, K. Theoretical possibility of stage corrugation in Si and Ge analogs of graphite. *Phys. Rev. B* **50**, 14916–14922 (1994).

25. Guzmán-Verri, G. G. & Lew Yan Voon, L. C. Electronic structure of silicon-based nanostructures. *Phys. Rev. B* **76**, 075131 (2007).

26. Cahangirov, S., Topsakal, M., Aktürk, E., Şahin, H. & Ciraci, S. Two- and One-Dimensional Honeycomb Structures of Silicon and Germanium. *Phys. Rev. Lett.* **102**, 236804 (2009).

27. De Padova, P. *et al.* Evidence of graphene-like electronic signature in silicene nanoribbons. *Appl. Phys. Lett.* **96**, 261905 (2010).

28. Vogt, P. *et al.* Silicene: Compelling Experimental Evidence for Graphenelike Two-Dimensional Silicon. *Phys. Rev. Lett.* **108**, 155501 (2012).

29. Meng, L. *et al.* Buckled Silicene Formation on Ir(111). *Nano Lett.* **13**, 685–690 (2013).

30. Zhaoa, J. *et al.* Rise of silicene: A competitive 2D material. *Prog. Mater. Sci.* **83**, 24–151 (2016).

31. Lebègue, S. & Eriksson, O. Electronic structure of two-dimensional crystals from *ab initio* theory. *Phys. Rev. B* **79**, 115409 (2009).

32. Ni, Z. *et al.* Tunable Bandgap in Silicene and Germanene. *Nano Lett.* **12**, 113–118 (2012).

33. Liu, C.-C., Feng, W. & Yao, Y. Quantum Spin Hall Effect in Silicene and Two-Dimensional Germanium. *Phys. Rev. Lett.* **107**, 076802 (2011).

34. Kaloni, T. P., Cheng, Y. C. & Schwingenschlögl, U. Hole doped Dirac states in silicene by biaxial tensile strain. *J. Appl. Phys.* **113**, 104305 (2013).

35. Fatholahnejad, H. *et al.* Tuning the analog and digital performance of Germanene nanoribbon field effect transistors with engineering the width and geometry of source, channel and drain region in the ballistic regime. *Mater. Sci. Semicond. Process.* **80**, 18–23 (2018).

36. Zhu, J. & Schwingenschlögl, U. Stability and electronic properties of silicene on WSe_2. *J. Mater. Chem. C* **3**, 3946–3953 (2015).

37. Ye, M. *et al.* Tunable band gap in germanene by surface adsorption. *Phys. E Low-dimensional Syst. Nanostructures* **59**, 60–65 (2014).

38. Bianco, E. *et al.* Stability and Exfoliation of Germanane: A Germanium Graphane Analogue. *ACS Nano* **7**, 4414–4421 (2013).

39. Li, L. *et al.* Buckled Germanene Formation on Pt(111). *Adv. Mater.* **26**, 4820–4824 (2014).

40. Dávila, M. E., Xian, L., Cahangirov, S., Rubio, A. & Le Lay, G. Germanene: a novel two-dimensional germanium allotrope akin to graphene and silicene. *New J. Phys.* **16**, 095002 (2014).

41. Acun, A. *et al.* Germanene: the germanium analogue of graphene. *J. Phys. Condens. Matter* **27**, 443002 (2015).

42. Yang, L.-M. *et al.* Revealing unusual chemical bonding in planar hyper-coordinate Ni_2Ge and quasi-planar Ni_2Si two-dimensional crystals. *Phys. Chem. Chem. Phys.* **17**, 26043–26048 (2015).

43. Liu, Y., Penev, E. S. & Yakobson, B. I. Probing the Synthesis of Two-Dimensional Boron by First-Principles Computations. *Angew. Chemie Int. Ed.* **52**, 3156–3159 (2013).

44. Mannix, A. J. *et al.* Synthesis of borophenes: Anisotropic, two-dimensional boron polymorphs. *Science* **350**, 1513–6 (2015).

45. Kong, L., Wu, K. & Chen, L. Recent progress on borophene: Growth and structures. *Front. Phys.* **13**, 138105 (2018).

46. Sergeeva, A. P. *et al.* Understanding Boron through Size-Selected Clusters: Structure, Chemical Bonding, and Fluxionality. *Acc. Chem. Res.* **47**, 1349–1358 (2014).

47. Feng, B. *et al.* Dirac Fermions in Borophene. *Phys. Rev. Lett.* **118**, 096401 (2017).

48. Oganov, A. R. *et al.* Ionic high-pressure form of elemental boron. *Nature* **457**, 863–867 (2009).

49. Peng, B. *et al.* Stability and strength of atomically thin borophene from first principles calculations. *Mater. Res. Lett.* **5**, 399–407 (2017).

50. Boustani, I. Systematic ab initio investigation of bare boron clusters:mDetermination of the geometryand electronic structures of B n (n=2–14). *Phys. Rev. B* **55**, 16426–16438 (1997).

51. Nagarajan, V. & Chandiramouli, R. Borophene nanosheet molecular device for detection of ethanol – A first-principles study. *Comput. Theor. Chem.* **1105**, 52–60 (2017).

52. Peng, B. *et al.* Stability and strength of atomically thin borophene from first principles calculations. *Mater. Res. Lett.* **5**, 399–407 (2017).

53. Krepel, D. & Hod, O. Lithium-Mediated Benzene Adsorption on Graphene and Graphene Nanoribbons. *J. Phys. Chem. C* 130916143804002 (2013).

54. Zhang, Y.-H. *et al.* Improving gas sensing properties of graphene by introducing dopants and defects: a first-principles study. *Nanotechnology* **20**, 185504 (2009).

55. Anichini, C. *et al.* Chemical sensing with 2D materials. *Chem. Soc. Rev.* **47**, 4860–4908 (2018).

56. Varghese, S. *et al.* Two-Dimensional Materials for Sensing: Graphene and Beyond. *Electronics* **4**, 651–687 (2015).

57. Zeng, Y. *et al.* Two-Dimensional Nanomaterials for Gas Sensing Applications: The Role of Theoretical Calculations. *Nanomaterials* **8**, 851 (2018).

58. Kaloni, T. P., Schreckenbach, G. & Freund, M. S. Large Enhancement and Tunable Band Gap in Silicene by Small Organic Molecule Adsorption. *J. Phys. Chem. C* **118**, 23361–23367 (2014).

59. Lazar, P. *et al.* Adsorption of Small Organic Molecules on Graphene. *J. Am. Chem. Soc.* **135**, 6372–6377 (2013).

60. Hu, W., Xia, N., Wu, X., Li, Z. & Yang, J. Silicene as a highly sensitive molecule sensor for NH3, NO and NO2. *Phys. Chem. Chem. Phys.* **16**, 6957 (2014).

61. Gürel, H. H., Özçelik, V. O. & Ciraci, S. Dissociative Adsorption of Molecules on Graphene and

Silicene. *J. Phys. Chem. C* **118**, 27574–27582 (2014).

62. Sahin, H. & Peeters, F. M. Adsorption of alkali, alkaline-earth, and 3 d transition metal atoms on silicene. *Phys. Rev. B* **87**, 085423 (2013).

63. Cui, H., Zhang, X. & Chen, D. Borophene: a promising adsorbent material with strong ability and capacity for SO2 adsorption. *Appl. Phys. A* **124**, 636 (2018).

64. Chandiramouli, R. & Nagarajan, V. Adsorption studies of NH3 molecules on functionalized germanene nanosheet – A DFT study. *Chem. Phys. Lett.* **665**, 22–30 (2016).

65. Huang, C.-S., Murat, A., Babar, V., Montes, E. & Schwingenschlögl, U. Adsorption of the Gas Molecules NH_3, NO, NO_2, and CO on Borophene. *J. Phys. Chem. C* **122**, 14665–14670 (2018).

66. Li, S. *et al*. Tunable electronic and magnetic properties in germanene by alkali, alkaline-earth, group III and 3d transition metal atom adsorption. *Phys. Chem. Chem. Phys.* **16**, 15968 (2014).

67. Xia, W., Hu, W., Li, Z. & Yang, J. A first-principles study of gas adsorption on germanene. *Phys. Chem. Chem. Phys.* **16**, 22495–22498 (2014).

68. Ewing, R. C. Nuclear waste forms for actinides. *Proc. Natl. Acad. Sci. U. S. A.* **96**, 3432–9 (1999).

69. Ewing, R. C., Weber, W. J. & Lian, J. Nuclear waste disposal—pyrochlore (A2B2O7): Nuclear waste form for the immobilization of plutonium and "minor" actinides. *J. Appl. Phys.* **95**, 5949–5971 (2004).

70. Morrison, S. J. & Spangler, R. R. *Extraction of Uranium and Molybdenum from Aqueous Solutions: A Survey of Industrial Materials for Use in Chemical Barriers for Uranium Mill Tailings Remediation*. *Environ. Sci. Technol* **26**, (1992).

71. Langmuir, D. Uranium solution-mineral equilibria at low temperatures with applications to sedimentary ore deposits. *Geochim. Cosmochim. Acta* **42**, 547–569 (1978).

72. John R. Bargar, *, †, Rebecca Reitmeyer, ‡ and & Davis‡, J. A. Spectroscopic Confirmation of Uranium(VI)−Carbonato Adsorption Complexes on Hematite. (1999).

73. Sun, Y., Wang, Q., Chen, C., Tan, X. & Wang, X. Interaction between Eu(III) and Graphene Oxide Nanosheets Investigated by Batch and Extended X-ray Absorption Fine Structure Spectroscopy and by Modeling Techniques. *Environ. Sci. Technol.* **46**, 6020–6027 (2012).

74. Romanchuk, A. Y., Slesarev, A. S., Kalmykov, S. N., Kosynkin, D. V. & Tour, J. M. Graphene oxide for effective radionuclide removal. *Phys. Chem. Chem. Phys.* **15**, 2321 (2013).

75. Zhao, G., Li, J., Ren, X., Chen, C. & Wang, X. Few-Layered Graphene Oxide Nanosheets As Superior Sorbents for Heavy Metal Ion Pollution Management. *Environ. Sci. Technol.* **45**, 10454–10462 (2011).

76. Sun, Y. *et al.* Adsorption and Desorption of U(VI) on Functionalized Graphene Oxides: A Combined Experimental and Theoretical Study. *Environ. Sci. Technol.* **49**, 4255–4262 (2015).

77. Du, J. & Jiang, G. Adsorption of 5f-electron atoms (ThCm) on graphene surface: An all-electron ZORA-DFT study. *J. Colloid Interface Sci.* **508**, 159–166 (2017).

Chapter 2: Computational Methods

With the development of advanced computer components, the scientific community has witnessed an emergence of interest in computational chemistry. Computational chemistry is a field with a focus on resolving chemical problems. It is not directly related to the development of new theoretical approaches (theoretical chemistry) but there is a strong interplay between computational and theoretical chemistry as computational chemistry applies theoretical methods into highly efficient computer programs in which a mathematical method is sufficiently well developed to compute numerical data of different molecules and solids[1,2]. The main applications of the field include the initial step as modeling of a molecular system which is tough to analyze in the real world. This contributes to solving problems such as the difficulty in handling the radioactive material as well as nuclear waste disposal problems[3,4]. Moreover, it helps in attaining knowledge of parameters and properties which are otherwise difficult to observe experimentally. However, the accuracy of methods depends on the size of complexes, i.e. small molecular calculations can be made highly accurate and less expensive[5].

Computational chemistry spans many research areas such as drug design, protein simulation including docking, etc., transition state calculations, spectroscopy, gas-phase vs. solvent phase calculations, X-ray crystallography, proton transfer, adsorption, etc. There are numerous quantum-chemical methods for the computations but density functional theory (DFT) is one of the most widely used cost-effective methods for quantum-mechanical (QM) calculations of the structure of atoms, molecules, crystals, surfaces, and their interactions[1,5–7]. This method is highly useful for molecules with a large number of atoms and can be combined with periodic boundary conditions. For modeling actinide systems accurately, several methods are used to get an approximate wave

function and density of the system. As we are dealing with heavier elements in this study, relativistic effects are of utmost importance because of the high curvatures of inner shell orbitals of actinides which is, hence, giving rise to high kinetic energy[8]. A brief description of computational methods that were used to model the systems under study is provided in this chapter.

2.1 Schrödinger equation[1,9]

The quantum mechanical systems such as atoms and molecules are described by mathematical functions that are solutions of a linear partial differential equation called the Schrödinger equation[9] which was developed by Erwin Schrödinger in 1926. In the microscopic world the state of motion with respect to time is governed by the time-dependent Schrödinger equation which is as follows:

$$\widehat{H}\psi = i\hbar\frac{\partial\psi}{\partial t} \tag{2.1}$$

where $\widehat{H}$ is the Hamiltonian operator which accounts for the kinetic and potential energies of the particle(s) in the system, ψ is the state vector of the quantum system called the wave function, i is the imaginary unit, $\hbar = \frac{h}{2\Pi}$ is the reduced Planck's constant, and $\frac{\partial}{\partial t}$ is the partial derivative with respect to time.

The above equation 2.1 also describes the wave functions for stationary states which can be further simplified by another form of the Schrödinger equation, the time-independent Schrödinger equation:

$$\widehat{H}\psi = E\Psi \tag{2.2}$$

where Ψ is the eigenfunction of the Hamiltonian, and E is a constant equal to the energy level of the system (energy eigenvalue).

The molecular Hamiltonian operator contains five contributions (see equation 2.3) such as from the kinetic energies (first two parts of equation 2.3) and the potential energy of Coulomb attraction (third term of equation 2.3) of the electrons to the nuclei. The last two terms of equation 2.3 are also potential energy terms of all the particles in the system (electrons and nuclei), specifically the Coloumbic electron-electron and nuclei-nuclei repulsions respectively.

$$\hat{H} = -\sum_{i}\frac{\hbar^2}{2m_e}\nabla_i^2 - \sum_{k}\frac{\hbar^2}{2m_k}\nabla_k^2 - \sum_{i}\sum_{k}\frac{e^2 Z_k}{r_{ik}} + \sum_{i<j}\frac{e^2}{r_{ij}} + \sum_{k<l}\frac{e^2 Z_k Z_l}{r_{kl}} \qquad (2.3)$$

In Eq. (2.3) constants can be made equal to 1 in the unit system known as Hartree atomic units where 1 Hartree = 27.211eV or 2 Rydberg constant, *i* and *j* represent electrons, *k* and *l* denote nuclei, m_e is mass of the electron, m_k is the mass of nucleus k, ∇^2 is the Laplacian operator, *e* is the charge on the electron, *Z* is an atomic number, and r_{ab} is the distance between particle a and b.

2.2 The Born-Oppenheimer approximation[1,10]

Due to the correlated motion of particles in many-particle systems, it is quite tough to get accurate wave functions. This is because the $\hat{H}$ operator (see equation 2.3) containing both attraction and repulsion terms is no longer separable as different potential terms couple the motion of the various particles. To partly resolve this the Born-Oppenheimer approximation[10] came into the picture. It states that the nuclei are much more massive than the electrons, which permits us to say that the nuclei are nearly fixed with respect to electron motion. As a result, we can decouple the nuclear and electronic motions and compute electronic energies for fixed nuclear positions. Hence, the nuclear kinetic energy term from equation 2.3 can be eliminated, and we have a constant value for

the nucleus-nucleus potential energy term for the given geometry. Thus, the electronic Schrödinger equation is given as:

$$(H_{el} + V_N)\psi_{el}(q_i; q_k) = E_{el}\psi_{el}(q_i; q_k) \quad (2.4)$$

where H_{el} comprises the first, third and fourth terms of equation 2.3 and *el* is the invocation of the Born-Oppenheimer approximation. V_N is the nuclear-nuclear repulsion, independent variables are represented by q_i (electronic coordinates), and nuclear coordinates q_k are parameters. The term V_N in equation 2.4 can be ignored as it is a constant for a given set of fixed nuclear coordinates. In this case, the eigenvalue of equation 2.4 is called the "pure electronic energy" and E_{el} can be obtained by adding V_N to this eigenvalue.

Equation 2.4 is also called the "clamped-nuclei" Schrödinger equation and it is highly beneficial for the concept of the potential energy surface (PES) which is a mathematical function that provides the energy of a molecule as a function of its geometry. However, this approximation fails in the case of high speeds of nuclei as for highly excited vibrational states, for energies close to crossing energies in the PES[11], or when the energy gap between the ground and excited electronic states is smaller than the energy scale of the nuclear motion like in metals[12].

2.3 The Variational method[1]

The variational method is a way of finding approximations to the lowest energy eigenstate or the ground state thus, to evaluate approximate wavefunctions such as molecular orbitals[13]. The basic idea is to choose a "trial" wavefunction that obeys the boundary conditions of the system and that depends on some adjustable parameters called "variational parameters". By adjusting these parameters, one's aim is to find the lowest energy trial wavefunction. The resulting trial wavefunction and its corresponding energy are variational method approximations to the exact

wavefunction and energy[14]. According to the Variational Theorem, the energy of any trial wavefunction 'E' is always an upper bound to the exact ground state energy 'E_0'. For the Schrödinger equation, the approximation can be given as:

$$E = \frac{\int \phi H \phi \, dr}{\int \Phi^2 \, dr} \geq E_0 \tag{2.5}$$

2.4 The Hartree-Fock (HF) approximation[1,15,16]

In a stationary state, the determination of the wave function and energy of a many-electron system can be achieved by the HF approximation. In the older literature, the Hartree-Fock method was called 'Self-consistent field method'. In this approximation, the molecular orbitals (MOs) can be separately evaluated from a one-electron operator. In other words, the motion of one electron is independent of the others and hence, the average Coloumb repulsion which is resulting due to the electron-electron repulsion is observed by each electron.

The Hartree-Fock wave function can be given by a Slater determinant (see equation 2.6) which obeys the Pauli Exclusion Principle and gives an antisymmetric wavefunction with respect to the electron exchange.

$$\psi(1,2,\ldots\ldots\ldots N) = \frac{1}{\sqrt{(2N)!}} \begin{vmatrix} \Psi_1\alpha(1) & \Psi_1\beta(1) & \ldots\ldots\ldots\ldots & \Psi_N\alpha(1) & \Psi_N\beta(1) \\ \Psi_1\alpha(2) & \Psi_1\beta(2) & \ldots\ldots\ldots\ldots & \Psi_N\alpha(2) & \Psi_N\beta(2) \\ . & . & . & . & . \\ . & . & . & . & . \\ . & . & . & . & . \\ \Psi_1\alpha(2N) & \Psi_1\beta(2N) & \ldots\ldots\ldots & \Psi_N\alpha(2N) & \Psi_N\beta(2N) \end{vmatrix} \tag{2.6}$$

where, α and β are spin functions and N is number of electrons.

The energy can be given as:

$$E_{el} = \langle \Psi^*(1,2,\dots\dots\dots 2N) | \hat{H} | \Psi(1,2,\dots\dots\dots 2N) \rangle \quad (2.7)$$

It can be rewritten as:

$$E_{el} = 2\sum_{j=1}^{N} I_j + \Sigma_{i=1}^{N} \sum_{j=1}^{N} (2J_{ij} - K_{ij}) \quad (2.8)$$

where,

$$I_j = \int dr_j \psi_j^*(r_j) \left(-\frac{1}{2}\nabla_j^2 - \sum_{N}^{M} \frac{z_A}{r_{jA}} \right) \psi_j(r_j) \quad (2.9)$$

$$J_{ij} = \int\int dr_1\, dr_2 \psi_i^*(r_1) \Psi_j^*(r_2) \frac{1}{r_{12}} \psi_i(r_1) \Psi_j(r_2) \quad (2.10)$$

$$K_{ij} = \int\int dr_1\, dr_2 \psi_i^*(r_1) \psi_j^*(r_2) \frac{1}{r_{12}} \psi_i(r_2) \psi_j(r_1) \quad (2.11)$$

The spatial orbitals that minimize the energy E after applying the Variational principle to equation 2.7 satisfy the following equations:

$$\hat{F}(r_1)\psi_i(r_1) = \varepsilon_i \psi_i(r_1) \qquad i = 1,2,\dots,N \quad (2.12)$$

where $\hat{F}$ is the Fock operator.

$$\hat{F}(r_1) = \hat{f}(r_1) + \sum_{j=1}^{N} \left[2\hat{J}_j(r_1) - \hat{K}_j(r_1) \right] \quad (2.13)$$

In equation 2.13,

$$\hat{f}(r_1) = -\frac{1}{2}\nabla_1^2 - \Sigma_A \frac{z_A}{r_{1A}} \quad (2.14)$$

The Coulomb operator is $\hat{J}_j(r_1)$

$$\hat{J}_j(r_1)\psi_i(r_1) = \psi_i(r_1) \int dr_2 \psi_j^*(r_2) \frac{1}{r_{12}} \psi_j(r_2) \quad (2.15)$$

The exchange operator is $\widehat{K}_j(r_1)$

$$\widehat{K}_j(r_1)\psi_i(r_1) = \psi_j(r_1)\int dr_2\psi_j^*(r_2)\frac{1}{r_{12}}\psi_i(r_2) \tag{2.16}$$

For the energy of the ith molecular orbital, one can multiply the equation 2.12 by $\psi_i^*(r_1)$ and integerating over r_1

$$\varepsilon_i = \int dr_1\psi_i^*(r_1)\hat{F}(r_1)\psi_i(r_1) \tag{2.17}$$

On putting the value of Fock operator in equation 2.17 we get:

$$\varepsilon_i = I_j + \sum_{j=1}^{N}\left(2J_{ij} - K_{ij}\right) \tag{2.18}$$

If we compare this equation with the energy equation 2.8, we get:

$$E = \sum_{i=1}^{N}(I_i + \varepsilon_i) \tag{2.19}$$

The molecular orbitals were expressed as linear combinations of basis functions by Clemens Roothan[17].

$$\psi = \Sigma_{\nu=1}^{K} c_\nu \phi_\nu \tag{2.20}$$

Hence, the Hartree-Fock-Roothan equations are as follows:

$$\sum_\nu F_{\mu\nu}c_\nu = \varepsilon\Sigma_\nu S_{\mu\nu}c_\nu \qquad \mu = 1,2, \ldots\ldots, \text{K} \tag{2.21}$$

where $F_{\mu\nu}$ and $S_{\mu\nu}$ are the Fock matrix elements and overlap matrix elements respectively, see below:

$$F_{\mu\nu} = \int dr_1\phi_\mu^*(r_1)\hat{F}(r_1)\phi_\nu(r_1) \tag{2.22}$$

$$S_{\mu\nu} = \int dr_1 \phi_\mu^*(r_1)\phi_\nu(r_1) \tag{2.23}$$

The set of algebraic equations for c_ν is represented by equation 2.21, which is called Hartree-Fock-Roothan equations[17].

Since the operator depends on the solutions, the equations in either HF-form or the Roothan form need to be solved self consistently. At each step, the energy calculations use already generated orbitals from the last step as input to construct the Fock operator and this is commonly known as the self-consistent field (SCF) approach which eventually gives us the SCF energy.

In spite of the accurate geometries obtained from the HF method, this methodology includes some discrepancies. Hartree-Fock considers the electron-electron repulsion with the repulsion of each electron with an average electron field and, hence, results in an error in the wavefunction and the energy. This energy error is called the total correlation energy which is about 1 eV per electron pair in a bond or lone pair which is small as compared to the total energy but causes serious impact on various properties of the system and reaction energies[18]. Many different approaches such as many-body perturbation theory, coupled-cluster theory, and configuration interaction (CI) can be incorporated with the HF method as a starting point to get more accurate results and they are generally referred as post-Hartree-Fock methods. For large systems like actinide complexes, post-Hartree-Fock methods are highly expensive and difficult to employ[1,19].

2.5 Density Functional Theory (DFT)[1,6]

Density functional theory is one of the most widely used variational methods in computational chemistry to compute the electronic structure of many-body systems such as atoms, molecules, and condensed phases. Derived from the N-particle Schrödinger equation, this method is purely

described in terms of the ground-state density distribution and wave functions for a single particle. DFT reduces the computations of the ground state properties of the interacting particles exactly to the solution of single-particle Hartree-type equations and hence, it is a widely used method because of its computational accuracy and efficiency as compared to HF as well as post-HF methods. Although DFT has its initial base in the Thomson-Fermi model for materials, it was first put in shape by Walter Kohn and Pierre Hohenberg in the framework of two theorems[20]. The Hohenberg-Kohn theorems are the heart of DFT and they create a connection between the ground-state electron density and the many-electron Schrödinger equation. The first theorem states that the external potential $V(r)$ is a unique functional of the electron density $\rho(r)$ (see equation 2.24). In other words, the ground state density uniquely determines the potential and hence, other properties of the system. The second theorem says that if the input density is the true ground state density then the functional that delivers the ground state energy of the system gives the lowest energy (see equation 2.25), that is, the ground state energy can be obtained variationally.

$$E[\rho(r)] = \int \rho(r)V(r)\,dr + F[\rho(r)] \tag{2.24}$$

where $F[\rho(r)]$ is the universal functional of the electron density $\rho(r)$

$$E[\rho(r)] = \int \rho(r)V(r)\,dr + F[\rho(r)] \geq E_0 \tag{2.25}$$

2.5.1 Kohn-Sham Self-Consistent Field methodology[1]

Kohn-Sham SCF methodology is based on solving the problem related to the electron-electron interaction term in the current Hamiltonian. This methodology assumes a fictitious system containing non-interacting electrons that, however, has the same overall ground state energy density as the real system which contains interactions of electrons. Hence, the energy term in

equation 2.26 depends on the kinetic energy of the non-interacting electrons (T_{ni}), the nucleus-electron interaction (V_{ne}), the classical electron-electron repulsion (V_{ee}), and the corrections to the kinetic energy (ΔT) and classical electron-electron repulsion energy (ΔV_{ee}) due to the interacting nature of electrons.

$$E[\rho(r)] = T_{ni}[\rho(r)] + V_{ne}[\rho(r)] + V_{ee}[\rho(r)] + \Delta T[\rho(r)] + \Delta V_{ee}[\rho(r)] \tag{2.26}$$

Within an orbital expression of the density, equation 2.26 may be rewritten as:

$$E[\rho(r)] = \sum_{i}^{N} \left(\left\langle \chi_i \left| -\frac{1}{2}\nabla_i^2 \right| \chi_i \right\rangle - \left\langle \chi_i \left| \sum_{k}^{nuclei} \frac{Z_k}{|r_i - r_k|} \right| \chi_i \right\rangle \right) + \sum_{i}^{N} \left\langle \chi_i \left| \frac{1}{2} \int \frac{\rho(r')}{|r_i - r'|} dr' \right| \chi_i \right\rangle + E_{xc}[\rho(r)] \tag{2.27}$$

where, N represents the number of electrons and E_{xc} is the exchange-correlation energy, which is the sum of the last two terms of equation (2.26).

The density for the exact eigenfunction of the non-interacting system (that is, its Slater determinant wave function) is given as:

$$\rho = \sum_{i=1}^{N} \langle \chi_i | \chi_i \rangle \tag{2.28}$$

The orbitals χ_i that minimizes the E in equation 2.28 satisfy the following equations (Kohn-Sham equations):

$$h_i^{KS} \chi_i = \varepsilon_i \chi_i \tag{2.29}$$

Here, the Kohn-Sham operator h_i^{KS} can be given as:

$$h_i^{KS} = -\frac{1}{2}\nabla_i^2 - \sum_k^{nuclei} \frac{Z_k}{|r_i - r_k|} + \int \frac{\rho(r')}{|r_i - r'|} dr' + V_{xc} \quad (2.30)$$

where V_{xc} is the functional derivative of E_{xc}, $V_{xc} = \frac{\delta E_{xc}}{\delta \rho}$.[1,21]

The above mentioned E_{xc} (see equation 2.27), the exchange-correlation energy, is a complex term as it doesn't only define the variation in quantum mechanical and classical electron-electron repulsion but also comprises the difference between the kinetic energy of the system having interacting electrons and that of the system with non-interacting electrons (see equation 2.26). The full solution for the Schrödinger equation can be obtained with the exact value of the exchange-correlation term whose exact nature is still unknown despite trying various functionals[22]. Some of the approximations to solve this problem are mentioned below:

1. **Local-density approximation (LDA):** It solely depends on the local value of the electronic density (ρ) at any position (r) in space to calculate the value of E_{xc} at the same position[23]. Various approaches have been found to give local approximations to E_{xc} but the most successful ones have been obtained from the homogeneous electron gas model (HEG). For the spin-unpolarized system, LDA for E_{xc} can be written as:

$$E_{xc}^{LDA}[\rho(r)] = \int \rho(r)\varepsilon_{xc}\big(\rho(r)\big)\, dr \quad (2.31)$$

   where ε_{xc} is the exchange-correlation energy per particle of HEG of charge density ρ.

2. **Generalized gradient approximation:** The LDA further leads to improved approximations as LDA itself becomes non-uniform in the cases when the density varies rapidly such as in molecules. One approximation is the generalized gradient approximation (GGA) in which E_{xc} depends on the electron gradient as well along with the electron density (ρ)[24] as follows:

$$E_{xc}^{GGA}[\rho(r)] = E_{xc}^{LDA}[\rho(r)] + \Delta E_{xc}\left[\frac{|\nabla\rho(r)|}{\rho^{\frac{4}{3}}r}\right] \quad (2.32)$$

However, this approximation has a well known shortcoming of underestimating the band gaps.

Some functionals in this category are PBE, PW, mPW. In this study, PBE[25] functional has been used.

3. **Meta-GGA:** The development beyond the GGA leads to the meta-GGAs that possess the second derivative of the elctron density[1,26]. It has dependence on the Laplacian of the orbitals, that is, the kinetic energy densities in the system.

$$\tau(r) = \sum_{i}^{occupied} \frac{1}{2}|\nabla\psi_i(r)|^2 \quad (2.33)$$

TPSS, M06L, VSXC are some functions of this type.

4. **Hybrid functionals:** These are widely used functionals that include partial mixing of the Hartree-Fock exchange energy with the DFT energy and provide a major benefit over the GGA, especially with regards to the band gap underestimation[27]. These types of functionals have not been applied for the present work due to their computational cost and the inclusion of large systems which make the computations highly expensive. One of the most common hybrid functionals is B3LYP (Becke 3-parameter exchange functional combined with the Lee–Yang–Parr correlation functional)[28,29]

$$E_{xc}^{B3LYP} = E_x^{LDA} + a_0(E_x^{HF} - E_x^{LDA}) + a_x(E_x^{GGA} - E_x^{LDA}) + E_c^{LDA} + a_c(E_c^{GGA} - E_c^{LDA}) \quad (2.34)$$

where $a_0 = 0.20$, $a_x = 0.72$, and $a_c = 0.81$, E_x^{GGA} is the GGA-B88 exchange functional, E_c^{GGA} is the GGA correlation functional of Lee–Yang–Parr[30], and E_c^{LDA} is the local density approximation correlation functional.

The choice of functional is completely dependent on the type of calculations being performed. The computational cost also impacts the selection of functionals along with the accuracy and efficiency of the computations. The "Jacob ladder of density functional approximations" introduced by J. P. Perdew[31] (see Figure 2.2) provides a good idea of the functionals, starting from Hartree world, in terms of their accuracy and simplicity.

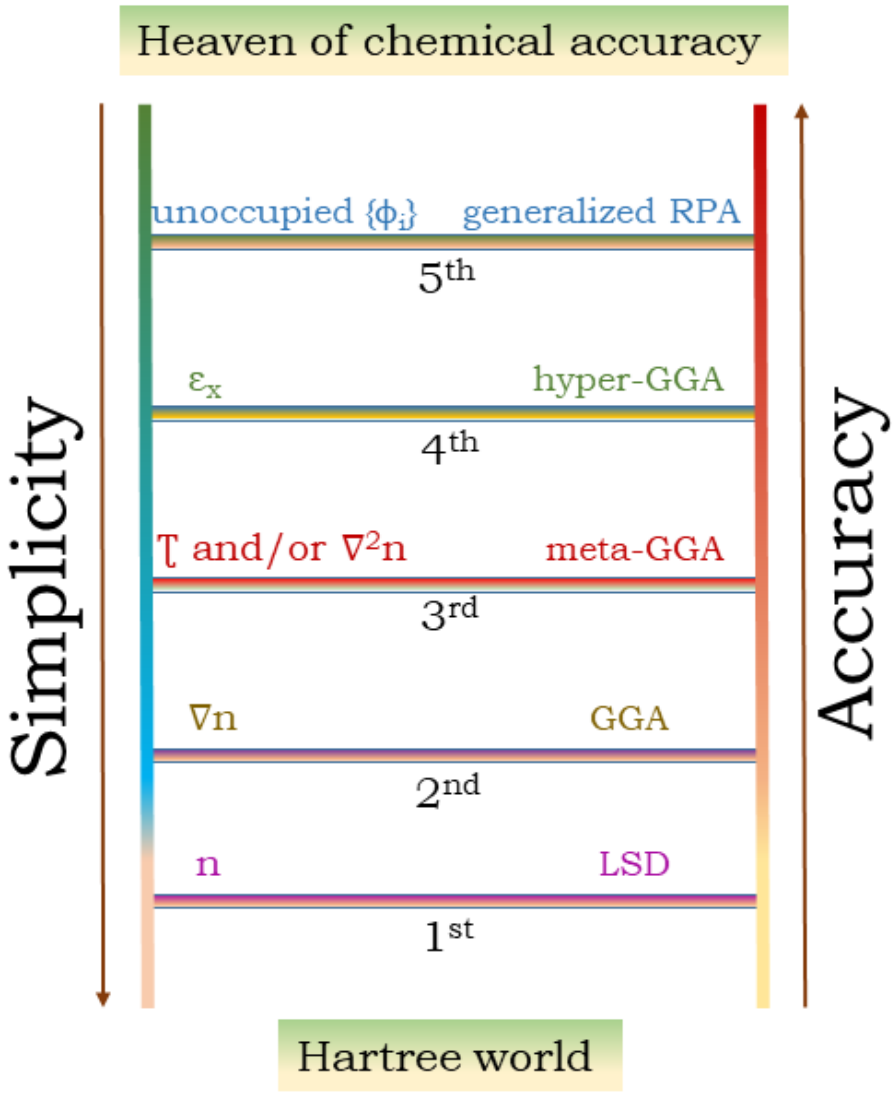

Figure 2.1 Jacob's ladder for the exchange-correlation energy by Perdew[31].

2.6 Basis Sets[1]

The basis sets are basically mathematical sets of (non-orthogonal) functions used to describe MOs and/or the wave functions. Larger basis sets result in fewer restrictions on the wave function thus, giving us a better approximation of the orbitals but they are demanding in terms of computationally cost. The standard basis sets, however, are designed to give the best description at a lower cost. Hence, the level of approximation is directly proportional to the basis sets used in the calculation. The choice of basis set is basically a trade-off between accuracy and computational cost. Each molecular orbital in theory is expressed as linear combinations of the basis functions. The contribution from each atomic orbital to the molecular orbital can be determined from the coefficient C_i.

$$\psi = \sum_{i=1}^{N} C_i \phi_i \tag{2.35}$$

The basis sets either constitute atomic orbitals, highly used in the quantum chemistry community, or plane waves, which are typically used for systems with periodic boundary conditions or solid-state chemistry. The most commonly used types of atomic orbitals are Slater-type orbitals (STOs) and Gaussian-type orbitals (GTOs)

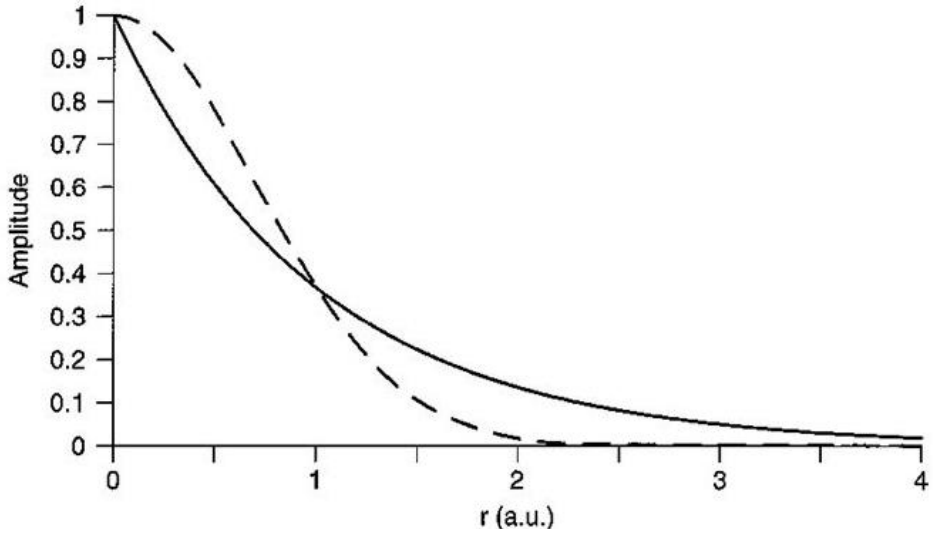

Figure 2.2 Behavior of e-x where x=r for STO (solid line) and x=r2 for GTO (dashed line)[1].

STOs are basically solutions to the the Schrödinger equation for H-like atoms and are decaying exponentially far away from the nucleus. The mathematical form of STOs can be written as:

$$\psi(r,\theta,\emptyset;\zeta,n,l,m) = \frac{(2\zeta)^{n+\frac{1}{2}}}{[(2n)!]^{\frac{1}{2}}} r^{n-1} e^{-\zeta r} Y_l^m(\theta,\phi) \tag{2.36}$$

where n is the principle quantum number for valence orbitals, ζ is the exponent that depends on the atomic number and can be chosen by some certain rules developed by Slater[33], $Y_l^m(\theta,\phi)$ are the spherical harmonics functions where l and m are the angular quantum numbers, and the spherical coordinates are given as $r,\theta,\emptyset$.

The shape of the atomic orbitals (AOs) is better described by STOs than by GTOs. The latter were first introduced by Boys in 1950[19]. The only major advantage of using GTOs over STOs is the faster computations because STOs require numerically calculated integrals during the calculation which costs a lot of time, whereas integrals over GTOs can be computed analytically. STOs obey the cusp condition (see Figure 2.1) and give an accurate electron density at the nucleus, whereas GTO gives the wrong shape of the AOs and become flat near the nucleus. The mathematical equation of GTOs varies from STOs for the variable r in the exponential function which is squared in GTOs (see equation 2.26)

$$\psi(x,y,z;\alpha,i,j,k) = N x^i y^j z^k e^{-\alpha(x^2+y^2+z^2)} \tag{2.37}$$

where the width of Gaussian functions depends on α, N is the normalization factor, and i, j, k are non-negative integers.

In general, there are different levels of basis sets which are required to completely describe electrons in the atom such as single zeta (SZ), double zeta (DZ), triple zeta (TZ), quadruple zeta (QZ), etc. The SZ has one basis function per occupied MO, DZ has two basis functions, and so on.

To get better results with the systems having electron correlation, weak interactions, H-bonds, highly excited states ,or for ionic systems etc., basis sets with polarization and diffuse functions can be used. The core electrons and valence electrons can also be treated separately as inner core electrons are shielded enough to not take part in chemical bond formation.

2.7 Relativistic Effects[1,34]

While working with the heavier elements with a high atomic number in the periodic table, the relativistic effects become crucial. Significant effects in the properties of atoms beyond Kr (Z>36) have been observed due to relativistic effects which come into picture due to the energy variations among electron levels. The mass m, of a moving object can be related to its velocity, v, according to the Einstein theory of relativity as follows:

$$m = m_0 \left(\frac{1-v^2}{c^2}\right)^{-\frac{1}{2}} \tag{2.38}$$

where m_0 is the mass of the object at rest and c is the speed of light. With the high value of velocity for the inner electrons of heavy elements, the mass of the moving electron becomes higher than its rest mass. This rise in mass gives smaller Bohr's radius:

$$a_0 = \frac{\hbar^2}{me^2} \tag{2.39}$$

Hence, it results in the relativistic contraction and stabilization of all *s*- and most of the *p*-orbitals of a many-electron system[35]. The nuclear screening in large atoms due to the contraction of *s*- and *p*-orbitals results in the relativistic expansion and destabilization of *d* and *f*-orbitals. High differences in the chemical properties of periods 5 and 6 of the periodic table are observed due to such effects.

The relativistic effects for the energies of a one-electron system were given by the Dirac in 1929:

$$E\psi = (c.\alpha.p + \beta mc^2 + V)\psi \tag{2.40}$$

where p is the momentum, V is the external potential, α is a vector constructed from the Pauli spin matrices (see 2.41-2.42), β is a 4 x 4 Dirac matrix containing the 2x2 identity matrix I.

$$\alpha = \begin{pmatrix} 0 & \sigma_{x,y,z} \\ \sigma_{x,y,z} & 0 \end{pmatrix} \tag{2.41}$$

$$\sigma_x = \begin{pmatrix} 0 & 1 \\ 1 & 0 \end{pmatrix}, \sigma_y = \begin{pmatrix} 0 & -i \\ i & 0 \end{pmatrix}, \sigma_z = \begin{pmatrix} 1 & 0 \\ 0 & -1 \end{pmatrix} \tag{2.42}$$

$$\beta = \begin{pmatrix} I & 0 \\ 0 & I \end{pmatrix} \tag{2.43}$$

The Dirac equation (see equation 2.44) contains four component wavefunctions. Electronic states have two large components and two small components. The Dirac equation is not only difficult to solve due to the possibility of variational collapse to negative energy states but it is also computationally expensive.

$$\Psi = \begin{pmatrix} \psi_L \\ \psi_S \end{pmatrix} = \begin{pmatrix} \psi_L & \uparrow \\ \psi_L & \uparrow \\ \psi_S & \downarrow \\ \psi_S & \downarrow \end{pmatrix} \tag{2.44}$$

The inclusion of spin-orbit interaction further intensifies the problem. Among various approximations, the zero-order regular approximation (ZORA) to the Dirac equation is widely used. ZORA uses a two-component approach to solve the Dirac equation by avoiding the energy dependence of the effective mass of the electron, regularizing the wave function[36–39]. It is suitable for large component systems[40]. For the periodic systems, effective core potentials (ECP, also

known as pseudopotentials, PP) are used to model relativistic effects. They are discussed in section 2.10.

2.8 Geometry optimization and frequency calculation[1,2]

Geometry optimization is a method of considering an arbitrary rough approximation of the structure as starting point, and performing a series of iterations on the geometry until it gets to the closest local energy minimum on the PES. We get the mathematical relationship between the different geometries of the molecule and their single-point energies by analyzing the PES. Thus, the main objective is to seek stable atomic arrangements by testing various possibilities. This is the initial step in computational modeling of the system which is then followed by other calculations. There are various points which characterize the PES known as stationary points (see Figure 2.3). The highest value in the particular area of PES is termed as 'local maximum' whereas the 'global maximum' is the highest value in the entire PES. Similarly, the lowest value in the specific region is a 'local minimum' and for the entire PES it is the 'global minimum'. The transition states are mainly represented by 'Saddle points' on the PES which are a minimum in one direction and maxima in others, as shown in Figure 2.3. The most stable structure of the geometry is given by the global minimum. The gradient which is the first derivative of the energy with respect to the geometry is zero at the stationary points.

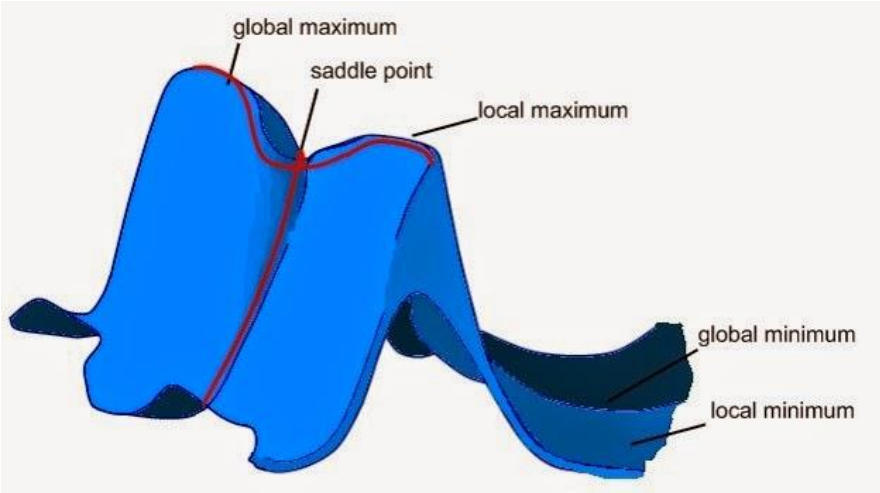

Figure 2.3 The Potential energy surface plot with labeled stationary points on the surface.

To be able to clearly differentiate between stationary points, the second derivatives of the energy with respect to the geometry must be considered and they are known as the 'Hessian (or force) matrix'. The diagonalization of the Hessian matrix results in the normal modes of vibrations that are the eigenvectors of the matrix. The eigenvalues of the mass-weigthed version of the Hessian are the squares of the corresponding vibrational frequencies. The maxima or minima can be determined by the signs of the second derivatives (Hessian eigenvalues) which can be obtained by frequency (second-derivate) calculations. A Hessian matrix with only non-negative eigenvalues represents a 'minimum' whereas, a negative eigenvalue corresponds to an imaginary frequency, and it indicates a 'maximum with respect to one coordinate' or 'saddle point'. For the present work, geometries with all real (not imaginary) frequencies were considered.

2.9 Solvent Effects[2,41]

The clear effects of a solvent environment on the spectra and energies of actinide complexes have been tested and reviewed in the literature[42–44]. The inclusion of solvent results in improved computations which are closer to the real exprimental environment. Because of the strong

interaction between solute and solvent, the properties of the solute which depend on the energy such as optimized geomtery, vibrational frequency, total energy, etc. depends on the type of solvent. There are two ways of modeling chemistry in solution: by using an explicit model or by employing an implicit (continuum) model. The explicit model includes direct and specific interactions of solvent with solute by treating a particular number of solvent molecules around the solute. Although this model provides a resolved picture of the solvent, this approach is computationally demanding especially in the case of heavy and large solutes. The implicit or continuum model, on the other hand, treats the solvent as a structureless medium with certain dielectric and interfacial properties and hence, the number of degrees of freedom is reduced[45,46]. The continuum model is the most widely used model and with the given charge distribution from ab-initio methods like HF, DFT, etc. the solvent is represented as a perturbation to the solute Hamiltonian (see equation 2.45)

$$\hat{H}^{total}(r) = \hat{H}^{molecule}(r) + \hat{V}^{molecule+solvent}(r) \tag{2.45}$$

where r stands for solute molecule coordinates and $\hat{V}^{molecule+solvent}$ is composed of interaction operators.

There are several different types of implicit models, including the following two that are based on similar physical models:

1. Polarized continuum model (PCM)[47,48]
2. Conductor like screening model (COSMO)[49,50]

The PCM considers the solvent as a polarizable continuum. There are further two types of well-known PCM models: the dielectric PCM (D-PCM) in which the continuum is polarizable and the conductor-like PCM (C-PCM) in which the continuum is a conductor just like in the COSMO

model which treats solvent as a continuum with a specific permittivity. I used the COSMO model with water as a solvent for the cluster model calculations.

2.10 Pseudopotentials[2]

For periodic systems, plane-wave basis sets are often used as the potential has the following property in this case:

$$V(r + na) = V(r) \tag{2.46}$$

where a is a lattice vector and n is an integer. According to Bloch's theorem[51], the wavefunction is a product of a cell periodic part and a wavelike part (equation 2.47)

$$\psi_i(r) = e^{ik.r} f_i(r) \tag{2.47}$$

where, k is the quantum number discussed in section 2.11.

The plane-wave basis set can be used to describe the wavefunction for the periodic cell and hence, $f_i(r)$ can be written as:

$$f_i(r) = \sum_G c_{i,G} e^{iG.r} \tag{2.48}$$

where G is the reciprocal lattice vector.

While using plane-wave basis functions, two factors come into play near the atomic nucleus: the electron-nucleus potential varies as $\frac{1}{r}$ and when r approaches zero it diverges towards infinity. Secondly, according to the exclusion principle, the valence electron wavefunctions should be orthogonal to the core electron wavefunctions. This condition is satisfied when the valence wavefunctions oscillate rapidly within the core region, thus, leading to high kinetic energies and eventually a large number of plane waves required in the basis set. These issues are resolved by

the use of the pseudopotential approximation[52] which eliminates the core electrons and merges the interaction between the core and valence electrons and the strong nuclear-valence electron interaction into a weaker pseudopotential. There are various schemes to generate pseudopotentials and the most commonly used are projector augmented wave pseudopotentials (PAW)[53] and ultra-soft pseudopotential (US)[54]. For higher precision and accuracy, PAW pseudopotentials are more famous because they have smaller radial cutoffs, that is, smaller core radii than US pseudopotentials and all nodes in the core region are used to rebuild the exact valence wavefunction in PAW type pseudopotentials[55]. The pseudopotentials account for the most important relativistic effects and decrease the computational costs of calculations involving heavy elements[56].

2.11 Reciprocal Space and the k Quantum Number[2]

In the real space, any position can be defined by a real-space vector R which can be given as the linear combination of three basic vectors a_1, a_2 and a_3 as follows:

$$R = n_1 a_1 + n_2 a_2 + n_3 a_3 \tag{2.49}$$

The reciprocal space is defined as space where a set of fictional points are built in such a way that the direction of a vector intersects with the normal to the real space planes and the separation of these points is proportional to the reciprocal of the real interplanar distance. Just like in equation 2.49, the reciprocal lattice vector K can be constructed from reciprocal basic vectors g_1, g_2, and g_3.

$$K = m_1 g_1 + m_2 g_2 + m_3 g_3 \tag{2.50}$$

According to the definition of reciprocal space:

$$g_1 = \frac{2\Pi}{V}(a_2 \times a_3) \qquad \perp a_2, a_3$$

$$g_2 = \frac{2\Pi}{V}(a_3 \times a_1) \qquad \perp a_3, a_1 \qquad (2.51)$$

$$g_3 = \frac{2\Pi}{V}(a_1 \times a_2) \qquad \perp a_1, a_2$$

where $V = a_1(a_2 \times a_3)$

The unit cell of reciprocal space is defined as the first Brillouin zone (shown in Figure 2.4). It constitutes of k-points in reciprocal space which are close to the origin. The values of these k-points can be obtained from periodic boundary conditions. For better quality of calculations, a large number of k-points are required to integrate over the Brillouin zone because, from the definition of real space and reciprocal space, a small unit cell (real space) corresponds to large reciprocal space (Brillouin zone).

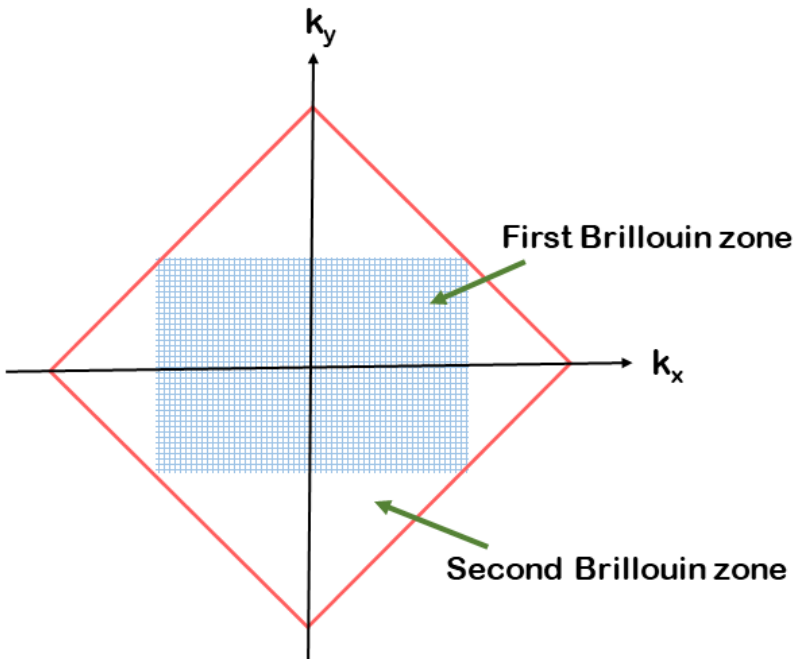

Figure 2.4 The reciprocal space with Brillouin zone[57].

2.12 Band Structure[2]

The electronic band structure is basically a diagram comprised of the orbital energies within the solid as a function of 'k'and thus, has energy bands and energy gaps in the range where electrons don't have their energies. In other words, it is essentially a molecular orbital (MO) diagram with symmetry labels for the translational symmetry. There are various applications of band structures including understanding physical properties of solids such as resistivity, optical absorption which provides knowledge that is useful for various devices such as transistors, solar cells etc.[58,59]

For a periodic crystal lattice, the band structure calculation includes the Schrödinger equation solved for an electron, giving Bloch waves as solutions:

$$\psi_{nk}(r) = e^{ik.r} u_{nk}(r) \tag{2.52}$$

where k is a wave vector, and n is the band index. For each k, there are many solutions of the Schrödinger equation labeled as n that is, the number of the bands.

The wave vector occupies any value in the Brillouin zone (see Figure 2.5). Special symmetry points with the Brillouin zone are labeled as Γ, Δ, Λ, Σ, etc. For instance, Γ is the center of the Brillouin zone and other high symmetry points vary according to the type of the crystal lattice.

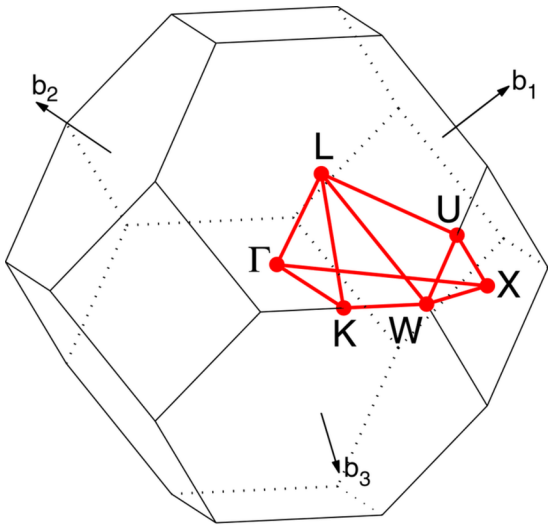

Figure 2.5 First Brillouin zone of an FCC crystal where b1, b2, and b3 are reciprocal base vectors[60]. (Reproduced with permission from reference 60. Copyright 2010 Computional Materials Science, Elsevier.)

2.13 Mayer Bond Order Analysis[1,61]

Various classical chemical ideas such as bond multiplicity, atomic charges, etc. are employed to test the bonding in molecules. The bond order is one of the most useful tools to get the fractional as well as non-fractional values from the output of quantum mechanical simulations. Among different types of bond orders, Mayer bond order (MBO) which is an extended version of the Wiberg bond order has proven highly useful in bonding analysis using semi-empirical computational methods, as well as for DFT and ab initio methods. MBO[62] is basically defined as:

$$B_{kk'} = \sum_{\mu \in k} \sum_{\nu \in k'} (PS)_{\mu\nu}(PS)_{\nu\mu} \tag{2.53}$$

where $B_{kk'}$ is the Mayer bond order value for the bond between k and k' atoms, P and S are the usual density and overlap matrices, respectively, and hence, the product PS is the Mulliken population. Due to the direct relation of MBO with the Mulliken population, there is a basis set dependence in the MBO as well. For homonuclear diatomics, equation 2.53 leads to integer values when small basis sets are used but, for more complicated systems and large basis sets, noninteger values have been observed which shows the ionic character of bonds as well as delocalization and multicentre effects[60,63]. In the present study, non-integer values of MBO have been observed as we are dealing with heavy metal actinide complexes which have shown bonding with 2D layers.

The equation 2.53 is suitable for restricted closed-shell calculations but, with the inclusion of the spin density, the definition of the MBO is as follows:

$$B_{kk'} = B^{\alpha}_{kk'} + B^{\beta}_{kk'} = 2\sum\nolimits_{\mu\in k}\sum\nolimits_{\nu\in k'}[\,(P^{\alpha}S)_{\mu\nu}(P^{\alpha}S)_{\nu\mu} + \left(P^{\beta}S\right)_{\mu\nu}\left(P^{\beta}S\right)_{\nu\mu}] \tag{2.54}$$

where P^{α} and P^{β} are the alpha and beta spin density matrix respectively.

2.14 Hirshfeld Atomic Charges[1,64]

Hirshfeld charges are basically the difference between a molecule and the unrelaxed atomic charge densities and hence, can be explained relative to the deformation density. Hirshfeld, in 1977, proposed the use of a "promolecule" composed of spherically symmetric neutral atoms at the coordinates of the atoms in the real molecule. He calculated the charge density at any point about the real molecule and the corresponding point about the promolecule as follows:

$$\rho_{promolecule}(r) = \sum\nolimits_{A}^{M_{Atoms}} \rho_{A}^{atomicdensity}(r) \tag{2.54}$$

The weighing factor w_A depends on how big the atomic density contribution is and can be given as:

$$w_A = \frac{\rho_A^{atomicdensity}(r)}{\rho_{promolecule}(r)} \tag{2.55}$$

Finally, the Hirshfeld charge Q_A on the atom can be obtained by using the following equation:

$$Q_A = Z_A - \int w_A(r)\rho_{molecule}(r)\,dr \tag{2.56}$$

where Z_A is the nuclear charge.

The biggest advantage of using Hirshfeld charges is the fact that, when the molecular deformation density converges to the true solution, the computed net charges will necessarily converge[65]. We

have used Hirshfeld charges to evaluate the amount of charge transfer resulting from the adsorption of actinide complexes on different types of 2D materials in the cluster model.

Bibliography

1. Cramer, C. J. *Essentials of computational chemistry : theories and models*. (Wiley, 2004).
2. Dronskowski, R. *Computational chemistry of solid state materials : a guide for materials scientists, chemists, physicists and others*. (Wiley-VCH, 2005).
3. Choppin, G. R. Actinide speciation in the environment. *J. Radioanal. Nucl. Chem.* **273**, 695–703 (2007).
4. Jensen, M. P. & Choppin, G. R. Complexation of Uranyl(VI) by Aqueous Orthosilicic Acid. *Radiochim. Acta* **82**, 83–88 (1998).
5. Jensen, F. & Frank. *Introduction to computational chemistry*. (John Wiley & Sons, 2007).
6. Dreizler, R. M. & Gross, E. K. U. *Density Functional Theory : an Approach to the Quantum Many-Body Problem*. (Springer Berlin Heidelberg, 1990).
7. Neal, H. L. Density functional theory of one-dimensional two-particle systems. *Am. J. Phys.* **66**, 512–516 (1998).
8. Pyykkö, P. Relativistic effects in structural chemistry. *Chem. Rev.* **88**, 563–594 (1988).
9. Schrödinger, E. An Undulatory Theory of the Mechanics of Atoms and Molecules. *Phys. Rev.* **28**, 1049–1070 (1926).
10. Born, M. & Oppenheimer, R. Zur Quantentheorie der Molekeln. *Ann. Phys.* **389**, 457–484 (1927).
11. Gordon, A. & Avron, J. E. Born-Oppenheimer Approximation near Level Crossing. *Phys. Rev. Lett.* **85**, 34–37 (2000).
12. Pisana, S. *et al.* Breakdown of the adiabatic Born–Oppenheimer approximation in graphene. *Nat. Mater.* **6**, 198–201 (2007).
13. Sommerfeld, T. Lorentz Trial Function for the Hydrogen Atom: A Simple, Elegant Exercise. *J. Chem. Educ.* **88**, 1521–1524 (2011).
14. Griffiths, D. J. *Introduction to quantum mechanics*. (Pearson Prentice Hall, 2005).
15. Hartree, D. R. The Wave Mechanics of an Atom with a Non-Coulomb Central Field. Part I. Theory and Methods. *Math. Proc. Cambridge Philos. Soc.* **24**, 89–110 (1928).
16. Hartree, D. R. The Wave Mechanics of an Atom with a Non-Coulomb Central Field. Part II. Some Results and Discussion. *Math. Proc. Cambridge Philos. Soc.* **24**, 111–132 (1928).
17. Roothaan, C. C. J. New Developments in Molecular Orbital Theory. *Rev. Mod. Phys.* **23**, 69–89 (1951).
18. Hay, P. J. & Martin, R. L. *Computational Studies of Actinide Chemistry*. *Los Alamos Science Number* **26**,

19. Boys, S. F. Electronic wave functions - I. A general method of calculation for the stationary states of any molecular system. *Proc. R. Soc. London. Ser. A. Math. Phys. Sci.* **200**, 542–554 (1950).

20. Hohenberg, P. & Kohn, W. Inhomogeneous Electron Gas. *Phys. Rev.* **136**, B864–B871 (1964).

21. Kohn, W. & Sham, L. J. Self-Consistent Equations Including Exchange and Correlation Effects. *Phys. Rev.* **140**, A1133–A1138 (1965).

22. Cohen, A. J., Mori-Sánchez, P. & Yang, W. Challenges for Density Functional Theory. *Chem. Rev.* **112**, 289–320 (2012).

23. Leeuwen, R. Van & Baerends, E. J. An analysis of nonlocal density functionals in chemical bonding. *Int. J. Quantum Chem.* **52**, 711–730 (1994).

24. Perdew, J. P., Burke, K. & Ernzerhof, M. Generalized Gradient Approximation Made Simple. *Phys. Rev. Lett.* **77**, 3865–3868 (1996).

25. Perdew, J. P., Burke, K. & Ernzerhof, M. Generalized Gradient Approximation Made Simple. *Phys. Rev. Lett.* **77**, 3865–3868 (1996).

26. Tao, J., Perdew, J. P., Staroverov, V. N. & Scuseria, G. E. Climbing the Density Functional Ladder: Nonempirical Meta–Generalized Gradient Approximation Designed for Molecules and Solids. *Phys. Rev. Lett.* **91**, 146401 (2003).

27. Becke, A. D. A new mixing of Hartree–Fock and local density- functional theories. *J. Chem. Phys.* **98**, 1372–1377 (1993).

28. Becke, A. D. Density- functional thermochemistry. III. The role of exact exchange. *J. Chem. Phys.* **98**, 5648–5652 (1993).

29. Kim, K. & Jordan, K. D. Comparison of Density Functional and MP2 Calculations on the Water Monomer and Dimer. *J. Phys. Chem.* **98**, 10089–10094 (1994).

30. Lee, C., Yang, W. & Parr, R. G. Development of the Colle-Salvetti correlation-energy formula into a functional of the electron density. *Phys. Rev. B* **37**, 785–789 (1988).

31. Perdew, J. P. *et al.* Prescription for the design and selection of density functional approximations: More constraint satisfaction with fewer fits. *J. Chem. Phys.* **123**, 062201 (2005).

32. Mardirossian, N. & Head-Gordon, M. ωB97X-V: A 10-parameter, range-separated hybrid, generalized gradient approximation density functional with nonlocal correlation, designed by a survival-of-the-fittest strategy. *Phys. Chem. Chem. Phys.* **16**, 9904 (2014).

33. Slater, J. C. Atomic Shielding Constants. *Phys. Rev.* **36**, 57–64 (1930).

34. Thayer, J. S. Relativistic Effects and the Chemistry of the Heaviest Main-Group Elements. *J. Chem. Educ.* **82**, 1721 (2005).

35. Pyykkö, P. Relativistic Effects in Chemistry: More Common Than You Thought. *Annu. Rev. Phys. Chem.* **63**, 45–64 (2012).

36. Lenthe, E. van, Ehlers, A. & Baerends, E.-J. Geometry optimizations in the zero order regular approximation for relativistic effects. *J. Chem. Phys.* **110**, 8943–8953 (1999).

37. Lenthe, E. van, Baerends, E. J. & Snijders, J. G. Relativistic regular two- component Hamiltonians. *J. Chem. Phys.* **99**, 4597–4610 (1993).

38. Lenthe, E. van, Baerends, E. J. & Snijders, J. G. Relativistic total energy using regular

approximations. *J. Chem. Phys.* **101**, 9783–9792 (1994).

39. Lenthe, E. van, Snijders, J. G. & Baerends, E. J. The zero- order regular approximation for relativistic effects: The effect of spin–orbit coupling in closed shell molecules. *J. Chem. Phys.* **105**, 6505–6516 (1996).

40. Autschbach, J. *et al.* Computational Tools for Predictive Modeling of Properties in Complex Actinide Systems. in *Computational Methods in Lanthanide and Actinide Chemistry* 299–342 (John Wiley & Sons Ltd, 2015).

41. Young, D. C. *Computational Chemistry*. (John Wiley & Sons, Inc., 2001).

42. Fortier, S. & W.Hayton, T. Oxo ligand functionalization in the uranyl ion (UO22+). *Coord. Chem. Rev.* **254**, 197–214 (2010).

43. Arnold, P. L., Pécharman, A.-F. & Love, J. B. Oxo Group Protonation and Silylation of Pentavalent Uranyl Pacman Complexes. *Angew. Chemie Int. Ed.* **50**, 9456–9458 (2011).

44. Graves, C. R. & Kiplinger, J. L. Pentavalent uranium chemistry—synthetic pursuit of a rare oxidation state. *Chem. Commun.* 3831 (2009).

45. Tomasi, J., Mennucci, B. & Cammi, R. Quantum Mechanical Continuum Solvation Models. *Chem. Rev.* **105**, 2999–3094 (2005).

46. Zhang, J., Zhang, H., Wu, T., Wang, Q. & van der Spoel, D. Comparison of Implicit and Explicit Solvent Models for the Calculation of Solvation Free Energy in Organic Solvents. *J. Chem. Theory Comput.* **13**, 1034–1043 (2017).

47. Cossi, M., Rega, N., Scalmani, G. & Barone, V. Polarizable dielectric model of solvation with inclusion of charge penetration effects. *J. Chem. Phys.* **114**, 5691–5701 (2001).

48. Cossia, M., Barone, V., Cammi, R. & Tomasi, J. Ab initio study of solvated molecules: a new implementation of the polarizable continuum model. *Chem. Phys. Lett.* **255**, 327–335 (1996).

49. Mennucci, B. & Tomasi, J. Continuum solvation models: A new approach to the problem of solute's charge distribution and cavity boundaries. *J. Chem. Phys.* **106**, 5151–5158 (1997).

50. Klamt, A. Conductor-like Screening Model for Real Solvents: A New Approach to the Quantitative Calculation of Solvation Phenomena. *J. Phys. Chem.* **99**, 2224–2235 (1995).

51. Blakemore, J. S. (John S. *Solid state physics*. (Cambridge University Press, 1985).

52. Yin, M. T. & Cohen, M. L. Theory of *ab initio* pseudopotential calculations. *Phys. Rev. B* **25**, 7403–7412 (1982).

53. Blöchl, P. E. Projector augmented-wave method. *Phys. Rev. B* **50**, 17953–17979 (1994).

54. Vanderbilt, D. Soft self-consistent pseudopotentials in a generalized eigenvalue formalism. *Phys. Rev. B* **41**, 7892–7895 (1990).

55. Kresse, G. & Joubert, D. From ultrasoft pseudopotentials to the projector augmented-wave method. *Phys. Rev. B* **59**, 1758–1775 (1999).

56. Fuentealba, P., Reyes, O., Stoll, H. & Preuss, H. Ground state properties of alkali and alkaline–earth hydrides. *J. Chem. Phys.* **87**, 5338–5345 (1987).

57. Mizia, J. & Górski, G. *Models of itinerant ordering in crystals : an introduction*. (Elsevier, 2007).

58. Proot, J. P., Delerue, C. & Allan, G. Electronic structure and optical properties of silicon crystallites: Application to porous silicon. *Appl. Phys. Lett.* **61**, 1948–1950 (1992).

59. Hubbard, J. & Dalton, N. W. The approximate calculation of electronic band structures II. Application to copper and iron. *J. Phys. C Solid State Phys.* **1**, 321 (1968).

60. Setyawan, W. & Curtarolo, S. High-throughput electronic band structure calculations: Challenges and tools. *Comput. Mater. Sci.* **49**, 299–312 (2010).

61. Bridgeman, A. J., Cavigliasso, G., Ireland, L. R. & Rothery, J. The Mayer bond order as a tool in inorganic chemistry†. *J. Chem. Soc. Dalt. Trans.* 2095–2108 (2001).

62. Bridgeman, A. J. & Rothery, J. Bonding in mixed halogen and hydrogen peroxides. *J. Chem. Soc. Dalt. Trans.* **0**, 4077–4082 (1999).

63. Bridgeman, A. J. & Rothery, J. Periodic trends in the diatomic monoxides and monosulfides of the 3d transition metals. *J. Chem. Soc. Dalt. Trans.* 211–218 (2000).

64. Hirshfeld, F. L. Bonded-atom fragments for describing molecular charge densities. *Theor. Chim. Acta* **44**, 129–138 (1977).

65. Davidson, E. R. & Chakravorty, S. A test of the Hirshfeld definition of atomic charges and moments. *Theor. Chim. Acta* **83**, 319–330 (1992).

Chapter 3

Adsorption of actinide (U-Pu) complexes on the silicene and germanene surface – A theoretical study

3.1 Abstract

Adsorption of actinide (Ac) complexes with environmentally relevant ligands on silicene and germanene surfaces has been investigated using density functional theory to determine the geometrical, energetic and electronic properties. Three types of ligands for each central metal atom are considered: OH^-, NO_3^- and CO_3^{2-} with common oxo ligands in all cases. Among these, carbonate complexes show the strongest adsorption followed by hydroxide and nitrate. Two types of model, cluster and periodic models, have been considered to include the short- and long-range effects. The cluster and periodic models are complementary, although the former has not yet been widely used for studies of 2D materials. Two cluster sizes have been investigated to check size dependency. Calculations were performed in the gas phase and water solvent. Based on the adsorption energy, for the CO_3^{2-} and OH^- ligands, the bond position between two Si atoms in the silicene sheet is the most strongly adsorbed site in the cluster model for silicene whereas in the periodic model these complexes exhibit strong binding on the Si atom of the silicene surface. The Ac-complexes with the NO_3^- ligand show strong affinity at the hollow space at the center of a hexagonal ring of silicene in both models. The H-site is most favorable for the binding of complexes on the germanene cluster whereas, these sites vary in the periodic model. Electronic

structure calculations have been performed which show a bandgap range from 0.130 to 0.300eV for the adsorption of actinide complexes on silicene that can be traced to charge transfer. Density of States calculations show that the contribution of the nitrate complexes is small near the Fermi level but it is larger for the carbonate complexes in the silicene case. Strong interactions between Ac-complexes and silicene are due to the formation of strong Si—O bonds upon adsorption which results in reduction of the actinide atom. Such bonding is lacking in germanene.

3.2 Introduction

Graphene, one of the most fascinating nanomaterials known, has gained a fair amount of attention since its isolation and characterization due to its promising applications that result from its exceptional physical and chemical properties. Its applications span various fields from electronics to biotechnology, due to its high mechanical strength, massless Dirac Fermions, high carrier mobility, and so on.[1–3] However, the lack of cost-effective techniques to produce high-quality single-layered graphene, the presence of zero bandgap, challenges with its incorporation into Si-based technology, etc. have led to enhanced efforts of locating other 2-dimensional (2D) materials.[4–6] Being in the same group IV in the periodic table as C, 2D-Si is a natural target material. Recent years have also witnessed a strong interest in the 2D material of the next element in the group, germanene, which is made up of a single layer of germanium atoms[7,8]. C, Si, and Ge have a lot of similarities due to the presence of the same valence electron configurations $2s^2 2p^2$, $3s^2 3p^2$ and $4s^2 4p^2$ respectively. Moreover, the high compatibility of silicene to Si-based nano-technology and its outstanding inherited properties from graphene make it highly interesting.[9–11]

Theoretical calculations have demonstrated a buckled honeycomb lattice structure for silicene and germanene which differentiates them from planar graphene.[12] The partially hybridized sp^2-sp^3 Si

and Ge atoms result in a distorted hexagonal honeycomb lattice of silicene and germanene whose electronic properties and bandgap can be easily modified.[13–16] The presence of buckling in the hexagon of the higher atomic number germanium as compared to carbon and silicon has been attributed to the large increase in spin-orbit coupling in germanene.[17,18] The magnitude of the spin-orbit interaction has been reported as 46.3 meV, 4 meV, and 1 μeV for germanene, silicene, and graphene, respectively.[19] The interactions between 2D materials and different chemical moieties have found a large number of applications in various fields.[20,21] Various studies reported huge modifications in electronic and structural properties of germanene and silicene by different chemical species.[15,22–24] The most effective and widely used methodology involves adsorbing complexes on the 2D sheet. The mechanism of this method involves the breaking of the lattice symmetry which further resulted from the charge transfer between adsorbent and adsorbate and hence, opens a bandgap in the 2D material.[15] Recent results from various studies have shown stronger binding affinity of chemical species for silicene and germanene as compared to graphene.[22–26] Various gas molecules (such as NH_3, NO, NO_2, SO_2, and O_2) that have been reported chemically inert to graphene show strong chemisorption in the case of silicene[27] and germanene[28]. Van der Waals density functional theory calculations have been performed by Kaloni et al. to understand the interactions between small organic molecules such as acetone, acetonitrile, ammonia, benzene, etc. and the silicene surface with and without doping.[22] Furthermore, alkali metal-adsorbed germanene has been found to have acquired metallic character with a Dirac point moving below the Fermi level and hence, opening a small gap without destroying its electronic properties.[23] Comparison between hypothetical planar and existing buckled silicene by using first-principles simulations shows strong adsorption of Fe and Cr on buckled silicene, thus revealing the benefits of a buckled structure.[29] Several projects have focused on the adsorption of 3d, 4d, 5d

metal complexes on both types of 2D materials[24,25,30–32] but, to the best of our knowledge, adsorption of 5f metal complexes has not yet been investigated for the silicene and germanene surfaces.

Actinides (Ac) can be found in the core of nuclear reactors along with other fission products and, hence, are a crucial part of nuclear energy. They impose a major risk on geological repositories because of their long lives and radioactivity. Contamination of the surroundings of repositories and other nuclear sites, mainly through the groundwater, due to nuclear waste is a major environmental concern.[33,34] Recent work in nanoscience and materials science has led to great advances in the separation of actinides by graphene and carbon-based nanotubes. Various reports have not only shown the ability of graphene to adsorb contaminated ionic products in solution (water) but also in the gaseous environment.[3,35–37] In 2014, Wang et al. evaluated the adsorption of the actinide complex uranium carbide on pristine and doped graphene by employing density functional theory (DFT) calculations.[38,39] Due to the increasing applications of functionalized graphene-like GO (graphene oxide) in nuclear waste management, the actinide ions were adsorbed on a GO sheet as well.[40] Periodic trends along the actinide series (Th-Cm) for the adsorption onto graphene clusters have been reported recently in 2017 with a detailed explanation of interactions occurring between the radioactive metal atom and a $C_{54}H_{18}$ graphene cluster. The Th atom shows stronger interaction with graphene as compared to other members of the series, resulting from the strong overlap between Th (6d) and C (2p) orbitals.[41]

A lot of effort has been invested into the study of adsorption of actinides onto graphene but, as already stated, similar work for silicene and germanene is missing. The current study can prove quite effective for radioactive material sensing technology as well as for the extraction from seawater of uranium which is the most critical component for nuclear power production. In recent

years, a large number of methods to recover uranium from seawater and aqueous solution have been proposed, such as coprecipitation[42], ion- exchange adsorption[43], and organic-inorganic hybrid adsorbents[44,45]. The most convenient and cost-effective methodology is by adsorption processes.[46,47] In the present work, equatorial ligands and complexes have been chosen by keeping both their environmental relevance and neutral charge in mind. Specifically, we have considered the complexes $[AcO_2(OH)_2]$, $[AcO_2(NO_3)_2]$ and $[AcO_2(CO_3)]$, Ac = U, Np, and Pu. Two models have been investigated, the cluster model and the periodic model, to study the short-range and long-range interactions. First-principles calculations were performed to investigate the geometrical, energetic and electronic properties (band structure). The periodic trends for U-Pu for different types of complexes have been observed.

3.3 Computational Details

The structural relaxation and electronic properties calculations were performed in the framework of approximate DFT, as implemented in the ADF software[48] for the cluster model calculations and in the PWSCF-code[49] for periodic model simulations, within the generalized gradient approximation[50] in the form of the Perdew, Burke, and Ernzerhof (PBE) functional. To have a better description of the non-covalent interactions between the 2D surface and adsorbed complexes, the dispersion corrected density functional theory (DFT-D3) proposed by Grimme[51] along with BJ damping[52,53] (D3BJ) to include the effects of non-bonded intramolecular dispersion was employed in both models. Germanene has strong spin-orbit interactions (SOI); accordingly, it has been taken into account for the germanene simulations.

For the cluster calculations, relativistic effects were included with ZORA (Zeroth Order Regular Approximation),[54,55] and a triple-ζ uncontracted Slater-type orbital (STO) basis set with two

polarization functions (TZ2P) with small frozen core were used.[56] Different spin multiplicities were investigated to locate the ground state. The charge transfer between the adsorbed complex and 2D sheet was computed by using Hirshfeld charges.[57] QTAIM[58,59] and Mayer bond order analysis (MBO) was used to verify and understand the nature of some interactions upon adsorption.[60] The systems were fully optimized followed by vibrational frequency analysis to ensure the presence of local minima on the potential energy surface (PES). Both gas phase and solvation calculations with water as a solvent were done for the cluster model. For the water solvent calculations, optimized structures from gas phase were re-optimized within the conductor like screening solvation model (COSMO)[61–63] at the same level of theory. The parameters for water solvent (radius 1.93 Å and dielectric constant 78.39) were used. The solvation calculations are particularly important to understand the binding of uranium complexes which have been found to be present in huge amounts in seawater.[64]

In the periodic model, Brillouin zone integration has been performed by choosing a Monkhorst-Pack 24 × 24 × 1 k-mesh grid for a supercell having dimensions of 4 × 4 × 1 with a lattice constant of 15.44 Å for silicene and 16.24 Å for germanene. To avoid artificial interactions occurring between adjacent periodic images, a vacuum region of 20 Å in the z-direction was used. Projector augmented wave pseudopotentials[65] for each type of atoms were employed. All atomic forces were converged to less than 1×10^{-3} eV/Å and a high plane wave cut off energy of 816 eV was employed. The settings chosen for the present study are similar to previous studies on silicene and germanene.[22,24] The amount of charge transfer from/to silicene was evaluated by Löwdin population analysis.[66]

To evaluate the stability of adsorption of actinide complexes on 2D surface, the adsorption energy was calculated by using the following formula in both models

$$E_{adsorption}(eV) = E_{2D+molecule} - (E_{2D} + E_{molecule})$$

where $E_{2D+molecule}$, $E_{2D,}$ and $E_{molecule}$ are the total energies of the combined silicene/germanene and Ac-complex, the 4 × 4 × 1 pristine silicene/germanene supercell or the cluster, and the adsorbed Ac-complex respectively. By using this definition, a negative value of $E_{adsorption}$ indicates strong adsorption, whereas a positive value indicates repulsion.

3.4 Results and Discussion

Two types of models can be used to represent extended systems: cluster models and periodic models. In the cluster model, the 2D surface has been represented by a finite piece (a flake) of the material just like its analog graphene which has been represented by six peri-fused benzene rings known as Coronene.[67,68] In the periodic model, periodic boundary conditions (PBC) will come into play for modeling an infinite system.[69] The latter is the most common method for studying the adsorption of species onto 2D materials. For the flake model of silicene, two sizes have been considered to investigate the effect of model size on the interactions of Ac-complexes with silicene. One has the molecular formula $Si_{42}H_{16}$ and the other $Si_{64}H_{20}$ (see Figure 3.1). In both clusters, hydrogen termination has been used to satisfy the dangling bonds. The calculations of adsorption of Ac-complexes on the two flakes $Si_{42}H_{16}$ and $Si_{64}H_{20}$ show similar effects on geometrical parameters of silicene after adsorption but they vary slightly in their adsorption energies (see Appendix, Tables S1-S3). So, for germanene only the $Ge_{42}H_{16}$ cluster size (see Figure S1) has been considered. In the following, we will discuss in detail the adsorption of Ac-complexes on the $Si_{42}H_{16}$ and $Ge_{42}H_{16}$ flakes in a water solvent.

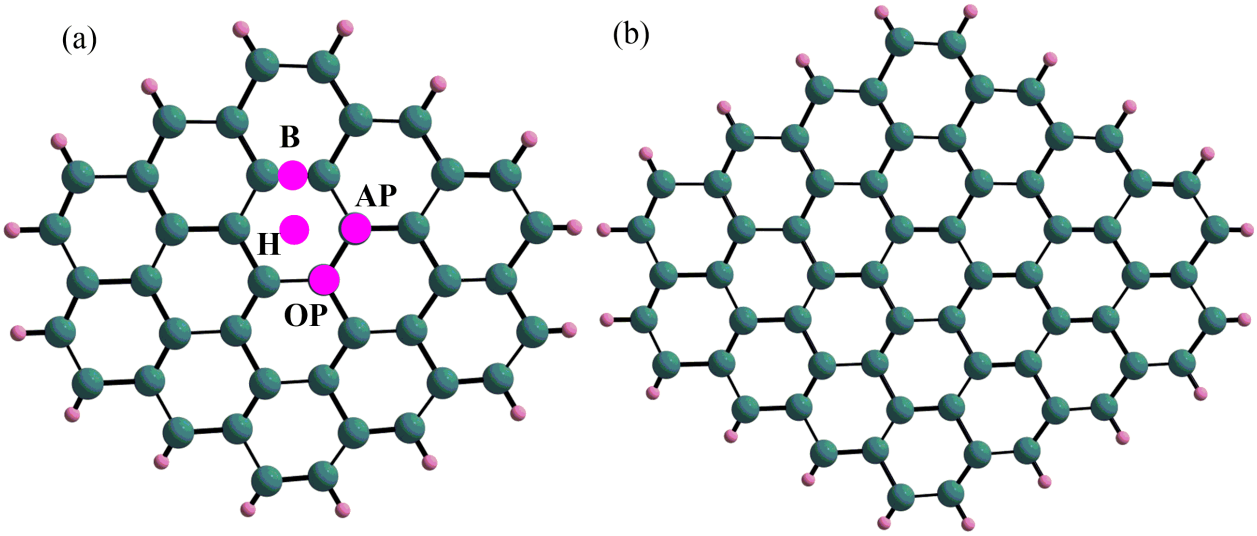

Figure 3.1 Optimized structures of the silicene flakes (a) $Si_{42}H_{16}$ and (b) $Si_{64}H_{20}$ respectively. The adsorption sites are shown on the $Si_{42}H_{16}$ flake.

To understand the most stable binding structure of Ac-complexes on both silicene and germanene, four possible binding positions have been considered in both types of models for both surfaces, namely, on top of the bond between neighboring Si/Ge atoms (B), on top of the hollow site of a hexagon (H), on top of a Si/Ge atom which is on the plane (OP) and on top of at Si/Ge atom which is above the plane of silicene/germanene (AP), see Figure 3.1. Various initial conformations have been covered by treating different atoms present in an Ac-complex on possible anchoring positions.

3.4.1 Structural Description.

Cluster Model. Different coordination environments of Ac-complexes ($[UO_2(OH)_2]$, $[UO_2(NO_3)_2]$, $[UO_2(CO_3)]$, $[NpO_2(OH)_2]$, $[NpO_2(NO_3)_2]$, $[NpO_2(CO_3)]$, $[PuO_2(OH)_2]$, $[PuO_2(NO_3)_2]$ and $[PuO_2(CO_3)]$) with different types of central metal and equatorial ligands including OH^-, NO_3^-, and CO_3^{2-} at four different adsorption sites (Figure 3.1) have been considered. Gas phase calculations were performed to obtain faster convergence and optimized structures were

then reoptimized under solvation conditions. The most favorable cases obtained in water solvent for the silicene flake are shown in Figure 3.2, and their corresponding geometrical parameters are collected in Table 3.1. The distance between the adsorbed Ac-complex and silicene sheet d (Å), the hexagonal Si—Si—Si angle , Θ (degree), the Si—Si bond length after adsorption (Å) and the buckling parameter which is the average perpendicular distance between neighboring Si atoms, Δ (Å), are summarized in Table 3.1. Upon adsorption, the structural parameters of pristine silicene have been hugely modified, indicating strong interactions. After adsorption, the Si–Si bond length has a range of 2.25-2.36 Å in the hydroxide complexes, 2.26-2.37 Å for nitrate complexes and 2.25-2.37 Å for carbonate complexes of U, Np and Pu adsorbed on silicene. This can be compared to a value of 2.27 Å for the pristine flake, Table 3.1. As a result of adsorption, the hexagonal angle Θ and the buckling Δ of pristine silicene have changed significantly, from 115º and 0.47 Å to 98-118º, 96-117º, 98-117º, and 0.35-0.69 Å, 0.39-0.69 Å and 0.38-0.68 Å for $[AcO_2(OH)_2]$, $[AcO_2(NO_3)_2]$ and $[AcO_2(CO_3)]$ complexes respectively. The average distance between hydroxide complexes of Ac and silicene after adsorption is 3.41 Å, whereas for nitrate and carbonate complexes the average distances are 3.50 Å and 3.38 Å respectively. The coordination number of the central metal atom is contributing towards these observations as there are larger steric effects in six-coordinate nitrate complexes as compared to carbonate and hydroxide, leading to the long Ac–silicene distance. Furthermore, from the literature, hydroxide has been found to be a stronger equatorial ligand[70–72], thus supporting our findings of a longer distance for hydroxide than for carbonate. There is an increase in distance between the silicene flake and central metal atom as we move from U to Np to Pu complexes for each type of ligand (see Table 3.1). It occurs due to the presence of strong ligand-surface interactions in the case of Pu complexes where we have found strong Si—O bonding resulting in significant elongation of the Pu—O bonds as compared to Np—

O followed by U—O. This can be related to a weakening of the axial Ac–O bond along the actinide series U, Np, Pu.[73] Hence, the central atom moves farther away from the silicene surface. The geometries and structural parameters for the gas phase calculations are summarized in Tables S4-S6 and Figure S2.

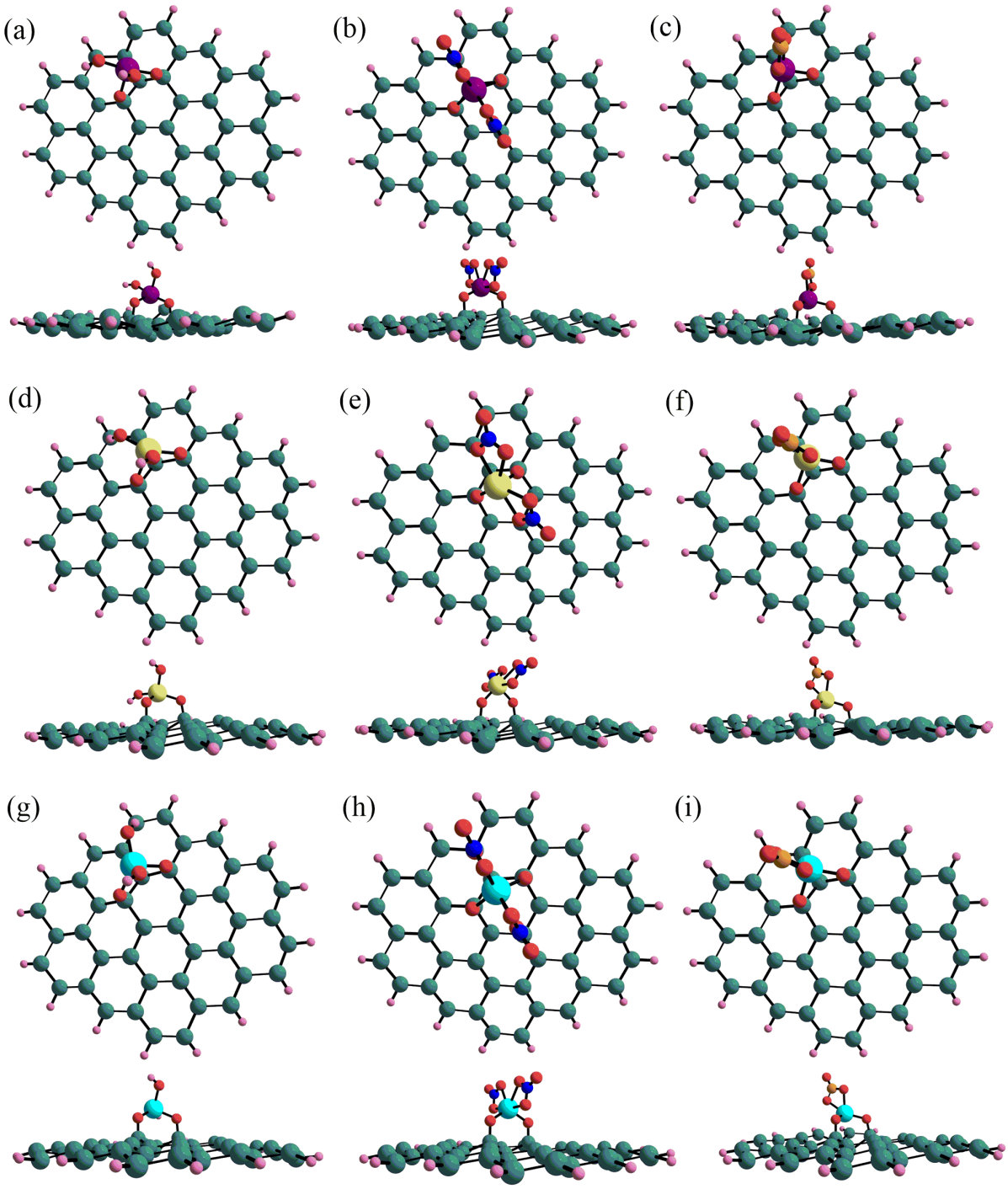

Figure 3.2 Top and side views of the optimized solvated structures in water for (a) $[UO_2(OH)_2]$, (b) $[UO_2(NO_3)_2]$, (c) $[UO_2(CO_3)]$, (d) $[NpO_2(OH)_2]$, (e) $[NpO_2(NO_3)_2]$, (f) $[NpO_2(CO_3)]$, (g) $[PuO_2(OH)_2]$, (h) $[PuO_2(NO_3)_2]$ and (i) $[PuO_2(CO_3)]$ on $Si_{42}H_{16}$ flake.

System	d (Å)	Θ (deg)	Si—Si (Å)	Δ (Å)	E_{ad} (eV)	Q (e)
Silicene	--	115	2.27	0.47	--	--
$UO_2(OH)_2$	3.24	98-115	2.25-2.35	0.35-0.61	-0.998	0.388
$NpO_2(OH)_2$	3.50	105-117	2.25-2.36	0.41-0.63	-1.331	0.457
$PuO_2(OH)_2$	3.52	104-118	2.26-2.35	0.41-0.69	-1.920	0.595
$UO_2(NO_3)_2$	3.27	103-117	2.26-2.35	0.39-0.69	-0.914	0.356
$NpO_2(NO_3)_2$	3.61	96-115	2.26-2.34	0.40-0.68	-1.237	0.421
$PuO_2(NO_3)_2$	3.64	98-117	2.26-2.37	0.38-0.67	-1.787	0.590
$UO_2(CO_3)$	3.18	100-116	2.25-2.37	0.45-0.68	-1.398	0.465
$NpO_2(CO_3)$	3.47	105-117	2.25-2.37	0.42-0.64	-1.763	0.578
$PuO_2(CO_3)$	3.51	98-117	2.26-2.37	0.38-0.67	-2.211	0.894

Table 3.1 Structural parameters, adsorption energy and amount of charge transfer from the silicene flake to Ac-complex for the most strongly adsorbed site in aqueous solvation.

For the $Ge_{42}H_{16}$ flake in water solvent, the most stable optimized geometries can be seen in Figure S3, and geometry parameters are summarized in Table 3.2. The calculated hexagonal angle in the pristine $Ge_{42}H_{16}$ flake in solvation is 112° with a Ge—Ge bond length of 2.43Å and buckling parameter of 0.69Å which matches a previous (periodic) study on germanene.[24] The buckling parameter of pristine germanene is much larger than that of silicene (Table 3.1), concomitant with a smaller hexagonal angle. The calculated average distance (see Table 3.2) between the sheet and complex is 3.32 Å for hydroxide, 3.55 Å for nitrate, and 3.28 Å for carbonate complexes. This follows the same pattern as for the silicene flake with nitrate complexes having a larger distance from the surface compared to carbonate and hydroxide. After the adsorption, some of the Ge atoms

above the plane can be seen slightly further up (Figure S3), along with the turning of the flake into a bowl-shaped structure, resulting in modified structural parameters. Similar bowl-shaped structures were also observed in the case of silicene, although they tend to belong to higher energy (less stable) structures. Test calculations show that dispersion-corrected functionals are required to capture this effect; it was not observed with non- dispersion-corrected functionals. The hexagonal angle lies in the range of 96-120° after interaction with Ac-complexes. Both, shortening as well as elongation of Ge—Ge bond lengths occurs. These bond lengths have a new range of 2.40-2.52 Å (see Table 3.2). The buckling parameter has a maximum value of 1.23Å upon the adsorption of Ac-complexes. Regarding the periodic trends in terms of distance between the complex and Ge-flake, the Pu-complexes are closest as compared to Np and U-complexes which is opposite to what we observed in the case of silicene as well as borophene[74]. The reason behind this is the absence of strong Ge—O bonds upon adsorption as is the case for silicene and borophene. As a result, the effect of the actinide contraction is more prominent and dominating. Calculated parameters for gas phase calculations of the $Ge_{42}H_{16}$ flake can be seen in Tables S7-S9.

System	d (Å)	Θ (deg)	Ge—Ge(Å)	Δ (Å)	E_{ad} (eV)	Q (e)
$Ge_{42}H_{16}$	--	112	2.43	0.69	--	--
$UO_2(OH)_2$	3.57	99-120	2.42-2.49	0.77-0.86	-0.592	0.578
$NpO_2(OH)_2$	3.24	99-120	2.43-2.50	0.68-0.96	-0.784	0.721
$PuO_2(OH)_2$	3.15	100-120	2.43-2.50	0.77-1.05	-1.315	0.912
$UO_2(NO_3)_2$	3.70	102-118	2.42-2.44	0.65-0.90	-0.380	0.345
$NpO_2(NO_3)_2$	3.49	97-118	2.41-2.50	0.63-0.97	-0.495	0.530
$PuO_2(NO_3)_2$	3.46	97-117	2.42-2.50	0.61-0.99	-0.846	0.894
$UO_2(CO_3)$	3.52	96-119	2.40-2.51	0.73-0.96	-0.630	0.683
$NpO_2(CO_3)$	3.21	97-117	2.41-2.52	0.61-1.22	-0.899	0.906
$PuO_2(CO_3)$	3.12	96-116	2.40-2.52	0.62-1.23	-1.537	1.090

Table 3.2 Geometrical parameters, adsorption energy E_{ad} (eV) and amount of charge transfer (Q) from flake to Ac-complex (in electron) of the most stable site for the adsorption on $Ge_{42}H_{16}$ flake in water solvent.

On comparing gas phase and solvation results for both Si and Ge flakes, large adsorption energies were observed in gas phase (see Tables 3.1, 3.2, S6 and S9). There is a larger Ac-surface distance in solvation as compared to gas phase indicating weaker adsorption in solvation. In both environments, the AP site is the least stable for adsorption.

For the silicene cluster, the most stable conformations have two newly formed bonds (see Figure 3.2) between the oxo ligands present in $[AcO_2(OH)_2]$, $[AcO_2(NO_3)_2]$ and $[AcO_2(CO_3)]$ complexes and the Si atoms. Other, less stable, conformations contain either zero or one Si—O bond. These bonds result because of the presence of buckling in the silicene structure which is not the case in graphene; this may be the reason that the adsorption of $[UO_2]^{2+}$ on functionalized graphene oxides lacks such bonding.[75] Qualitatively similar results were also seen in the case of buckled and planar borophene where the former one is having strong adsorption interactions with the formation of two B—O bonds with actinides while the latter one has only one B—O bond[74]. The two Si-O bonds lead to the reduction of the central metal atom which is further supported by the direction of charge transfer (discussed below). The presence of these bonds has been verified by MBO analysis.[60] The Si–O bond order values for the hydroxide complexes of U, Np and Pu on the silicene flake fall in the range 0.43 to 0.53, whereas, for nitrate and carbonate complexes, this value varies from 0.41 to 0.52 and 0.42 to 0.53 respectively (see Table 3.3). An increase in the bond order value corresponding to an increase in the strength of the Si—O bonds can be seen as we move from U to Pu complexes (Table 3.3) which is also evident from the decrease in Si—O bond lengths along the series. There is a decrease in bond strength for Ac—O bonds where Ac= U, Np, Pu for each type of ligand which justifies the elongation of the Ac—O bond as we go down from U to Pu. Table 3.3 has values for Ac—O bond lengths before and after adsorption showing large elongation in Pu—O bond lengths for each type of ligand with values 2.16 to 2.18 Å whereas, for the Np—O

bond, the values range from 2.14-2.16 Å, and the U—O bond length has a range 2.08-2.10 Å. This is in contrast to normal actinyl complexes where the Ac–O bond lengths generally follow the actinide contraction. The weakening of the Ac—O bond upon adsorption can be further analyzed by the MBO values which represent the bond strength before and after adsorption (see Table 3.3). From the data it can be seen that the double bond present between Ac and the actinyl oxygen (O) is converting to a single bond (or less) upon adsorption. This goes along with the newly formed Si—O bonds. For the germanene flake, on the other hand, the Ge—O bonds are quite weak (see Table S10). The Ge—O bond lengths lie in the range of 1.99-2.13 Å, which is much longer than the Si—O bond lengths (1.65-1.71 Å).

Ac-Complex − $Si_{42}H_{16}$	**Ac—O (□)**		**MBO (Ac—O)**		**Si—O (□)**	**MBO (Si—O)**
	Before	**After**	**Before**	**After**		
$UO_2(OH)_2$	1.81	2.10	1.84	0.45	1.69	0.44
$NpO_2(OH)_2$	1.80	2.15	1.88	0.41	1.66	0.50
$PuO_2(OH)_2$	1.79	2.17	1.95	0.37	1.65	0.52
$UO_2(NO_3)_2$	1.78	2.08	1.95	0.50	1.71	0.41
$NpO_2(NO_3)_2$	1.78	2.16	1.96	0.39	1.67	0.45
$PuO_2(NO_3)_2$	1.77	2.16	2.01	0.38	1.65	0.51
$UO_2(CO_3)$	1.79	2.09	1.94	0.43	1.69	0.45
$NpO_2(CO_3)$	1.77	2.14	1.97	0.42	1.66	0.49
$PuO_2(CO_3)$	1.77	2.18	1.98	0.37	1.65	0.53

Table 3.3 Bond lengths of Ac-complexes before and after adsorption along with the Mayer bond order (MBO) values and bond length of newly formed Si—O bonds with bond order values.

Periodic Model. The structural changes upon adsorption of the Ac-complexes on the silicene surface in periodic calculations are summarized in Table 3.4, and the optimized geometries can be

seen in Figure S4. The average distance between the silicene sheet and the hydroxide and carbonate complexes has been found to be 3.16 Å, and for nitrate complexes, it has been observed as 3.22 Å. The adsorbed molecules are slightly closer to the sheet in the periodic case as compared to the cluster model with an average difference of 0.2 Å. There is a lot of structural reconstruction as a result of adsorption in the PBC case as well, including modification of the hexagonal angle of silicene, which has been changed from 116º to 106-117º, 105-118º, and 107-118º for hydroxide, nitrate and carbonate Ac-complexes. The Si—Si bond lengths upon adsorption reaches a maximum value of 2.37 Å for hydroxide Ac-complexes and it shows variation from 2.27 to 2.36 Å for nitrate as well as carbonate complexes. The buckling increases around the region of adsorption because of the newly formed Si—O bonds which lift the Si atoms slightly higher above the plane of silicene. Hence, buckling has changed from 0.48 Å to 0.45-0.69 Å, 0.41-1.67 Å and 0.44-0.69 Å for $[AcO_2(OH)_2]$, $[AcO_2(NO_3)_2]$ and $[AcO_2(CO_3)]$ adsorbed on silicene respectively. There is an elongation of the bond between Ac and O atoms after interactions with silicene. A huge lengthening of the Pu—O bonds has been observed, from 1.73-1.76 to 2.07-2.09 Å for each type of ligand whereas, for Np—O the range after adsorption is 1.98-2.02 Å and the U—O has new bond length values that fall within the range 1.97-2.01 Å. Both cluster and PBC model show large elongation for the Pu—O bond as compared to Np—O followed by U—O. The Si—O bond lengths fall into the range of 1.66 -1.79 Å with a decrease in bond length as we go from U to Pu for each ligand which is quite similar to the cluster model except that bond lengths in PBC are somewhat larger, probably due to the difference in the choice of relativistic method. (see Table S11).

System	d (Å)	Θ (deg)	Si—Si (Å)	Δ (Å)
Silicene	--	116	2.27	0.48
$UO_2(OH)_2$	3.12	106-117	2.28-2.36	0.50-0.64
$NpO_2(OH)_2$	3.18	106-117	2.28-2.36	0.45-0.62
$PuO_2(OH)_2$	3.20	105-117	2.27-2.37	0.45-0.69
$UO_2(NO_3)_2$	3.19	105-118	2.28-2.35	0.46-0.63
$NpO_2(NO_3)_2$	3.23	105-118	2.28-2.35	0.41-0.63
$PuO_2(NO_3)_2$	3.26	105-117	2.27-2.34	0.46-0.67
$UO_2(CO_3)$	3.11	107-118	2.27-2.36	0.47-0.68
$NpO_2(CO_3)$	3.16	107-117	2.27-2.35	0.44-0.69
$PuO_2(CO_3)$	3.22	107-117	2.27-2.36	0.48-0.69

Table 3.4 Structural parameters for the pristine silicene and silicene after adsorption for the systems under study for PBC calculations.

The optimized geometries of the 4×4×1 supercell containing 32 Ge atoms and one Ac carbonate complex can be seen in Figure 3.3. (See Figure S5 for the nitrate and hydroxide systems.) The structural parameters for the most favorable conformation of each complex adsorbed on germanene are summarized in Table S12. The hexagonal angle, Ge—Ge bond length and buckling in the pristine germanene supercell is in very good agreement with previous reports.[18,24,76] The structural relaxation simulations result in an average distance between complexes and 2D sheet of 3.30 Å, 3.52 Å, and 3.27 Å for hydroxide, nitrate and carbonate complexes respectively. For each type of ligand, results are quite similar to the cluster model in that the Pu-complexes are closer to the 2D germanene layer followed by Np-complexes, and finally, U-complexes. This is due to the lack of strong chemisorption; thus, the actinide contraction comes into play. There is a huge alteration in the hexagonal angle of germanene upon adsorption as for hydroxide complexes it lies in the range of 103-114° whereas the minimum value is 110° for nitrate complexes and 109° for carbonate complexes with the same maximum angle of 114°. The Ge—Ge bond lengths are mainly elongated resulting in variable bond lengths with a maximum value of 2.54 Å. As a result of the slightly upward as well as downward movement of Ge atoms due to binding of Ac-complexes, the

buckling parameter changed from its original value. For hydroxide complexes, it lies in the range of 0.61-0.82 Å whereas for nitrate and carbonate systems, this range is 0.65-0.81 Å, and 0.63-0.88 Å respectively. The Ge—O and Ac—O bond lengths are collected in Table S13.

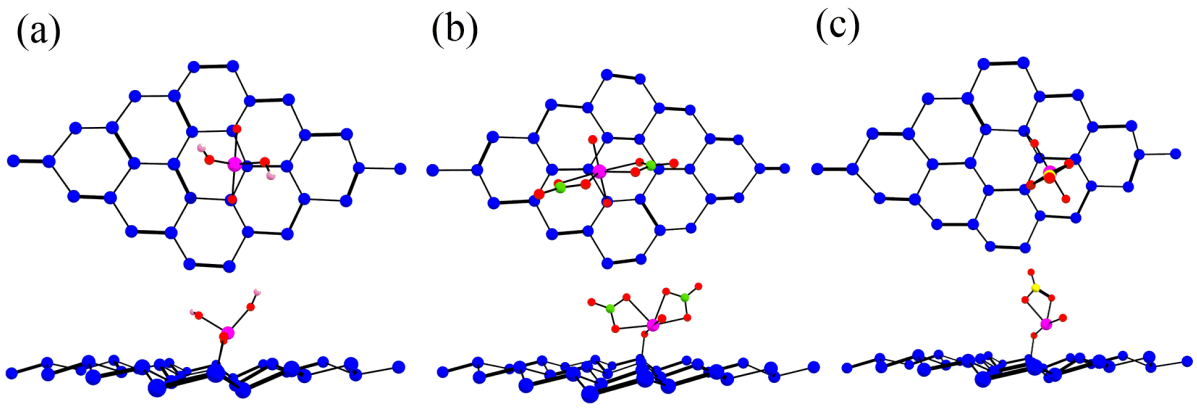

Figure 3.3 Top view and side view of relaxed structures of (a) $[PuO_2(OH)_2]$, (b) $[PuO_2(NO_3)_2]$, and (c) $[PuO_2(CO_3)]$ adsorbed on germanene under PBC.

In summary, in both types of models for silicene, the strongly adsorbed cases have bidentate surface coordination of Ac-complex with two ligands pointing down and bonded to two alternate above-plane Si atoms, and the other ligands pointing upwards away from the silicene surface. For germanene, although surface coordination is weak, there is a huge alteration in the structural parameters of the 2D surface because of physiosorption of actinide complexes.

3.4.2 Adsorption Energy. Silicene has shown minor as well as major geometry changes upon the adsorption of Ac-complexes. These alterations indicate strong adsorption interactions and hence, large negative adsorption energies.

Cluster Model. Adsorption energies and the amount of charge transfer in water solvent for the cluster model can be found in Table 3.1 and in Table S14 where adsorption energies of the four anchoring positions named according to the position of the central metal atom after adsorption on silicene (Figure 3.1) have been summarized. Not surprisingly[77], the adsorption energies are

significantly higher for gas phase calculations (see Table S14). For the cluster model, hydroxide complexes of U and Np show the strongest adsorption when the central metal atom is on the B-site with adsorption energy (E_{ad}) values of -0.998 eV and -1.331 eV respectively. The $[PuO_2(OH)_2]$ shows much stronger binding with silicene for the same site as compared to $[UO_2(OH)_2]$ and $[NpO_2(OH)_2]$ with an E_{ad} value of -1.920 eV. The data for the nitrate complexes show a similar periodic trend but here, the H-site is the most favorable one which may be due to the steric effects as $[AcO_2(NO_3)_2]$ has a larger number of equatorial bonds than the others. The values of E_{ad} for nitrate complex of U, Np and Pu were found to be -0.914 eV, -1.237 eV, -1.787 eV respectively. Among all types of ligands considered in the study, the carbonate ligands show the strongest adsorption interactions on the B-site with values of -1.398 eV, -1.763 eV and -2.211 eV for U, Np and Pu complexes respectively. On comparing different sites with each other for each complex, weaker/longer Si—O bonds were found at the H and OP-sites for hydroxide and carbonate as compared to the B-site but no Si—O bonds were seen on the AP-site which, as a consequence, shows larger differences of 0.8-1.2 eV in adsorption energy from the most favorable site. The bond length values of Si—O and Ac—O for the less favorable sites for all systems and geometries for $UO_2(CO_3)$ adsorption are summarized in Table S15 and Figure S6 respectively. Similarly, for nitrate complexes, B-site and OP-site contain weaker Si—O bonds but the AP site has no such bonding at all and, thus, is least favorable. Overall, carbonate complexes are more strongly adsorbed than hydroxide complexes which are further followed by nitrate complexes of actinides which is also supported by the bond lengths and bond orders, as discussed above (Table 3.3). There is a formation of strong Si—O bonds and hence, elongated and weaker Ac—O bonds. This effect is strongest in case of carbonate complexes followed by hydroxide and nitrate complexes respectively. Furthermore, this is also evident from the amount of charge transfer obtained from

Hirshfeld charges: Generally, the stronger the adsorption, the higher the charge transfer. The charge transfer is taking place from silicene to adsorbed Ac-complex and the values for the most favorable site are collected in Table 3.1. The direction of charge transfer indicates the presence of ionic bonding which is further supported by QTAIM analysis (see Table S16) where we have found values of the electron density at the bond critical point (BCP) of $\rho < 0.2$ and the Laplacian of the density, $\nabla^2\rho > 0$, for the Si—O bonds in the most strongly adsorbed carbonate complexes which signifies ionic bonding.[58] The spin density plots (Figure S6) and spin density values on Ac (Table S17) show the reduction of central metal actinide atom upon adsorption as the spin value for U, Np and Pu changes from 0 to 1.29-1.84, 1.14 to 3.13-3.48 and 2.24 to 4.54-4.85 electron respectively.

The most favorable site for the complexes adsorbed on $Ge_{42}H_{16}$ in water is the H-site for each case (see Figure S3). The adsorption energy for the hydroxide complexes has values of -0.592, -0.784, and -1.315 eV for U, Np, and Pu systems respectively (see Figure 3.4 and Table 3.2). For the nitrate case, the Pu-complex is most strongly adsorbed with an energy value of -0.846 eV as compared to U and Np complexes which have binding energies of -0.380 and -0.495 eV respectively. Among the different types of ligands, the carbonate complexes are again most strongly adsorbed, having maximum adsorption interactions in $PuO_2(CO_3)$ with an energy of -1.537 eV whereas $UO_2(CO_3)$ and $NpO_2(CO_3)$ exhibited -0.630 and -0.899 eV as adsorption energies. The trends show stronger binding in Pu-complexes followed by Np and U-complexes. Regarding the ligands, the carbonate complexes are most strongly adsorbed followed by hydroxide and nitrate which can be attributed to the different coordination numbers and ligand strengths as discussed above. These trends are in good agreement with those of the similar size silicene flake that is, $Si_{42}H_{16}$. However, the adsorption strength is quite low in case of the germanene flake as

compared to the silicene flake. Further, the amount of charge transfer from $Ge_{42}H_{16}$ to Ac-complexes (see Table 3.2) is supporting the results from adsorption energy analysis with a the maximum charge transfer of 1.090 electron in case of $PuO_2(CO_3)$.

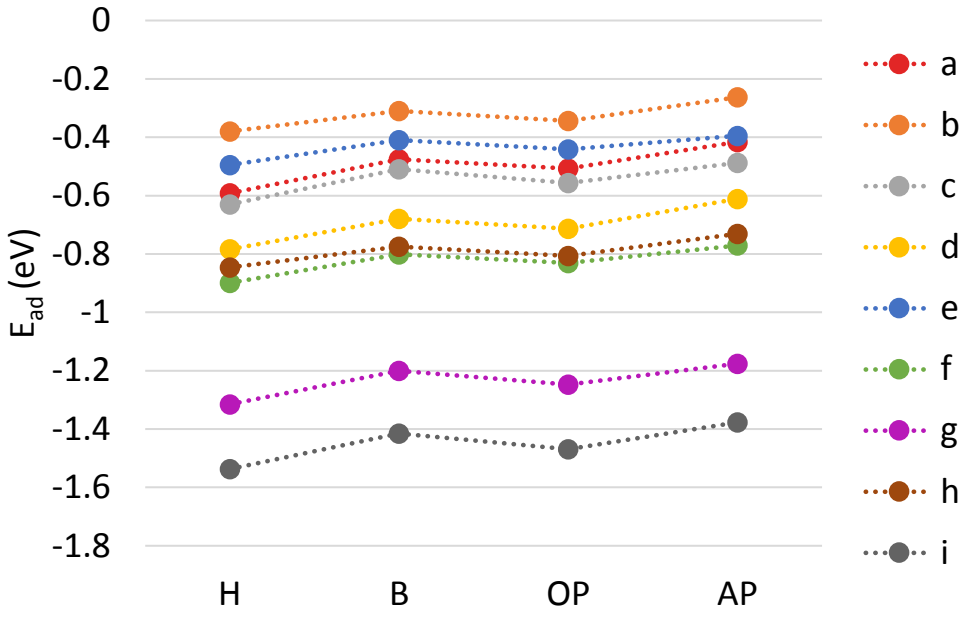

Figure 3.4 Adsorption energies at different possible sites in terms of position of the central metal atom for (a) $[UO_2(OH)_2]$, (b) $[UO_2(NO_3)_2]$, (c) $[UO_2(CO_3)]$, (d) $[NpO_2(OH)_2]$, (e) $[NpO_2(NO_3)_2]$, (f) $[NpO_2(CO_3)]$, (g) $[PuO_2(OH)_2]$, (h) $[PuO_2(NO_3)_2]$, and (i) $[PuO_2(CO_3)]$ complexes adsorbed on $Ge_{42}H_{16}$ in aqueous solvation.

The analysis of adsorption energies at four possible sites (see Figure 3.4) for each complex shows a maximum difference of around 4-5 kcal/mol for the H-site and A-site which is much lower variation than what we obtained for the silicene system. The difference in adsorption energy between the H-site with B- and O-sites is comparatively less as all these sites have weak Ge—O bonds (see Table S10). For the hydroxide complexes, the Ac—O bond is elongated the most in the case of Pu with the formation of a new but weak Ge—O bond with bond length 2.00 Å. For the nitrate complexes, no Ge—O bond formation was observed for the U-complex, whereas it was observed for both Np and Pu with long bond lengths of 2.04 and 2.02 Å respectively. Similarly,

the Pu complex containing a carbonate ligand has the strongest Ge—O bond among the various complexes with bond strength of 0.32 and Ge—O bond length of 1.99 Å which is, however, still a very weak bond compared to the silicene case. On comparing different ligands, the carbonate complexes show stronger chemisorption as compared to hydroxide followed by nitrate ligands, again qualitatively similar to the silicene case.

Periodic Model. For the periodic calculations, similar trends as in the cluster model have been observed for the strength of adsorption of the carbonate, hydroxide and nitrate complexes in both the silicene and germanene systems. For the silicene surface, the hydroxide and carbonate complexes show strong binding affinity at the OP-site whereas, the nitrate complexes are strongly adsorbed at the H-site. The AP-site is the least favorable in all systems as this site does not allow for Si—O bond due to the inappropriate position of the central metal atom and oxo ligands for the formation of Si—O bonds. In this particular site, the metal is situated on the above-plane Si. As a result, the O atoms are positioned either on the H-site or on the OP site, i.e. above Si atoms which are on the plane of silicene; neither position facilitates the formation of Si–O bonds. On comparing with the cluster model, the H-site is favorable for the nitrate complexes in both types of model whereas for carbonate and hydroxide complexes the B-site is preferable in the cluster model and the OP-site for the periodic model. The obtained values of E_{ad} vary from -0.885 to -2.590 eV (Table 3.5). The charge transfer values indicating reduction of the central Ac metal atom from +6 to +4 oxidation state which is also supported by the MBO values in Table 3 and the spin density plots.

Silicene -Ac-complex	H-site	B-site	OP-site	AP-site	Q	Band gap
$UO_2(OH)_2$	-1.234	-1.203	-1.306	-0.219	1.76	0.155
$NpO_2(OH)_2$	-1.729	-1.698	-1.781	-0.516	1.88	0.206
$PuO_2(OH)_2$	-2.115	-2.065	-2.165	-0.798	2.26	0.258
$UO_2(NO_3)_2$	-0.885	-0.799	-0.832	-0.001	1.69	0.130
$NpO_2(NO_3)_2$	-1.365	-1.300	-1.329	-0.215	1.82	0.179
$PuO_2(NO_3)_2$	-2.001	-1.943	-1.907	-0.749	2.13	0.190
$UO_2(CO_3)$	-1.639	-1.601	-1.684	-0.421	1.90	0.248
$NpO_2(CO_3)$	-1.924	-1.894	-1.995	-0.774	1.98	0.259
$PuO_2(CO_3)$	-2.521	-2.491	-2.590	-0.958	2.37	0.300

Table 3.5 Adsorption energy (in eV) of the optimized structures with the central atom at four different sites (H-site, B-site, OP-site, and AP site), amount of charge transfer from surface to the adsorbate (in electron), and band gap (in eV) for the most favorable anchoring site for silicene under PBC.

In case of germanene, the most stable conformations for the hydroxide complexes were found to be at the O- site, B-site, and H-site with calculated adsorption energy values of -0.422 eV, -0.585 eV, and -1.143 eV for U, Np and Pu complexes respectively (see Figure 3.5). For these complexes, one weak Ge—O bond was seen in the optimized structure for each case (see Figures 3.3 and S5). In $[PuO_2(OH)_2]$, the Pu—O bond is elongated slightly, to 1.90 Å at most (see Table S13), along with the formation of a stronger Ge—O bond (2.02 Å) as compared to $[UO_2(OH)_2]$ and $[NpO_2(OH)_2]$ and hence, stronger adsorption. For the nitrate complexes, the adsorption energy is relatively lower than for hydroxide complexes as well as carbonate complexes. The values lie in the range of -0.259 to -0.558 eV, with the central metal atom on the B-site in $[UO_2(NO_3)_2]$ and $[NpO_2(NO_3)_2]$, whereas the most stable structure is the H-site in $[PuO_2(NO_3)_2]$ in the fully relaxed geometry. In terms of Ge—O bond formation, no bond was observed in case of nitrate complexes except that in $[PuO_2(NO_3)_2]$, the Ge—O bond distance was found to be 2.14 Å which is significantly shorter than is observed in $[UO_2(NO_3)_2]$ and $[NpO_2(NO_3)_2]$. The calculated data shows that the carbonate complexes are most strongly adsorbed with E_{ad} values of -0.507 eV for

the U complex at the H-site, -0.680 eV for the N- system on the B-site, and -1.456 eV for the Pucomplex on the H-site. The Ac—O bond has been elongated the most for $PuO_2(CO_3)$ (1.92 Å) with the formation of one Ge—O bond having a bond distance of 1.96 Å. Further, the charge transfer values (see Table S12) agree well with the results from the adsorption energy analysis. There is a maximum charge transfer of 1.618 electron from 2D germanene to $[PuO_2(CO_3)]$. The trends are quite similar to what we obtained in the case of silicene but the strength of adsorption is much lower for germanene as the most stable structure in case of silicene [i.e. $PuO_2(CO_3)$] has an adsorption energy of -2.590 eV which is more negative by 1.134 eV than in germanene case.

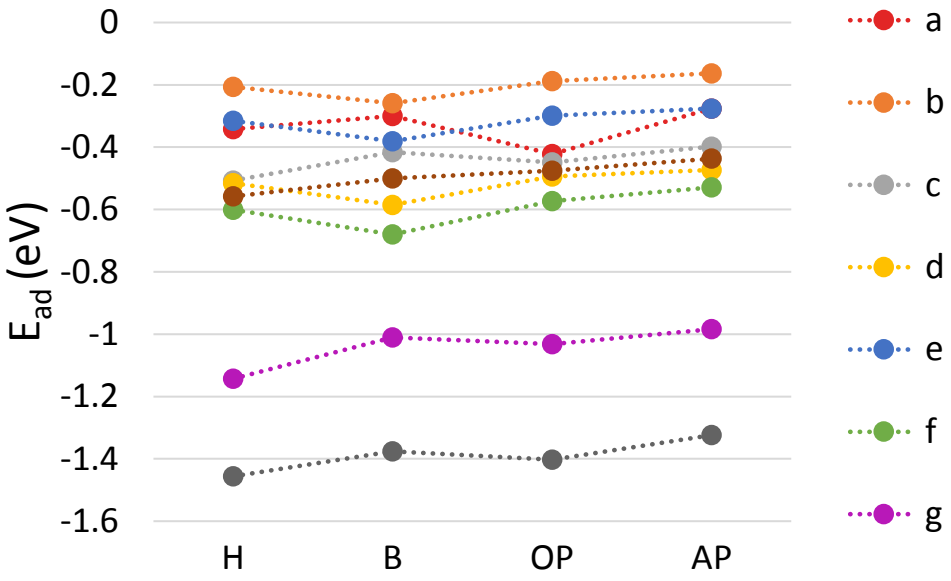

Figure 3.5 Calculated adsorption energies (PBC) at different possible sites in terms of position of the central metal atom for (a) $[UO_2(OH)_2]$, (b) $[UO_2(NO_3)_2]$, (c) $[UO_2(CO_3)]$, (d) $[NpO_2(OH)_2]$, (e) $[NpO_2(NO_3)_2]$, (f) $[NpO_2(CO_3)]$, (g) $[PuO_2(OH)_2]$, (h) $[PuO_2(NO_3)_2]$, and (i) $[PuO_2(CO_3)]$ complexes adsorbed on germanene.

The binding affinity between silicene and Ac-complexes is much stronger than for various other adsorbents that have been studied in the literature, including small organic molecules adsorbed on the same surface with a maximum adsorption energy of -0.949 eV for toluene.[14] The reason for the very strong binding interactions in the present case is found in the formation of strong Si—O

bonds upon adsorption. Formation of one Ge—O bond (2.02 Å) upon adsorbing NO_2 on germanene has been observed[28], but the adsorption energy is -1.08 eV and hence, our results indicate much stronger binding interactions. Further, studies of adsorption of actinide complexes on borophene have shown similar trends and the highest adsorption energy value is -2.584 eV for $PuO_2(CO_3)$[74] which is comparable to what we have found for here for the silicene case. Hence, silicene could be a suitable host material for such type of radioactive actinide complexes.

C. Electronic Structure. The electronic structure of the narrow gap semiconductors, silicene and germanene, can be hugely influenced by the adsorption of different functional groups.[22,67,79] The electronic band structures for pristine silicene and germanene including SOI were calculated. Calculated band gap values are 1.93 meV and 24.4 meV respectively (see Figure S8) which agrees well with the literature.[22,24] The electronic structures of Ac-complex adsorbed on silicene are illustrated in Figure 6. The bandgap has been hugely modified by the adsorption of Pu-complexes. [$PuO_2(CO_3)$] shows the strongest structural distortions which result in gap opening of 0.300 eV (see Figure 6). This is followed by [$PuO_2(OH)_2$] and [$NpO_2(CO_3)$] binding on silicene with gaps of 0.258 and 0.259 eV respectively. These results are supported by the adsorption energy calculations: Stronger adsorption leads to higher charge transfer which results in breaking of the sublattice symmetry and hence gives rise to the opening of a gap at the Dirac point. Thus, the band gap of pristine silicene has been significantly changed by actinide adsorption and hence, these results could in principle be useful for electronic applications of silicene such as high-performance silicene field-effect transistors. Among U, Np and Pu complexes, the U-complexes show the weakest interactions with a relatively small gap opening of 0.155 eV, and 0.130 eV for hydroxide and nitrate ligands (see Figure 3.6 and Table 3.5) respectively. The carbonate complex of uranium shows a more significant band gap as compared to its hydroxide and nitrate complexes with the

gap value of 0.248 eV. The values for the bandgap opening at the Dirac point for Np complexes adsorbed on silicene lie in between the values obtained for U and Pu complexes. We have observed the largest amount of charge transfer of about 2.37 electron from the silicene to the [$PuO_2(CO_3)$] complex, inducing a large bandgap, and the smallest amount of charge transfer (1.69 electrons) for [$UO_2(NO_3)_2$] inducing a small bandgap. (see Figure 3.6 and Table 3.5).

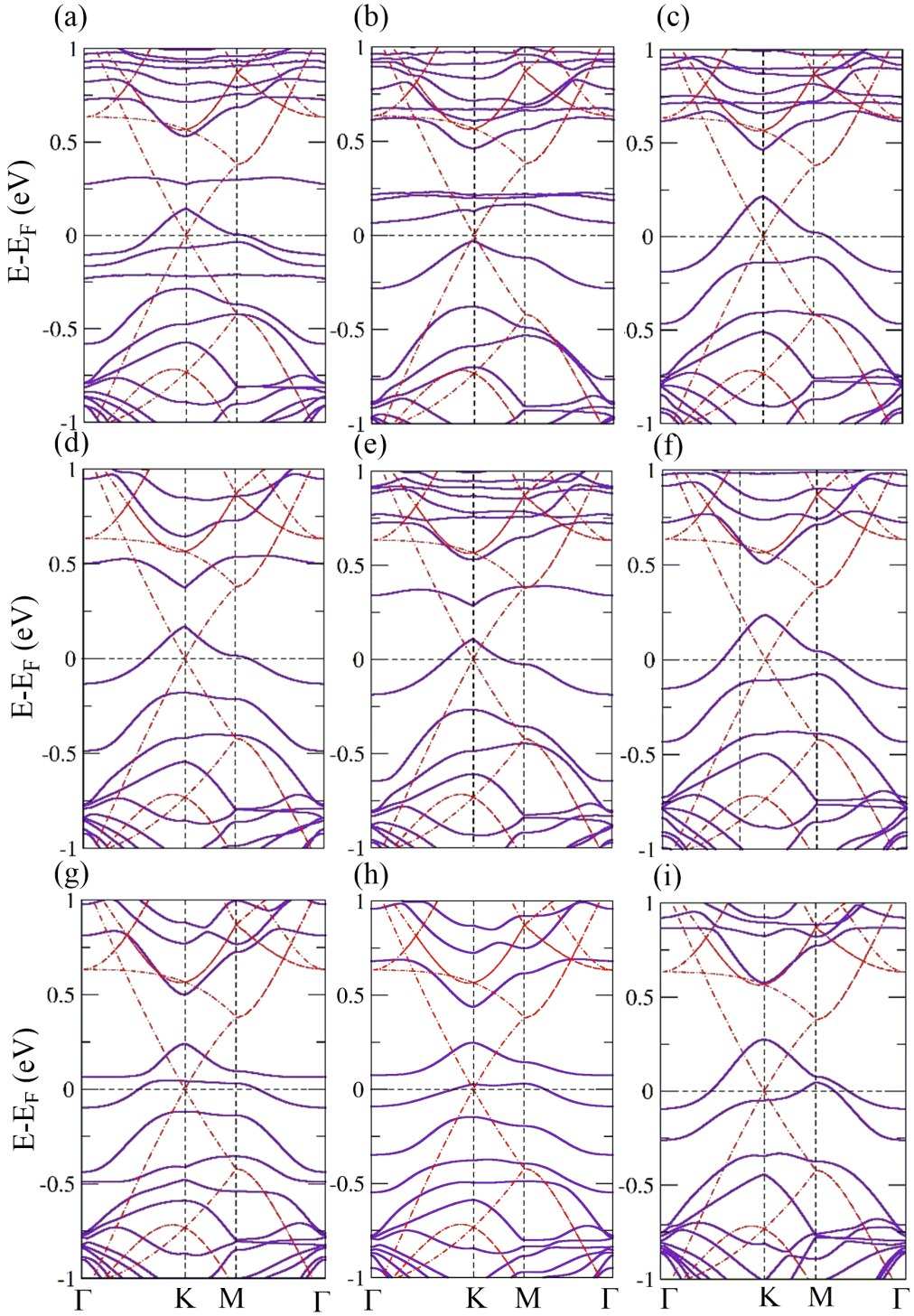

Figure 3.6 Electronic band structure of silicene with adsorbed (a) $[UO_2(OH)_2]$, (b) $[UO_2(NO_3)_2]$, (c) $[UO_2(CO_3)]$, (d) $[NpO_2(OH)_2]$, (e) $[NpO_2(NO_3)_2]$, (f) $[NpO_2(CO_3)]$, (g) $[PuO_2(OH)_2]$, (h) $[PuO_2(NO_3)_2]$ and (i) $[PuO_2(CO_3)]$. The red dashed lines stand for pristine silicene. The Fermi level is set to zero.

For germanene, the electronic band structure diagrams can be seen in Figure S9. Although the trends for band gap opening in germanene are similar to silicene, the effect is much smaller in the former case due to weak adsorption interactions. A maximum band gap of 0.218 eV was observed for [$PuO_2(CO_3)$] which is followed by [$PuO_2(OH)_2$] with a gap of 0.178 eV, and [$PuO_2(NO_3)_2$] (0.169 eV). For U and Np complexes as well, the carbonate complexes have a larger gap followed by hydroxide and then nitrate. The band gap values are 0.137 and 0.122 eV for [$NpO_2(CO_3)$] and [$UO_2(CO_3)$] respectively which is less than what was obtained for the silicene case. The smallest opening of only 0.042 eV was observed in [$UO_2(NO_3)_2$]. These results are in good agreement with the adsorption energy and charge transfer calculations. Indeed, there is an approximately linear relationship between the band gap and charge transfer values for both surfaces, see Figure S10. The small band gap opening in germanene as compared to silicene can be traced to the absence of strong chemisorption on the germanene surface.

Further detailed insight into the electronic structure of the adsorbent-adsorbate system is provided by the total and partial density of states (DOS) plots. Due to the presence of chemisorption interactions between silicene and Ac complexes, only the DOS for the silicene surface have been studied. As noted, the smallest bandgap among actinide-silicene systems has been observed for the nitrate complex of U, thus showing the presence of weak interactions. This is also evident from the DOS plot (see Figure 3.7-b). The contribution of the nitrate complex of uranium is further away from the Fermi energy as compared to the hydroxide and carbonate complexes. As we move from U to Pu, for each type of ligand the contribution of the complexes is moving closer to the Fermi level, indicating the presence of strong binding interactions. The PDOS plots are showing a detailed picture of the contribution from different orbitals (Figure S11). From the PDOS, Pu-complexes have more contribution from the 5f orbitals whereas Np and U have a stronger

contribution from 6d as compared to 5f. Our results may be further studied in detail for investigating the presence of energy degeneracy driven covalency. Specifically, in the Pu complexes we have the highest amount of charge transfer and thus, more ionic bonds (less covalent) as compared to U and Np which have more contribution from 6d orbitals than 5f orbitals.[80] The DOS of pristine silicene has been strongly altered by the adsorption of Ac-complexes which is indicative of the presence of strong interactions. Also, to note is the formation of new peaks in the total DOS because of the contributions from the actinide complexes in the DOS of pristine silicene. There is an increase in the strength of interaction due to stronger contributions from the complex near the Fermi level as we go down from U to Pu for each type of ligand. Hence, our DOS plots effectively support our overall results of the adsorption energy analysis (see above).

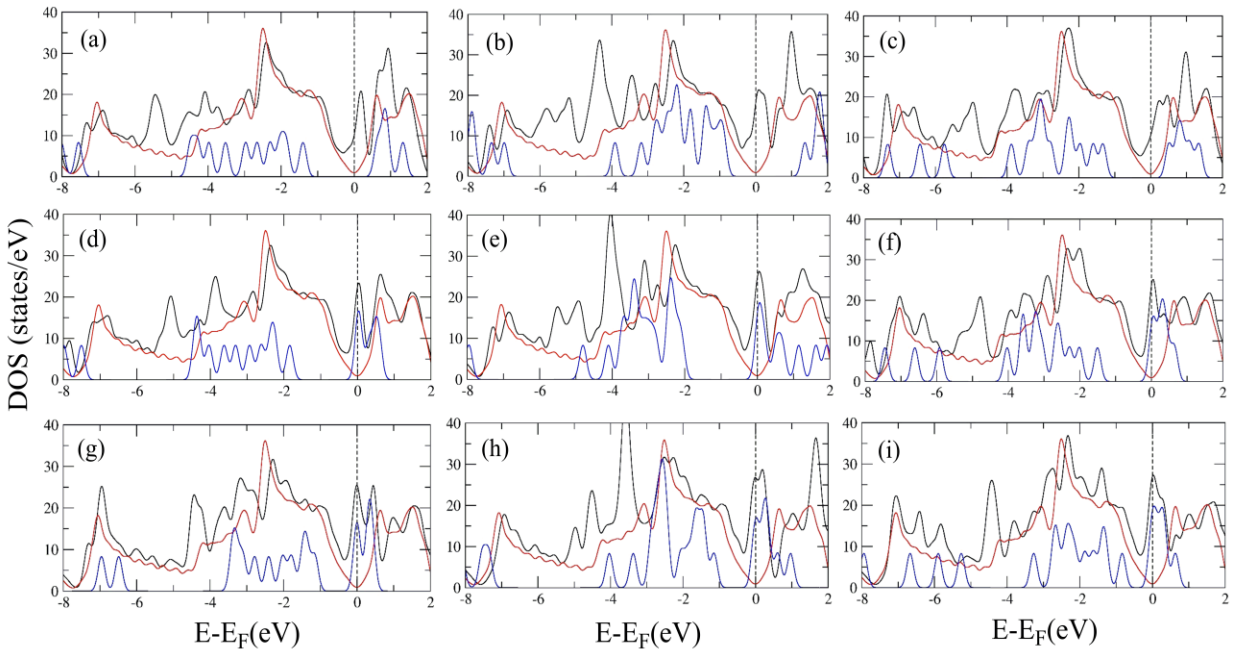

Figure 3.7 Density of states plots for (a) $[UO_2(OH)_2]$, (b) $[UO_2(NO_3)_2]$, (c) $[UO_2(CO_3)]$, (d) $[NpO_2(OH)_2]$, (e) $[NpO_2(NO_3)_2]$, (f) $[NpO_2(CO_3)]$, (g) $[PuO_2(OH)_2]$, (h) $[PuO_2(NO_3)_2]$ and (i) $[PuO_2(CO_3)]$ on silicene. Red line – pristine silicene, blue – adsorbed Ac-complex, and black – for total DOS (Ac-molecule+silicene). The Fermi level is set to zero.

3.5 Conclusions

In conclusion, first-principles calculations have been employed to investigate the structural and electronic properties of the adsorption of actinide (U-Pu) complexes with environmentally relevant ligands (equatorial OH^-, NO_3^-, and CO_3^{2-} ligands) on the silicene and germanene sheets. The inclusion of the cluster model with flake-size silicene provides detailed information for the presence of bonding between Si and the -yl oxo ligands which further leads to the reduction of the central metal from the +6 to the +4 oxidation. Moreover, the cluster model is highly beneficial for observing structural modifications in the 2D surface (such as bending, e.g. Figure S3) as PBC does not allow this by construction. Two different sizes of cluster were compared and only very minute differences in adsorption energies were observed. Because of the heavy charge transfer between complexes and silicene, the formed Si—O bonds have mainly ionic character. For the germanene cluster, very weak interactions between Ge and the –yl oxo ligand were observed. For silicene, the B-site is most favorable for carbonate complexes as well as for hydroxide complexes of Ac = U-Pu whereas the H-site is most suitable for strong interactions for nitrate complexes of Ac = U-Pu. The H-site is highly stable for all the complexes adsorbed on germanene cluster. In a periodic model, the Si atom which is on the plane of silicene, i.e. the OP-site, has been found to have the strongest binding with the silicene in the case of hydroxide and carbonate complexes. The nitrate complexes show the strongest affinity towards the sheet at the H-site again. The complexes adsorbed on germanene show stable interactions at different sites for different complexes in the periodic model. In both types of model, the carbonate complexes show strong interactions with silicene/germanene followed by hydroxide complexes and nitrate complexes of actinides, which is a result of a combination of steric factors and ligand properties. The binding of actinide complexes with silicene is comparable to that with borophene and stronger than with germanene.

The strong adsorption and opening of a large gap at the Dirac point that has been found are of great potential for the use of silicene as a sensor for radioactive materials, although selectivity may still cause an issue. Moreover, silicene could potentially be employed for separation of radioactive waste, extraction of uranium from seawater, and similar applications.

Bibliography

1. Geim, A. K. & Novoselov, K. S. The rise of graphene. *Nat. Mater.* **6**, 183–91 (2007).
2. Castro Neto, A. H., Guinea, F., Peres, N. M. R., Novoselov, K. S. & Geim, A. K. The electronic properties of graphene. *Rev. Mod. Phys.* **81**, 109–162 (2009).
3. Kemp, K. C. *et al.* Environmental applications using graphene composites: water remediation and gas adsorption. *Nanoscale* **5**, 3149 (2013).
4. Gupta, A., Sakthivel, T. & Seal, S. Recent development in 2D materials beyond graphene. *Prog. Mater. Sci.* **73**, 44–126 (2015).
5. Kaloni, T. P., Schreckenbach, G., Freund, M. S. & Schwingenschlögl, U. Current developments in silicene and germanene. *Phys. status solidi - Rapid Res. Lett.* **10**, 133–142 (2016).
6. Xu, M., Liang, T., Shi, M. & Chen, H. Graphene-Like Two-Dimensional Materials. *Chem. Rev.* **113**, 3766–3798 (2013).
7. Roome, N. J. & Carey, J. D. Beyond Graphene: Stable Elemental Monolayers of Silicene and Germanene. *ACS Appl. Mater. Interfaces* **6**, 7743–7750 (2014).
8. Acun, A. *et al.* Germanene: the germanium analogue of graphene. *J. Phys. Condens. Matter* **27**, 443002 (2015).
9. Lalmi, B. *et al.* Epitaxial growth of a silicene sheet. *Appl. Phys. Lett.* **97**, 223109 (2010).
10. Vogt, P. *et al.* Silicene: Compelling Experimental Evidence for Graphenelike Two-Dimensional Silicon. *Phys. Rev. Lett.* **108**, 155501 (2012).
11. Huang, X., Tian, R.-Y., Yang, X.-B. & Zhao, Y.-J. Competition between Pauli Exclusion and H-Bonding: H_2O and NH_3 on Silicene. *J. Phys. Chem. C* **120**, 19151–19159 (2016).
12. Kara, A. *et al.* A review on silicene — New candidate for electronics. *Surf. Sci. Rep.* **67**, 1–18 (2012).
13. Jose, D. & Datta, A. Structures and Chemical Properties of Silicene: Unlike Graphene. *Acc. Chem. Res.* **47**, 593–602 (2014).
14. Nijamudheen, A., Bhattacharjee, R., Choudhury, S. & Datta, A. Electronic and Chemical Properties of Germanene: The Crucial Role of Buckling. *J. Phys. Chem. C* **119**, 3802–3809 (2015).
15. Ye, M. *et al.* Tunable band gap in germanene by surface adsorption. *Phys. E Low-dimensional Syst. Nanostructures* **59**, 60–65 (2014).

16. Kaloni, T. P., Tahir, M. & Schwingenschlögl, U. Quasi free-standing silicene in a superlattice with hexagonal boron nitride. *Sci. Rep.* **3**, 3192 (2013).

17. Katsnelson, M. I. & Fasolino, A. Graphene as a Prototype Crystalline Membrane. *Acc. Chem. Res.* **46**, 97–105 (2013).

18. Cahangirov, S., Topsakal, M., Aktürk, E., Şahin, H. & Ciraci, S. Two- and One-Dimensional Honeycomb Structures of Silicon and Germanium. *Phys. Rev. Lett.* **102**, 236804 (2009).

19. Liu, C.-C., Jiang, H. & Yao, Y. Low-energy effective Hamiltonian involving spin-orbit coupling in silicene and two-dimensional germanium and tin. *Phys. Rev. B* **84**, 195430 (2011).

20. Schedin, F. *et al.* Detection of individual gas molecules adsorbed on graphene. *Nat. Mater.* **6**, 652–655 (2007).

21. He, Q., Wu, S., Yin, Z. & Zhang, H. Graphene-based electronic sensors. *Chem. Sci.* **3**, 1764 (2012).

22. Kaloni, T. P., Schreckenbach, G. & Freund, M. S. Large Enhancement and Tunable Band Gap in Silicene by Small Organic Molecule Adsorption. *J. Phys. Chem. C* **118**, 23361–23367 (2014).

23. Pang, Q. *et al.* Adsorption of alkali metal atoms on germanene: A first-principles study. *Appl. Surf. Sci.* **314**, 15–20 (2014).

24. Kaloni, T. P. Tuning the Structural, Electronic, and Magnetic Properties of Germanene by the Adsorption of 3d Transition Metal Atoms. *J. Phys. Chem. C* **118**, 25200–25208 (2014).

25. Sahin, H. & Peeters, F. M. Adsorption of alkali, alkaline-earth, and 3 d transition metal atoms on silicene. *Phys. Rev. B* **87**, 085423 (2013).

26. Lin, X. & Ni, J. Much stronger binding of metal adatoms to silicene than to graphene: A first-principles study. *Phys. Rev. B* **86**, 075440 (2012).

27. Hu, W., Xia, N., Wu, X., Li, Z. & Yang, J. Silicene as a highly sensitive molecule sensor for NH3, NO and NO2. *Phys. Chem. Chem. Phys.* **16**, 6957 (2014).

28. Xia, W., Hu, W., Li, Z. & Yang, J. A first-principles study of gas adsorption on germanene. *Phys. Chem. Chem. Phys.* **16**, 22495–22498 (2014).

29. Bui, V. Q., Pham, T.-T., Nguyen, H.-V. S. & Le, H. M. Transition Metal (Fe and Cr) Adsorptions on Buckled and Planar Silicene Monolayers: A Density Functional Theory Investigation. *J. Phys. Chem. C* **117**, 23364–23371 (2013).

30. Le, H. M., Pham, T.-T., Dinh, T. S., Kawazoe, Y. & Nguyen-Manh, D. First-principles modeling of 3 *d* -transition-metal-atom adsorption on silicene: a linear-response DFT + *U* approach. *J. Phys. Condens. Matter* **28**, 135301 (2016).

31. Valencia, H., Gil, A. & Frapper, G. Trends in the Adsorption of 3d Transition Metal Atoms onto Graphene and Nanotube Surfaces: A DFT Study and Molecular Orbital Analysis. *J. Phys. Chem. C* **114**, 14141–14153 (2010).

32. Manadé, M., Viñes, F. & Illas, F. Transition metal adatoms on graphene: A systematic density functional study. *Carbon N. Y.* **95**, 525–534 (2015).

33. Nelson, D. M. & Lovett, M. B. Oxidation state of plutonium in the Irish Sea. *Nature* **276**, 599–601 (1978).

34. Rubio Montero, P. & Martín Sánchez, A. Plutonium contamination from accidental release or

simply fallout: study of soils at Palomares (Spain). *J. Environ. Radioact.* **55**, 157–165 (2001).

35. Li, Z. *et al.* Uranium(VI) adsorption on graphene oxide nanosheets from aqueous solutions. *Chem. Eng. J.* **210**, 539–546 (2012).

36. Deb, A. K. S., Ilaiyaraja, P., Ponraju, D. & Venkatraman, B. Diglycolamide functionalized multi-walled carbon nanotubes for removal of uranium from aqueous solution by adsorption. *J. Radioanal. Nucl. Chem.* **291**, 877–883 (2012).

37. Iijima, S. Helical microtubules of graphitic carbon. *Nature* **354**, 56–58 (1991).

38. Han, J., Dai, X., Gao, Y., Meng, Y. & Wang, Z. Defect-induced strong localization of uranium dicarbide on the graphene surface. *Phys. Chem. Chem. Phys.* **16**, 22784–22790 (2014).

39. Han, J. *et al.* Strong Adsorption Between Uranium Dicarbide and Graphene Surface Induced by f Electrons. *J. Phys. Chem. C* **117**, 26849–26857 (2013).

40. Wu, Q.-Y. *et al.* Understanding the Interactions of Neptunium and Plutonium Ions with Graphene Oxide: Scalar-Relativistic DFT Investigations. *J. Phys. Chem. A* **118**, 10273–10280 (2014).

41. Du, J. & Jiang, G. Adsorption of 5f-electron atoms (ThCm) on graphene surface: An all-electron ZORA-DFT study. *J. Colloid Interface Sci.* **508**, 159–166 (2017).

42. Luo, W. *et al.* Sequestering Uranium and Technetium through Co-Precipitation with Aluminum in a Contaminated Acidic Environment. *Environ. Sci. Technol.* **43**, 7516–7522 (2009).

43. Nalan Kabay, ‡ *et al.* Recovery of Uranium from Phosphoric Acid Solutions Using Chelating Ion-Exchange Resins†. (1998).

44. Yue, Y. *et al.* Seawater Uranium Sorbents: Preparation from a Mesoporous Copolymer Initiator by Atom-Transfer Radical Polymerization. *Angew. Chemie Int. Ed.* **52**, 13458–13462 (2013).

45. Wang, D. *et al.* Significantly Enhanced Uranium Extraction from Seawater with Mass Produced Fully Amidoximated Nanofiber Adsorbent. *Adv. Energy Mater.* **8**, 1802607 (2018).

46. Abney, C. W., Mayes, R. T., Saito, T. & Dai, S. Materials for the Recovery of Uranium from Seawater. *Chem. Rev.* **117**, 13935–14013 (2017).

47. Sholl, D. S. & Lively, R. P. Seven chemical separations to change the world. *Nature* **532**, 435–437 (2016).

48. te Velde, G. *et al.* Chemistry with ADF. *J. Comput. Chem.* **22**, 931–967 (2001).

49. Giannozzi, P. *et al.* QUANTUM ESPRESSO: a modular and open-source software project for quantum simulations of materials. *J. Phys. Condens. Matter* **21**, 395502 (2009).

50. Perdew, J. P., Burke, K. & Ernzerhof, M. Generalized Gradient Approximation Made Simple. *Phys. Rev. Lett.* **77**, 3865–3868 (1996).

51. Grimme, S., Antony, J., Ehrlich, S. & Krieg, H. A consistent and accurate *ab initio* parametrization of density functional dispersion correction (DFT-D) for the 94 elements H-Pu. *J. Chem. Phys.* **132**, 154104 (2010).

52. Grimme, S., Ehrlich, S. & Goerigk, L. Effect of the damping function in dispersion corrected density functional theory. *J. Comput. Chem.* **32**, 1456–1465 (2011).

53. Becke, A. D. & Johnson, E. R. A density-functional model of the dispersion interaction. *J. Chem. Phys.* **123**, 154101 (2005).

54. Lenthe, E. van, Baerends, E. J. & Snijders, J. G. Relativistic regular two- component Hamiltonians. *J. Chem. Phys.* **99**, 4597–4610 (1993).

55. van Lenthe, E., Ehlers, A. & Baerends, E.-J. Geometry optimizations in the zero order regular approximation for relativistic effects. *J. Chem. Phys.* **110**, 8943–8953 (1999).

56. Van Lenthe, E. & Baerends, E. J. Optimized Slater-type basis sets for the elements 1-118. *J. Comput. Chem.* **24**, 1142–1156 (2003).

57. Hirshfeld, F. L. Bonded-atom fragments for describing molecular charge densities. *Theor. Chim. Acta* **44**, 129–138 (1977).

58. Bader, R. F. W. *Atoms in Molecules - A Quantum Theory*. (Oxford University Press, 1990).

59. Bader, R. F. W., Bayles, D. & Heard, G. L. Properties of atoms in molecules: Transition probabilities. *J. Chem. Phys.* **112**, 10095–10105 (2000).

60. Bridgeman, A. J., Cavigliasso, G., Ireland, L. R. & Rothery, J. The Mayer bond order as a tool in inorganic chemistry†. *J. Chem. Soc. Dalt. Trans.* 2095–2108 (2001).

61. Pye, C. C. & Ziegler, T. An implementation of the conductor-like screening model of solvation within the Amsterdam density functional package. *Theor. Chem. Accounts Theory, Comput. Model. (Theoretica Chim. Acta)* **101**, 396–408 (1999).

62. Klamt, A. Conductor-like Screening Model for Real Solvents: A New Approach to the Quantitative Calculation of Solvation Phenomena. *J. Phys. Chem.* **99**, 2224–2235 (1995).

63. Klamt, A. & Schüürmann, G. COSMO: a new approach to dielectric screening in solvents with explicit expressions for the screening energy and its gradient. *J. Chem. Soc., Perkin Trans. 2* 799–805 (1993).

64. Singhal, P., Jha, S. K., Pandey, S. P. & Neogy, S. Rapid extraction of uranium from sea water using Fe3O4 and humic acid coated Fe3O4 nanoparticles. *J. Hazard. Mater.* **335**, 152–161 (2017).

65. Blöchl, P. E. Projector augmented-wave method. *Phys. Rev. B* **50**, 17953–17979 (1994).

66. Reed, A. E., Weinstock, R. B. & Weinhold, F. Natural population analysis. *J. Chem. Phys.* **83**, 735–746 (1985).

67. Lazar, P. *et al.* Adsorption of Small Organic Molecules on Graphene. *J. Am. Chem. Soc.* **135**, 6372–6377 (2013).

68. Ha, M. *et al.* Adsorption of Carbon Tetrahalides on Coronene and Graphene. *J. Phys. Chem. C* **121**, 14968–14974 (2017).

69. Makov, G. & Payne, M. C. Periodic boundary conditions in *ab initio* calculations. *Phys. Rev. B* **51**, 4014–4022 (1995).

70. Schreckenbach, G., Hay, P. J. & Martin, R. L. Density functional calculations on actinide compounds: Survey of recent progress and application to [UO2X4]2? (X=F, Cl, OH) and AnF6 (An=U, Np, Pu). *J. Comput. Chem.* **20**, 70–90 (1999).

71. Bühl, M. & Schreckenbach, G. Oxygen Exchange in Uranyl Hydroxide via Two "Nonclassical" Ions. *Inorg. Chem.* **49**, 3821–3827 (2010).

72. Shamov, G. A. & Schreckenbach, G. Theoretical Study of the Oxygen Exchange in Uranyl Hydroxide. An Old Riddle Solved? *J. Am. Chem. Soc.* **130**, 13735–13744 (2008).

73. Shamov, G. A. & Schreckenbach, G. Density Functional Studies of Actinyl Aquo Complexes Studied Using Small-Core Effective Core Potentials and a Scalar Four-Component Relativistic Method. *J. Phys. Chem. A* **109**, 10961–10974 (2005).

74. Grover, P. & Schreckenbach, G. A first-principles study of adsorption of actinide complexes on borophene. *Submitted* (2019).

75. Sun, Y. *et al.* Adsorption and Desorption of U(VI) on Functionalized Graphene Oxides: A Combined Experimental and Theoretical Study. *Environ. Sci. Technol.* **49**, 4255–4262 (2015).

76. Kaloni, T. P. & Schwingenschlögl, U. Weak interaction between germanene and GaAs(0001) by H intercalation: A route to exfoliation. *J. Appl. Phys.* **114**, 184307 (2013).

77. Schreckenbach, G. Differential Solvation. *Chem. - A Eur. J.* **23**, 3797–3803 (2017).

78. Feng, J. *et al.* Gas adsorption on silicene: A theoretical study. *Comput. Mater. Sci.* **87**, 218–226 (2014).

79. Quhe, R. *et al.* Tunable and sizable band gap in silicene by surface adsorption. *Sci. Rep.* **2**, 853 (2012).

80. Su, J. *et al.* Energy-Degeneracy-Driven Covalency in Actinide Bonding. *J. Am. Chem. Soc.* **140**, 17977–17984 (2018).

Chapter 3 Appendix

System	d (Å)	Θ (deg)	Si—Si (Å)	Δ (Å)
Silicene	--	115	2.27	0.47
$UO_2(OH)_2$	3.29	100-115	2.25-2.36	0.40-0.62
$NpO_2(OH)_2$	3.50	104-117	2.27-2.36	0.43-0.65
$PuO_2(OH)_2$	3.58	104-117	2.26-2.36	0.42-0.63
$UO_2(NO_3)_2$	3.32	101-116	2.26-2.35	0.38-0.68
$NpO_2(NO_3)_2$	3.58	97-115	2.27-2.35	0.42-0.70
$PuO_2(NO_3)_2$	3.62	99-117	2.26-2.36	0.41-0.67
$UO_2(CO_3)$	3.24	100-116	2.25-2.38	0.45-0.69
$NpO_2(CO_3)$	3.42	103-116	2.27-2.37	0.42-0.68
$PuO_2(CO_3)$	3.50	100-117	2.26-2.37	0.39-0.66

Table S1 Geometrical parameters of pristine silicene $Si_{64}H_{20}$ and strongest adsorbed site for each complex adsorbed on the flake in a water solvent.

System	Ac—O (Å)		Ac—O (Å)		Si—O (Å)	MBO (Si—O)
	Before	After	Before	After		
$UO_2(OH)_2$	1.81	2.09	1.87	0.45	1.70	0.43
$NpO_2(OH)_2$	1.80	2.15	1.89	0.40	1.67	0.50
$PuO_2(OH)_2$	1.79	2.18	1.92	0.38	1.65	0.51
$UO_2(NO_3)_2$	1.79	2.07	1.93	0.48	1.70	0.39
$NpO_2(NO_3)_2$	1.78	2.15	1.95	0.40	1.67	0.45
$PuO_2(NO_3)_2$	1.78	2.16	2.00	0.38	1.66	0.51
$UO_2(CO_3)$	1.77	2.09	1.96	0.45	1.69	0.43
$NpO_2(CO_3)$	1.79	2.13	1.97	0.43	1.67	0.48
$PuO_2(CO_3)$	1.77	2.17	1.99	0.38	1.66	0.52

Table S2 Bond lengths of Ac-complexes before and after adsorption and bond lengths of newly formed Si—O bonds with Mayer bond order values (MBO) for adsorption on the $Si_{64}H_{20}$ flake in a water solvent.

System	H-site	B-site	OP-site	AP-site	Q
$UO_2(OH)_2$	-0.920	-0.897	-0.963	-0.010	0.372
$NpO_2(OH)_2$	-1.246	-1.324	-1.217	-0.171	0.462
$PuO_2(OH)_2$	-1.826	-1.769	-1.827	-0.580	0.503
$UO_2(NO_3)_2$	-0.896	-0.850	-0.825	0.092	0.365
$NpO_2(NO_3)_2$	-1.221	-1.147	-1.118	-0.115	0.415
$PuO_2(NO_3)_2$	-1.773	-1.719	-1.684	-0.458	0.587
$UO_2(CO_3)$	-1.229	-1.310	-1.201	-0.279	0.447
$NpO_2(CO_3)$	-1.698	-1.743	-1.649	-0.508	0.561
$PuO_2(CO_3)$	-2.089	-2.140	-2.018	-0.761	0.794

Table S3 Adsorption energy (in eV) at all four anchoring positions in terms of the central metal in the optimized structure and amount of charge transfer from the $Si_{64}H_{20}$ flake to Ac-complex for the most strongly adsorbed site.

System	d (Å)	Θ (deg)	Si—Si (Å)	Δ (Å)
Silicene	--	115	2.27	0.48
$UO_2(OH)_2$	3.17	97-115	2.25-2.36	0.47-0.64
$NpO_2(OH)_2$	3.19	115-116	2.25-2.35	0.35-0.73
$PuO_2(OH)_2$	3.44	105-116	2.25-2.36	0.43-0.70
$UO_2(NO_3)_2$	3.32	103-117	2.26-2.35	0.39-0.71
$NpO_2(NO_3)_2$	3.27	104-116	2.26-2.34	0.36-0.67
$PuO_2(NO_3)_2$	3.53	105-115	2.26-2.35	0.38-0.65
$UO_2(CO_3)$	3.01	100-116	2.26-2.37	0.42-0.67
$NpO_2(CO_3)$	3.08	98-116	2.25-2.37	0.39-0.65
$PuO_2(CO_3)$	3.15	98-116	2.25-2.38	0.40-0.69

Table S4 Structural parameters of pristine silicene $Si_{42}H_{16}$ and strongly adsorbed site for each complex adsorbed on the flake in gas phase.

System	Ac—O (Å)		MBO		Si—O (Å)	MBO (Si—O (Å))
	Before	After	Before	After		
$UO_2(OH)_2$	1.81	2.09	1.90	0.49	1.68	0.47
$NpO_2(OH)_2$	1.78	2.13	1.92	0.43	1.66	0.49
$PuO_2(OH)_2$	1.77	2.16	2.02	0.39	1.64	0.54
$UO_2(NO_3)_2$	1.79	2.05	1.91	0.54	1.72	0.40
$NpO_2(NO_3)_2$	1.78	2.11	1.92	0.46	1.67	0.46
$PuO_2(NO_3)_2$	1.76	2.13	2.04	0.41	1.65	0.52
$UO_2(CO_3)$	1.79	2.08	1.90	0.49	1.69	0.43
$NpO_2(CO_3)$	1.79	2.10	1.90	0.47	1.67	0.47
$PuO_2(CO_3)$	1.77	2.15	2.01	0.40	1.64	0.53

Table S5 Bond lengths of Ac-complexes before and after adsorption and bond lengths of newly formed Si—O bonds with Mayer bond order values (MBO) for adsorption on $Si_{42}H_{16}$ flake in gas phase.

System	H-site	B-site	OP-site	AP-site	Q
$UO_2(OH)_2$	-1.240	-1.291	-1.204	-0.267	0.362
$NpO_2(OH)_2$	-1.515	-1.487	-1.572	-0.535	0.393
$PuO_2(OH)_2$	-2.021	-2.004	-2.098	-0.967	0.581
$UO_2(NO_3)_2$	-0.925	-0.893	-0.997	-0.028	0.348
$NpO_2(NO_3)_2$	-1.328	-1.300	-1.379	-0.395	0.367
$PuO_2(NO_3)_2$	-2.036	-1.964	-1.993	-0.903	0.544
$UO_2(CO_3)$	-1.529	-1.591	-1.495	-0.425	0.396
$NpO_2(CO_3)$	-1.916	-1.957	-1.866	-0.827	0.493
$PuO_2(CO_3)$	-2.416	-2.489	-2.394	-1.014	0.789

Table S6 Adsorption energy (in eV) at all four anchoring positions in gas phase and amount of charge transfer from the $Si_{42}H_{16}$ flake to Ac-complex for the most strongly adsorbed site.

System	d (Å)	Θ (deg)	Ge—Ge(Å)	Δ (Å)
$Ge_{42}H_{16}$	--	112	2.43	0.68
$UO_2(OH)_2$	3.38	97-120	2.42-2.50	0.62-1.13
$NpO_2(OH)_2$	3.18	97-120	2.43-2.51	0.65-0.95
$PuO_2(OH)_2$	3.13	94-114	2.43-2.53	0.70-0.98
$UO_2(NO_3)_2$	3.70	102-118	2.42-2.44	0.65-0.90
$NpO_2(NO_3)_2$	3.41	96-117	2.42-2.51	0.62-0.87
$PuO_2(NO_3)_2$	3.38	97-116	2.42-2.51	0.61-1.07
$UO_2(CO_3)$	3.32	96-119	2.40-2.51	0.73-0.96
$NpO_2(CO_3)$	3.14	95-117	2.41-2.52	0.61-0.94
$PuO_2(CO_3)$	3.11	98-119	2.45-2.48	0.59-1.19

Table S7 Structural parameters of germanene flake before and after adsorption of Ac-complexes in gas phase where d (Å) is the distance between the central metal atom and $Ge_{42}H_{16}$, Θ (deg) is the hexagonal angle between three neighboring Ge atoms, Ge—Ge bond length in Å, and Δ (Å) is the buckling parameter.

System	Ac—O (Å)		MBO		Ge—O (Å)	MBO (Ge—O)
	Before	After	Before	After		
$UO_2(OH)_2$	1.81	1.89	1.90	1.47	2.10	0.20
$NpO_2(OH)_2$	1.78	1.91	1.92	0.73	2.05	0.25
$PuO_2(OH)_2$	1.77	1.93	2.02	0.71	1.97	0.30
$UO_2(NO_3)_2$	1.79	1.80	1.91	1.98	--	--
$NpO_2(NO_3)_2$	1.78	1.89	1.92	0.78	2.04	0.23
$PuO_2(NO_3)_2$	1.76	1.92	2.04	0.75	2.03	0.25
$UO_2(CO_3)$	1.79	1.92	1.90	1.39	2.07	0.21
$NpO_2(CO_3)$	1.79	1.93	1.90	0.74	2.05	0.26
$PuO_2(CO_3)$	1.77	1.97	2.01	0.69	1.98	0.32

Table S8 Mayer bond order analysis of Ac—O bond before and after adsorption on $Ge_{42}H_{16}$ in gas phase along with bond order and bond length values of newly formed Ge—O bonds.

Sytem	H-site	B-site	OP-site	AP-site	Q
$UO_2(OH)_2$	-0.628	-0.516	-0.561	-0.486	0.367
$NpO_2(OH)_2$	-0.818	-0.720	-0.757	-0.702	0.526
$PuO_2(OH)_2$	-1.333	-1.204	-1.238	-1.179	0.885
$UO_2(NO_3)_2$	-0.520	-0.406	-0.448	-0.396	0.255
$NpO_2(NO_3)_2$	-0.573	-0.474	-0.513	-0.449	0.332
$PuO_2(NO_3)_2$	-0.911	-0.827	-0.859	-0.789	0.664
$UO_2(CO_3)$	-0.702	-0.612	-0.639	-0.600	0.466
$NpO_2(CO_3)$	-0.961	-0.869	-0.916	-0.841	0.697
$PuO_2(CO_3)$	-1.665	-1.551	-1.608	-1.539	0.906

Table S9 Adsorption energy (in eV) at all four anchoring positions in gas phase and amount of charge transfer from the $Ge_{42}H_{16}$ flake to Ac-complex for the most strongly adsorbed site.

Ac-Complex – $Ge_{42}H_{16}$	Ac—O (Å)		MBO (Ac—O)		Ge—O (Å)	MBO(Ge—O)
	Before	After	Before	After		
$UO_2(OH)_2$	1.81	1.88	1.838	1.60	2.22	0.13
$NpO_2(OH)_2$	1.80	1.92	1.879	0.73	2.02	0.23
$PuO_2(OH)_2$	1.79	1.94	1.953	0.67	2.00	0.31
$UO_2(NO_3)_2$	1.78	1.80	1.953	1.99	--	--
$NpO_2(NO_3)_2$	1.78	1.90	1.967	0.75	2.04	0.21
$PuO_2(NO_3)_2$	1.77	1.92	2.010	0.78	2.02	0.26
$UO_2(CO_3)$	1.79	1.90	1.940	1.49	2.13	0.19
$NpO_2(CO_3)$	1.77	1.93	1.971	0.72	2.01	0.25
$PuO_2(CO_3)$	1.77	1.94	1.985	0.68	1.99	0.32

Table S10 Mayer bond order analysis of Ac—O and Ge—O bond before and after adsorption on $Ge_{42}H_{16}$ in water solvent.

System	Ac—O (Å) (Before adsorption)	Ac—O (Å) (After adsorption)	Si—O (Å)
$UO_2(OH)_2$	1.80	2.01	1.73
$NpO_2(OH)_2$	1.78	2.02	1.71
$PuO_2(OH)_2$	1.76	2.09	1.66
$UO_2(NO_3)_2$	1.78	1.97	1.79
$NpO_2(NO_3)_2$	1.77	1.98	1.76
$PuO_2(NO_3)_2$	1.74	2.07	1.68
$UO_2(CO_3)$	1.80	1.99	1.75
$NpO_2(CO_3)$	1.78	2.00	1.73
$PuO_2(CO_3)$	1.73	2.08	1.67

Table S11 Bond lengths of Ac-complexes before and after adsorption with the bond length of the newly formed Si—O bonds for the adsorption on silicene under periodic boundary conditions.

System	d (Å)	Θ (deg)	Ge—Ge (Å)	Δ (Å)	E_{ad} (eV)	Q (e)	E_{gap} (eV)
Germanene	--	112	2.44	0.68	--	--	--
$UO_2(OH)_2$	3.40	105-113	2.44-2.51	0.62-0.79	-0.422	1.126	0.067
$NpO_2(OH)_2$	3.31	103-114	2.43-2.50	0.64-0.80	-0.585	1.255	0.073
$PuO_2(OH)_2$	3.19	109-114	2.44-2.54	0.61-0.82	-1.143	1.525	0.178
$UO_2(NO_3)_2$	3.67	110-114	2.44-2.46	0.67-0.81	-0.259	0.735	0.042
$NpO_2(NO_3)_2$	3.53	111-114	2.44-2.45	0.65-0.72	-0.381	1.100	0.050
$PuO_2(NO_3)_2$	3.35	110-114	2.44-2.51	0.66-0.81	-0.558	1.175	0.169
$UO_2(CO_3)$	3.36	100-114	2.43-2.51	0.71-0.88	-0.507	1.146	0.122
$NpO_2(CO_3)$	3.27	109-114	2.44-2.50	0.63-0.81	-0.680	1.368	0.137
$PuO_2(CO_3)$	3.17	109-114	2.44-2.54	0.63-0.79	-1.456	1.618	0.218

Table S12 Geometrical parameters, adsorption energy, band gap and amount of charge transfer from 2D sheet to complex for pristine germanene and adsorbed Ac-complexes under PBC.

Ac-Complex - germanene	Ac—O (Å)		Ge—O (Å)
	Before	After	
$UO_2(OH)_2$	1.80	1.84	2.12
$NpO_2(OH)_2$	1.78	1.85	2.17
$PuO_2(OH)_2$	1.76	1.90	2.02
$UO_2(NO_3)_2$	1.78	1.79	--
$NpO_2(NO_3)_2$	1.77	1.77	--
$PuO_2(NO_3)_2$	1.74	1.87	2.14
$UO_2(CO_3)$	1.80	1.88	2.11
$NpO_2(CO_3)$	1.78	1.86	2.13
$PuO_2(CO_3)$	1.73	1.92	1.96

Table S13 Bond length comparison of Ac—O bonds before and after adsorption along with Ge—O bond distances for adsorption on germanene under PBC.

Silicene − Ac- complex	H-site	B-site	OP-site	AP-site
$UO_2(OH)_2$	-0.930	-0.998	-0.902	-0.001
$NpO_2(OH)_2$	-1.271	-1.331	-1.223	-0.141
$PuO_2(OH)_2$	-1.843	-1.920	-1.818	-0.523
$UO_2(NO_3)_2$	-0.914	-0.857	-0.815	0.089
$NpO_2(NO_3)_2$	-1.237	-1.174	-1.132	-0.103
$PuO_2(NO_3)_2$	-1.787	-1.734	-1.700	-0.412
$UO_2(CO_3)$	-1.347	-1.398	-1.311	-0.256
$NpO_2(CO_3)$	-1.709	-1.763	-1.656	-0.408
$PuO_2(CO_3)$	-2.131	-2.211	-2.101	-0.646

Table S14 Calculated adsorption energies (in eV) at all four anchoring positions (see Figure 3.1) named according to central metal position in the optimized structure for the cluster model of silicene cluster under water solvent conditions.

Ac-Complex − $Si_{42}H_{16}$	Ac—O (Å)	On B site		On OP site		On AP site	
	Before	Ac—O	Si—O	Ac—O	Si—O	Ac—O	Si—O
$UO_2(OH)_2$	1.817	2.01	1.99	2.01	2.00	1.83	--
$NpO_2(OH)_2$	1.803	2.04	1.95	2.02	1.97	1.81	--
$PuO_2(OH)_2$	1.781	2.05	1.94	2.04	1.96	1.80	--
$UO_2(CO_3)$	1.795	2.00	1.98	2.00	1.99	1.81	--
$NpO_2(CO_3)$	1.774	2.02	1.94	2.01	1.96	1.78	--
$PuO_2(CO_3)$	1.771	2.04	1.93	2.03	1.93	1.78	--
Ac-Complex − $Si_{42}H_{16}$	Ac—O (Å)	On H site		On OP site		On AP site	
	Before	Ac—O	Si—O	Ac—O	Si—O	Ac—O	Si—O
$UO_2(NO_3)_2$	1.789	1.96	1.99	1.94	2.02	1.79	--
$NpO_2(NO_3)_2$	1.780	1.98	1.97	1.96	1.97	1.78	--
$PuO_2(NO_3)_2$	1.766	2.02	1.94	2.01	1.94	1.77	--

Table S15 Ac-O bond lengths before and after adsorption along with the bond lengths of newly formed Si—O bonds on less favourable sites for the adsorption on $Si_{42}H_{16}$ flake under solvent conditions.

Ac-complex – Silicene	Rho, ρ (Si—O)	Laplacian, $\nabla^2\rho$ (Si—O)
$UO_2(CO_3)$	0.124	0.598
$NpO_2(CO_3)$	0.132	0.664
$PuO_2(CO_3)$	0.138	0.723

Table S16 QTAIM analysis of electron densities at the bond critical point (BCP) of Si—O bonds where ρ is the magnitude of the electron density and $\nabla^2\rho$ is the Laplacian of ρ for carbonate complexes of actinides adsorbed on $Si_{42}H_{16}$ flake under solvent conditions.

Ac-complex – Silicene	Spin Density (Ac atom) in electron
$UO_2(OH)_2$	1.591
$NpO_2(OH)_2$	3.298
$PuO_2(OH)_2$	4.714
$UO_2(NO_3)_2$	1.278
$NpO_2(NO_3)_2$	3.131
$PuO_2(NO_3)_2$	4.537
$UO_2(CO_3)$	1.843
$NpO_2(CO_3)$	3.478
$PuO_2(CO_3)$	4.849

Table S17 Spin density values on the Ac atom after adsorption on $Si_{42}H_{16}$ flake in water solvent.

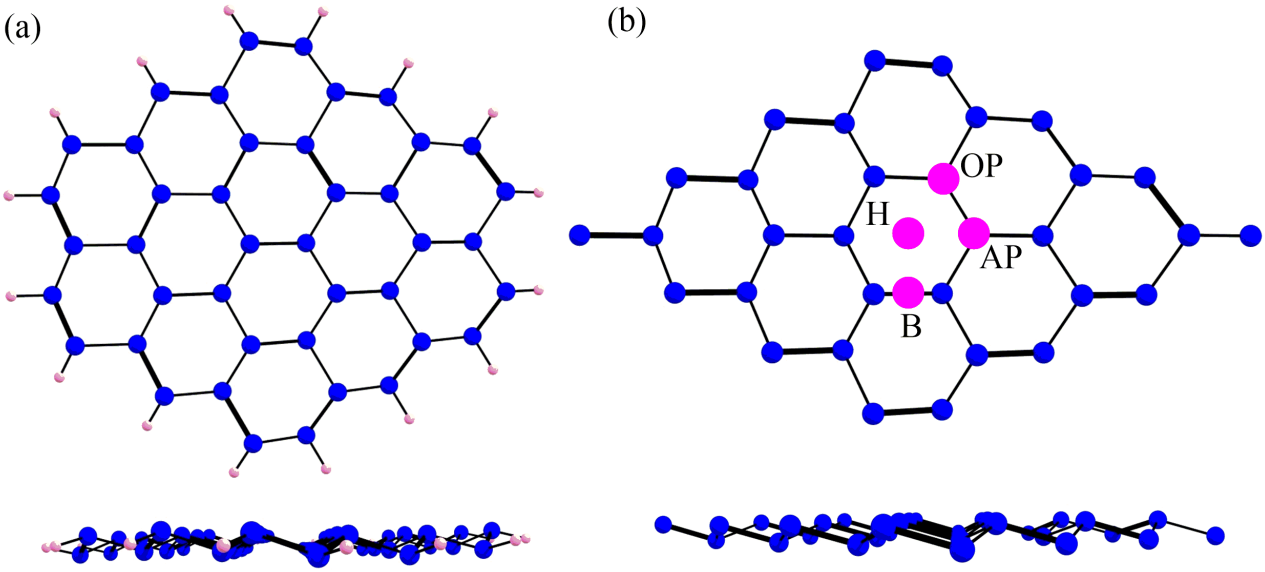

Figure S1 Top and side views of optimized structures of (a) $Ge_{42}H_{16}$ flake and (b) germanene supercell under periodic conditions.

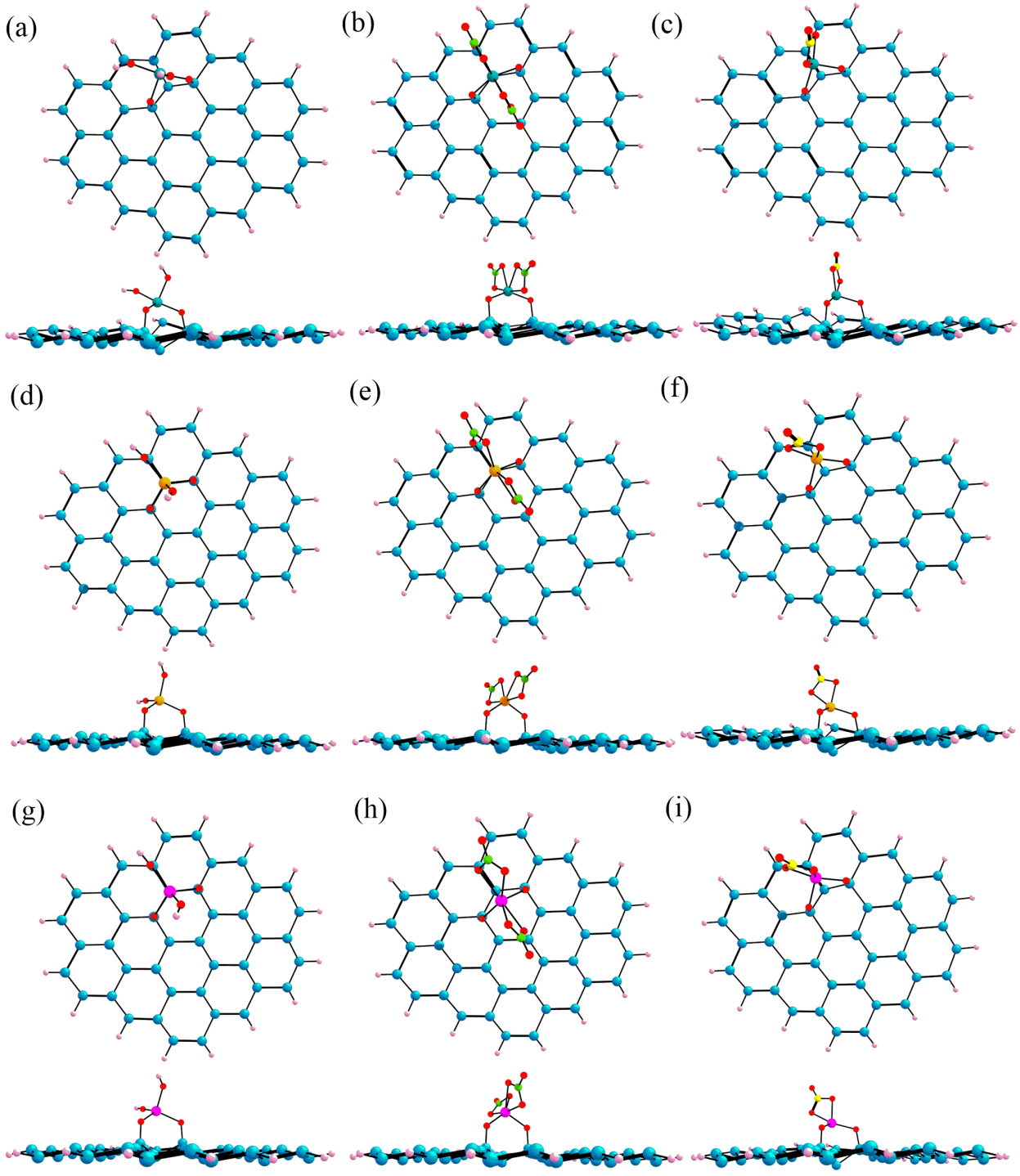

Figure S2 Top and side views of the optimized structures in gas phase for (a) $[UO_2(OH)_2]$, (b) $[UO_2(NO_3)_2]$, (c) $[UO_2(CO_3)]$, (d) $[NpO_2(OH)_2]$, (e) $[NpO_2(NO_3)_2]$, (f) $[NpO_2(CO_3)]$, (g) $[PuO_2(OH)_2]$, (h) $[PuO_2(NO_3)_2]$ and (i) $[PuO_2(CO_3)]$ on $Si_{42}H_{16}$ flake.

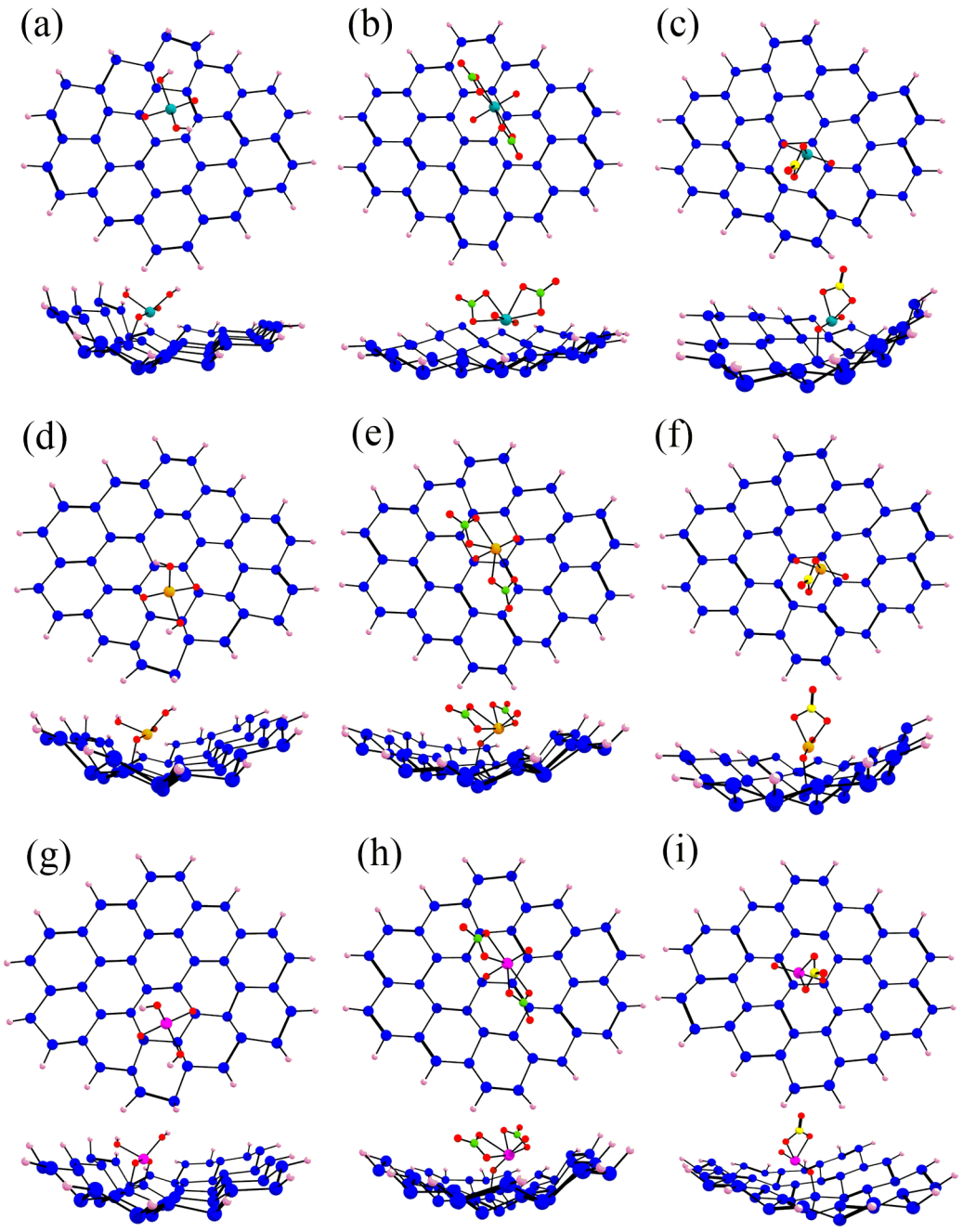

Figure S3 Optimized geometries of (a) $[UO_2(OH)_2]$, (b) $[UO_2(NO_3)_2]$, (c) $[UO_2(CO_3)]$, (d) $[NpO_2(OH)_2]$, (e) $[NpO_2(NO_3)_2]$, (f) $[NpO_2(CO_3)]$, (g) $[PuO_2(OH)_2]$, (h) $[PuO_2(NO_3)_2]$, and (i) $[PuO_2(CO_3)]$ complexes adsorbed on $Ge_{42}H_{16}$ in water solvent.

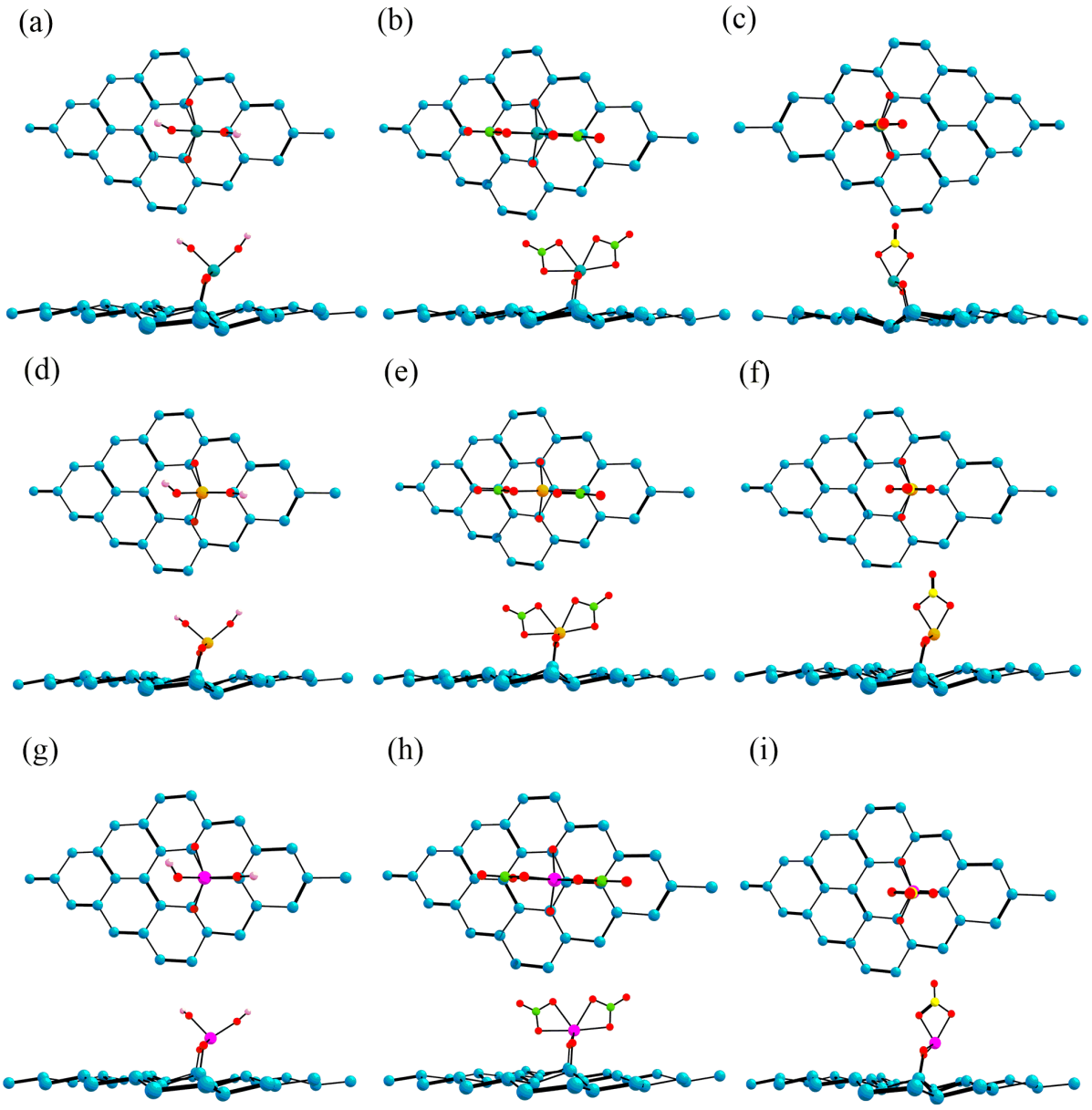

Figure S4 Optimized geometries of the most stable structures of Ac-complexes adsorbed on pristine silicene supercell, top and side views, PBC calculations.

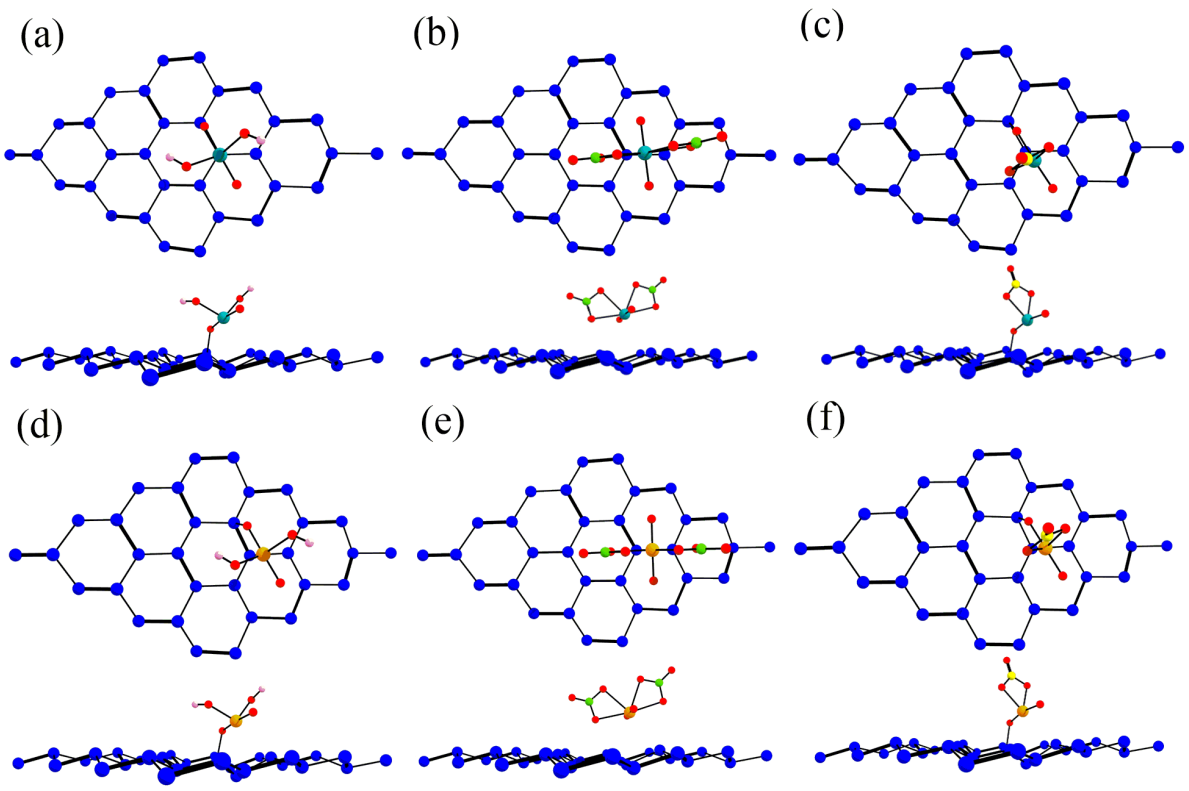

Figure S5 Optimized geometries of 4x4x1 supercell containing germanene and (a) $[UO_2(OH)_2]$, (b) $[UO_2(NO_3)_2]$, (c) $[UO_2(CO_3)]$, (d) $[NpO_2(OH)_2]$, (e) $[NpO_2(NO_3)_2]$, and (f) $[NpO_2(CO_3)]$ (PBC).

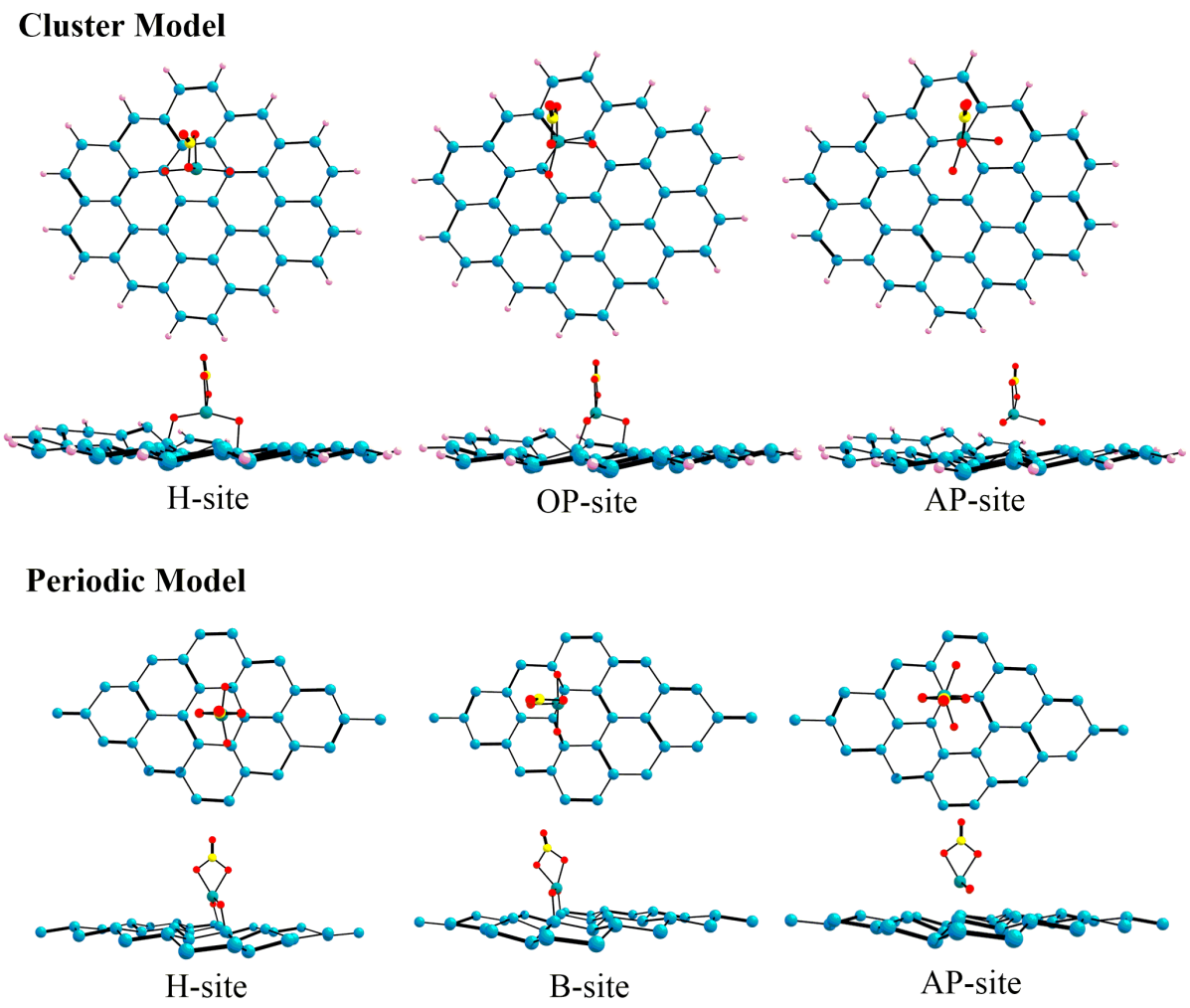

Figure S6 Representative geometries of less favourable sites for the $[UO_2(CO_3)]$ complex adsorbed on $Si_{42}H_{16}$ cluster in water solvent and for PBC calculations, respectively. There is no Si—O bond observed for the AP-site.

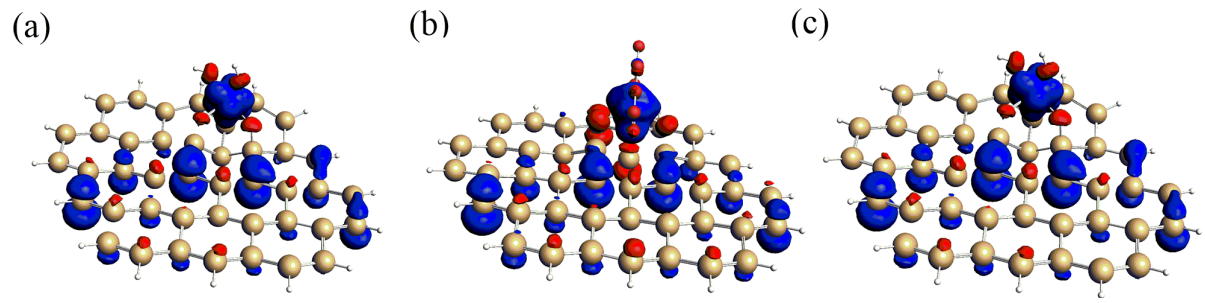

Figure S7 Spin density plots for the adsorption of (a) $[UO_2(OH)_2]$, (b) $[UO_2(NO_3)_2]$, (c) $[UO_2(CO_3)]$ on a $Si_{42}H_{16}$ flake.

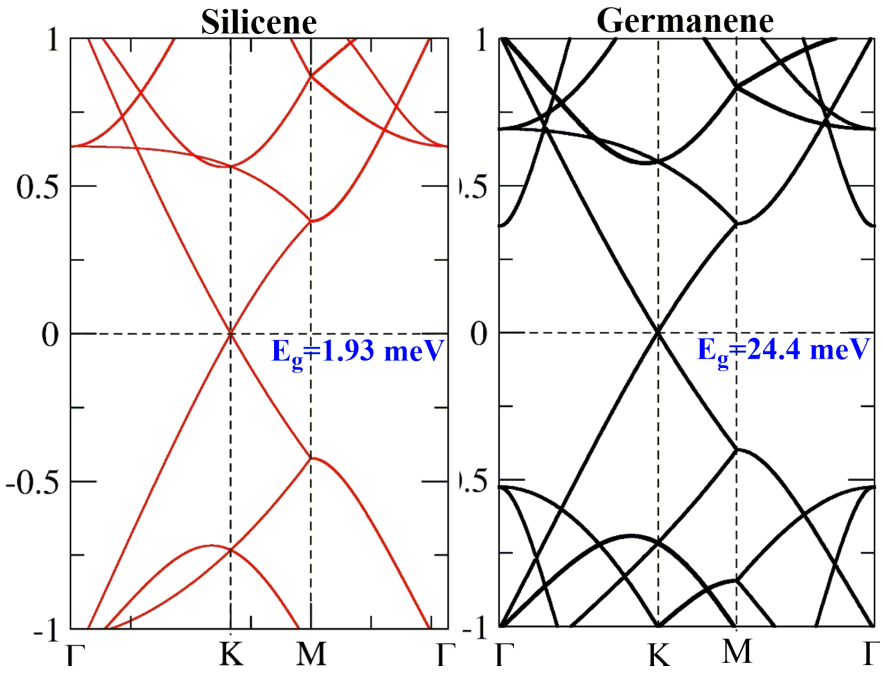

Figure S8 Electronic band structure with band gap value (E_g) for pristine silicene (left) and germanene(right). The Fermi level is set to zero.

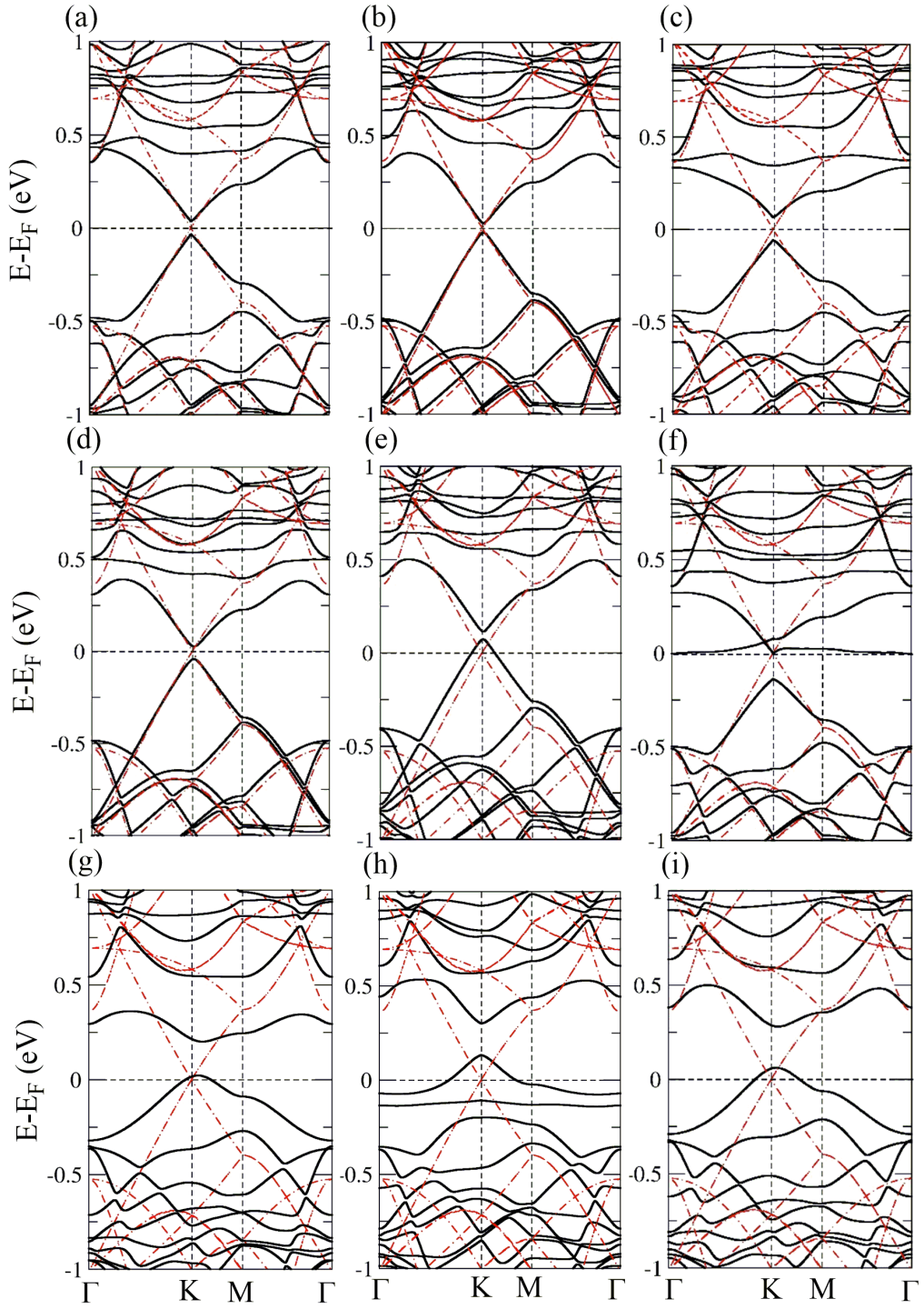

Figure S9 Electronic band structure of germanene with adsorbed (a) $[UO_2(OH)_2]$, (b) $[UO_2(NO_3)_2]$, (c) $[UO_2(CO_3)]$, (d) $[NpO_2(OH)_2]$, (e) $[NpO_2(NO_3)_2]$, (f) $[NpO_2(CO_3)]$, (g) $[PuO_2(OH)_2]$, (h) $[PuO_2(NO_3)_2]$ and (i) $[PuO_2(CO_3)]$. The red dashed lines stand for pristine germanene. The Fermi level is set to zero.

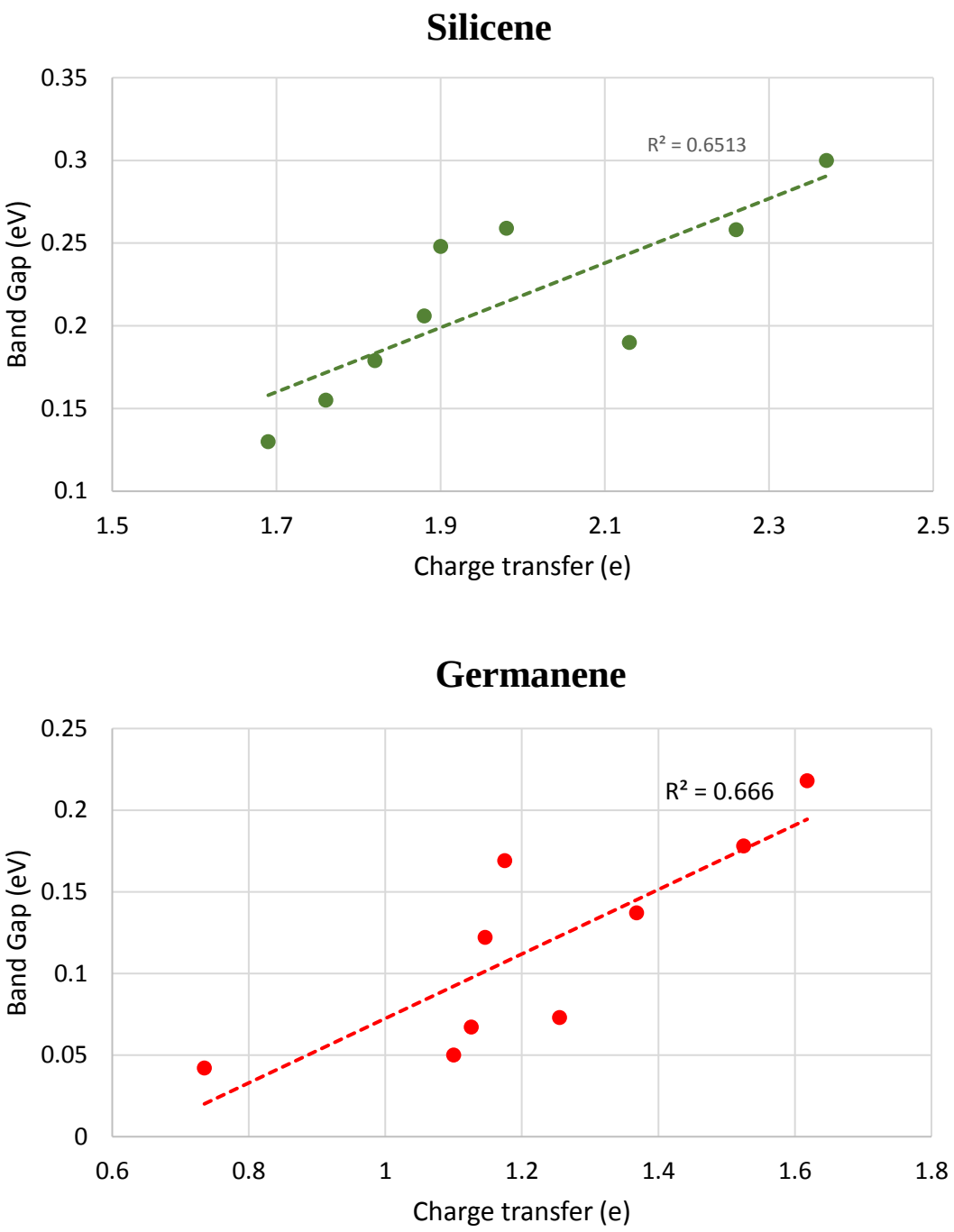

Figure S10 Linear correlation between band gap (eV) and charge transfer (e) for actinide adsorption on silicene and germanene surface under PBC.

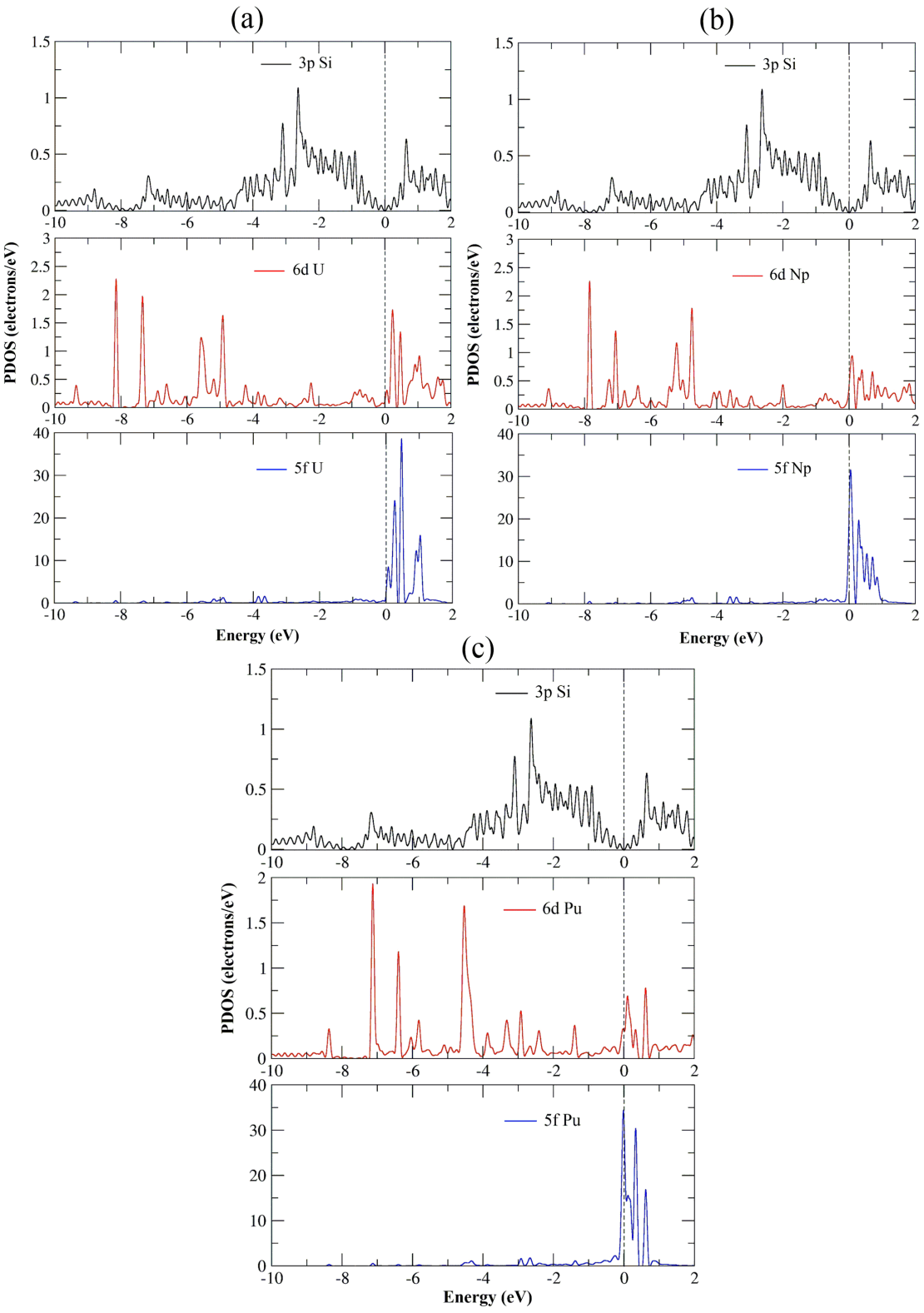

Figure S11 The PDOS of Ac-carbonate complexes, (a) $[UO_2(CO_3)]$ (b) $[NpO_2(CO_3)]$ and (c) $[PuO_2(CO_3)]$, adsorbed on silicene surface under PBC.

Chapter 4

A first-principles study of adsorption of actinide complexes on borophene

4.1 Abstract

First-principles calculations were used to investigate previously unexplored adsorption of actinide complexes on the recently synthesized 2D material borophene. Both the buckled and line-defective planar phases of borophene have been used to study the adsorption of actinide complexes of U to Pu with environmentally relevant ligands including OH^-, NO_3^-, CO_3^{2-}. Various adsorption configurations, corresponding adsorption energies, charge transfer, and electronic properties were studied. All the possible adsorption sites for both types of borophene have been investigated for each adsorbate. The calculated results reveal the presence of strong interactions due to the formation of chemical bonds between B and the oxo ligand of the adsorbate which leads to the reduction of the central actinide metal atom. Comparing the different actinides, periodic trends were established which indicate strong affinity in case of Pu complexes as compared to Np and U complexes. The presence of buckling in borophene contributes towards the strength of adsorption, thus, buckled borophene is a highly suitable candidate for adsorption of actinide complexes in comparison to planar borophene.

4.2 Introduction

With decades of nuclear weapons production and the immense consumption of nuclear energy, nuclear waste and pollution is a major concern for scientists and society in general.[1,2] The spent fuel which discharges from a nuclear power plant constitutes the major part of nuclear waste. The

main components of the waste fuel include uranium, plutonium, neptunium, americium, curium and various other long-lived species.[3] Their disposal requires one hundred thousand years of safe storage, and various techniques such as ion exchange[4] reactions to remove NO^{3-} and uranium from contaminated groundwater, filtration by membranes[5] such as polyamidoamine (PAMAM) dendronized hollow fiber membranes (HFMs) that were synthesized and used in the recovery of heavy metal ions and precipitation methodologies[6] for the treatment of chelated heavy metal-containing wastewater have been widely used to remedy increasing contamination of environment. Various experimental and theoretical reports in the literature have shown the adsorption technique as the simplest and most cost-effective method for assessing radioactive contamination related to the nuclear waste problem.[7,8] High surface to volume ratio along with the presence of a large number of active sites in the structure of two dimensional (2D) materials have made them ideal adsorbents for the remediation of nuclear waste.[9–11]

The field of 2D materials began with the discovery of graphene, first developed by Novoselov et al.[12] through mechanical exfoliation in 2004. The 2D carbon-based material graphene gained a huge amount of attention due to its extraordinary properties such as thermal stability[13], high surface area, charge carrier mobility[14], special structural characteristics with high performance[15], etc. The display of sensitivity even at low concentrations have made 2D materials suitable for various applications including gas sensors[16], protein binding, dye adsorption, and other fields[16]. The main principle of sensing technology involves charge transfer induced by acceptors or donors on the surface of the 2D material which leads to an alteration in the electronic structure of the adsorbing surface[17]. Boron, being a neighbor of carbon in the periodic table, has exceptional electronic properties and hence, boron clusters have gained enormous interest[18]. In recent years, borophene consisting of a monolayer of B atoms with a hexagonal structure has been synthesized by its

deposition on an Ag (111) surface[19–21]. Borophene exhibits properties similar to graphene and other types of 2D materials such as high specific surface area, mechanical strength, and unique anisotropic metallic character which further leads to interesting magnetic and electronic properties[22–26]. It has been also investigated as an ideal anode material for Na-ion batteries due to its exceptional properties[27].

Boron shows up to 16 reported bulk allotropes[28,29]. Various structures such as planar or quasi-planar boron clusters, for example, B_{12}^-, B_{13}^+, B_{19}^- and B_{36} have been predicted and then successfully synthesized with different vacancy densities and arrangements[30–32]. For borophene, i.e. boron sheets, some previous reports have suggested a buckled structure with each B atom being bonded with two adjacent atoms in the same plane and one B atom from a different plane whereas recent reports suggest a planar structure which is metallic, flat and composed of mixtures of hexagons and triangles[33–35]. Both types of structures have been grown on an Ag(111) substrate. Theoretical studies have been done for studying the adsorption of various small gas molecules such as NH_3, CO_2, CO, NO, etc. on both types of structures[36,37]. The application of borophene for rechargeable batteries by considering the adsorption of Ca, Mg, Na and Li atoms with single layer and free-standing borophene has been investigated using density functional theory (DFT) calculations[38]. The sensing behavior of borophene towards $COCl_2$ and CO has been studied by calculating the binding energy and electronic density of states (DOS)[39]. At present, no studies have been reported for the adsorption of actinides/lanthanides on a borophene surface.

In the present study, we have used first-principles DFT calculations to study the interaction of both, buckled/striped (N1) and line-defective β-12 (N2) structure of borophene, with $AcO_2(OH)_2$, $AcO_2(NO_3)_2$, $AcO_2(CO_3)$ where Ac = U, Np, Pu to employ the metallic character of borophene for radioactive material sensing. We have investigated the possible adsorption sites (adsorption

energies), charge transfer, and electronic structures to gain knowledge about the interaction happening between borophene and the actinide complexes.

4.3 Computational Details

To investigate the adsorption characteristics of actinide complexes on buckled as well as planar monolayer structures of borophene, spin-unrestricted first-principles calculations were done in the framework of DFT as implemented in the PWSCF code[40]. The generalized gradient approximation in the form of the Perdew–Burke–Ernzerhof functional (PBE) was used for the exchange-correlation potential[41] and van der Waals (vdW) corrections proposed by Grimme (DFT-D3)[42] along with BJ damping[43] were employed due to their good description of long-range non-covalent vdW interactions between adsorbate and adsorbent[44,45]. The calculations employed periodic boundary conditions and plane-wave expansion of the orbitals. Scalar relativistic projector augmented wave pseudopotentials[46] have been employed with a high plane wave cutoff at an energy of 816 eV. To avoid artificial inter-layer interactions between adjacent monolayers, a minimum spacing of 20 Å has been used in the z-direction. A 24×24×1 k-mesh was used for Brillouin zone sampling (Monkhorst−Pack scheme[47]) for 64 atoms (N1) and 75 atoms (N2) borophene supercells, see Figure 4.1. All atomic positions (with and without adsorbed complexes) were relaxed with a force tolerance limit of 1×10^{-3} eV/Å.

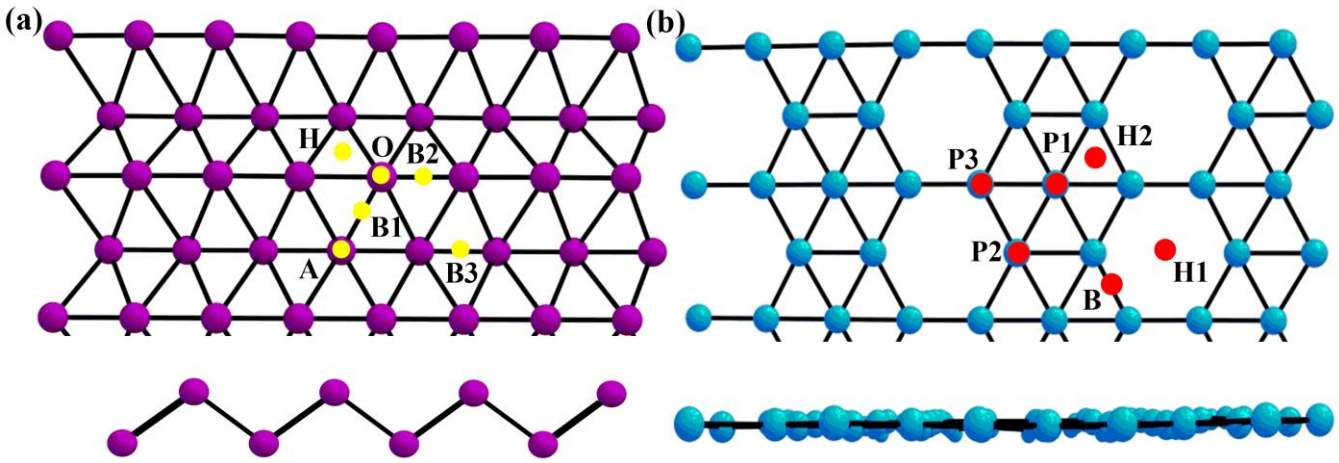

Figure 4. 1 Supercell of (a) N1 and (b) N2 borophene with possible adsorption sites.

To start with, we fully relaxed the rectangular unit cell of N1 borophene containing 2 atoms and N2 borophene containing 5 atoms per unit cell. The relaxed lattice constants were found to be a=1.61 Å, b=2.87 Å for N1 borophene and, a=2.93 Å, b=5.07 Å for N2 borophene, which is in good agreement with the earlier reported values[48]. These results indicate the accuracy of our model for this study. These relaxed parameters of the unit cell were used to create an 8×4×1 supercell for the buckled N1 and a 5×3×1 supercell for the planar N2 structure of borophene, as shown in Figure 4.1. Adsorption energies $E_{ad} = E_{borophene\text{-}complex} - (E_{borophene} + E_{complex})$ were calculated, where $E_{borophene\text{-}gas}$, $E_{borophene}$, E_{gas}, are the total energies of the combined adsorbent-adsorbate system of actinide complex with borophene, pristine borophene, and the actinide complex respectively. A high negative value of E_{ad} indicates that the complex molecule is adsorbed strongly, whereas a positive value means that it is repelled by borophene. The amounts of charge transfer from/to the actinide complex as a result of the adsorption were determined by Löwdin charge analysis[49] (difference between partial charges before and after adsorption).

4.4 Results and Discussion

There are six different adsorption sites possible in principle on both types N1 and N2 of borophene structures, as shown in Figure 4.1. For N1 borophene, these are characterized by the adsorbed complex being on top of an upper B atom (A-site), on top of a lower B atom (O-site), on top of the bond between one upper and one lower B atoms (B1-site), above the bond between two lower B atoms (B2-site), over the bond between two upper B atoms (B3-site) and on the triangular hollow space (H-site) For N2 borophene, the sites are the following: on top of a B atom at the center of hexagonal ring (P1-site), above two different B atoms (P2- and P3-sites), on top of the hexagonal hollow space (H1-site), over the triangular hollow space (H2-site) and on the bond between two B atoms (B site). Three types of neutral actinide complexes with environmentally important ligands have been chosen for this study. They include $AcO_2(OH)_2$, $AcO_2(NO_3)_2$ and AcO_2CO_3 where Ac= U, Np, and Pu. We performed the geometry relaxation by placing each actinide complex on the above-mentioned sites for N1 and N2. For each actinide complex, we tried to cover all the possible orientations by systematically placing different types of atoms present in each complex into various possible positions. For instance, for $[UO_2(OH)_2]$, we put U, O (oxo ligand) and O (from OH^-) on the various possible adsorption sites of borophene. The most favorable site which is the site with strongest adsorption interaction (see Table B1 in appendix for this chapter) has been studied further for structural parameters, charge transfer and electronic structure for each complex. The optimized structures of the preferred orientation for the adsorption on N1 and N2 have been provided in the Appendix (Figures B1 and B2). The optimized structures of the carbonate complexes $[UO_2(CO_3)]$, $[NpO_2(CO_3)]$, and $[PuO_2(CO_3)]$ adsorbed on N1 and N2 can also be seen in Figure 4.2.

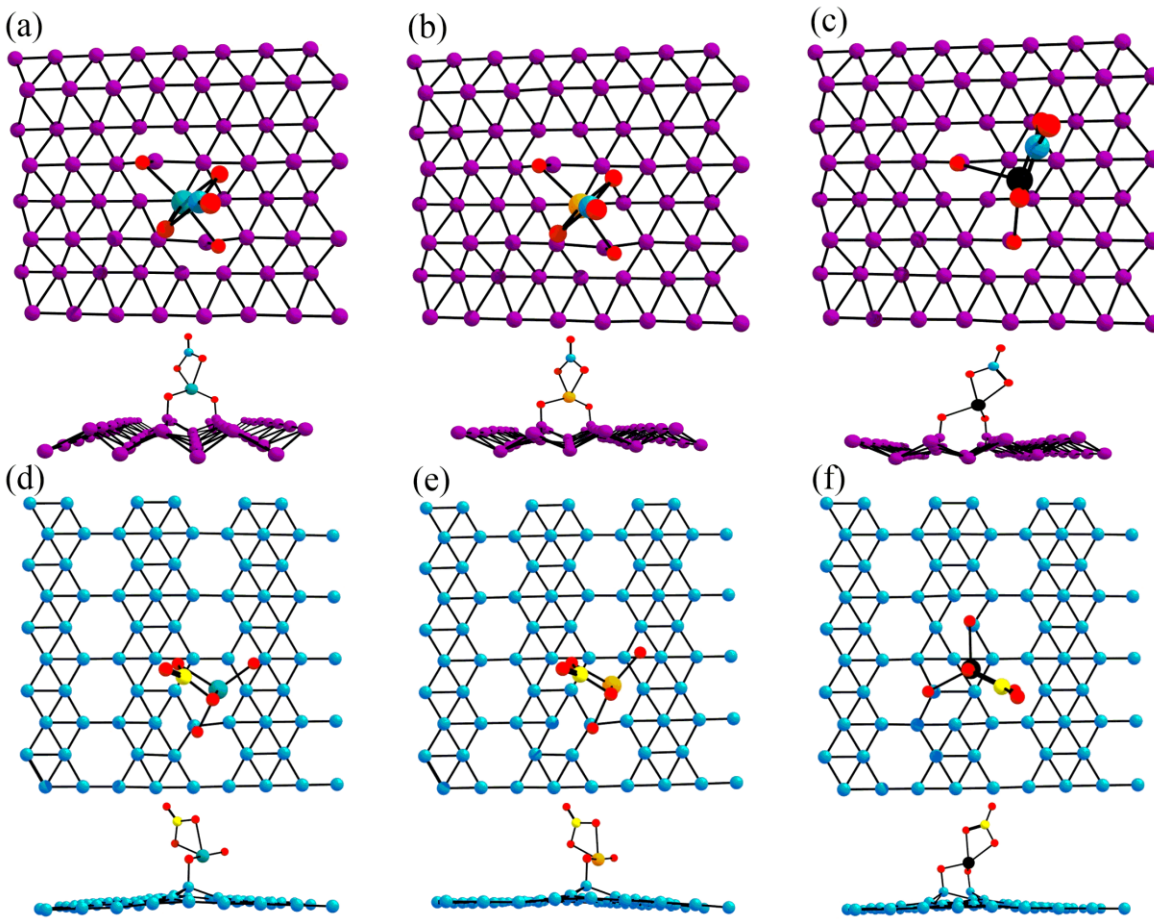

Figure 4.2 Side and top view of the most stable sites for (a) [$UO_2(CO_3)$], (b) [$NpO_2(CO_3)$], and (c) [$PuO_2(CO_3)$] on N1 borophene, and (d) [$UO_2(CO_3)$], (e) [$NpO_2(CO_3)$], and (f) [$PuO_2(CO_3)$] on N2 borophene.

In all the systems, the oxo ligands of the actinide complexes are pointing towards the borophene sheet and thus, forming B—O bonds after adsorption (see Figure B3). The bond lengths of Ac—O bonds have been hugely modified upon adsorption. For U-complexes, the U—O bond lies in the range of 1.78-1.80 Å before adsorption and it has been elongated to a range of 1.99-2.03 Å after adsorption on N1 and 1.93-1.98 Å for N2 adsorption with the newly formed B—O bonds falling into the range of 1.41-1.44 Å and 1.51-1.52 Å respectively. Similarly, for adsorption of Np and Pu complexes on N1 and N2 borophene, there is even stronger elongation of the Ac—O bond in the case of N1 adsorption as compared to N2 adsorption. The Pu—O bonds became weakest with an

average bond length of 2.11 Å as compared to U—O and Np—O bonds which elongate to the average bond lengths of 2.01 Å and 2.04 Å for N1 adsorption. On the other hand, for the N2 case, the average Pu—O bond is 2.02 Å that is, smaller than for N1 adsorption. Therefore, the B—O bonds are strongest in Pu-complexes with average bond distances of 1.35 Å and 1.47 Å for N1 and N2 respectively. These results are in good agreement with the adsorption energies pattern (Tables B1 and B2). Out of all the possible adsorption sites for N1 borophene, we found that the O-site is most favorable for the hydroxide complexes of U to Pu with the adsorption energy lying in the range of -1.529 to -2.456 eV. The strongly favored anchoring positions by actinide complexes on both N1 and N2 sheets are listed in terms of the position of the central metal actinide atom obtained after optimization. The adsorption energies for the other, less stable sites have been provided in the Appendix for all systems under study (see Tables B1 and B2). For the nitrate complexes adsorbed on N1, strong interactions have been observed at the B1-site in case of U and Np with energy values of -0.866 eV and -0.937 eV respectively whereas the O-site is most favorable for adsorption of the Pu complex with an energy of -1.663 eV. The lowest energy site for the carbonate complexes adsorbed on N1 is the O-site with energy values of -1.600 eV and -1.810 eV for $[UO_2(CO_3)]$ and $[NpO_2(CO_3)]$ respectively. For the same carbonate ligand, we find strong binding energy of -2.584 eV at the B1-site for $[PuO_2(CO_3)]$ with the highest stability of all complexes. In terms of periodic trends, the Pu complexes show the highest affinity towards the N1 sheet followed by the Np complexes with the U complexes having the lowest interactions. Regarding the ligands, carbonate shows the strongest adsorption which is followed by hydroxide and nitrate respectively. The difference between the carbonate and nitrate systems may be the result of reduced steric hindrance in the carbonate complexes where one CO_3^{2-} ligand is supplying two equatorial bonds to the central actinide metal atom whereas there are four equatorial bonds in the case of the nitrate

complexes. Hydroxide, on the other hand, is a stronger equatorial ligand which can be seen in molecular systems as well[50–52]. This leads to weakening of the other bonds, including the surface interaction. On comparing the results with our work for the silicene system, the nitrate and carbonate complexes are strongly adsorbed on silicene with a high adsorption energy of -2.001 eV for $[PuO_2(NO_3)_2]$ and -2.590 eV for $[PuO_2(CO_3)]$ as compared to N1 borophene whereas, for hydroxide complexes, the Pu-complex is more strongly adsorbed on N1 borophene with an energy of -2.460 eV compared to -2.115 eV for silicene[53]. The periodic trends, as well as ligand behavior in terms of interactions, are similar between silicene and borophene. The adsorption energy trends are further supported by the charge transfer analysis. The amount of charge transfer from the N1 sheet to actinide complexes is not only pointing towards the reduction of the central metal actinide atom but also indicates the presence of a primarily ionic type of bonding. The charge transfer shows a linear relationship with the strength of adsorption. Adsorption energy and charge transfer values have been summarized in Figure 4.3.

The adsorption energy values are considerably different between N1 and N2 borophene due to the different bonding environments experienced by molecules on the buckled (N1) and planar (N2) structures. The N2 borophene shows weaker adsorption interactions as compared to N1 borophene, which points toward a relationship between adsorption and the presence of buckling in the sheet. This has been already observed in the stronger interactions present in buckled silicene as compared to planar graphene[54–56]. The H1-site has been found energetically most favorable for all the complexes adsorbed on N2 borophene with just two exceptions. The hydroxide and carbonate complexes of Pu bind most strongly on the H2-site as compared to the H1-site with energy values of -1.905 eV and -1.955 eV respectively. Similar trends in terms of the strength of adsorption can be observed for N2 borophene as for N1 borophene regarding ligands and central actinide metal

atom despite the fact that one structure is buckled and the other one is planar with line-defects. The variation of charge transfer with the binding interactions for N2 have been shown in Figure 4.3 (c)-(d). Our results show the better compatibility of borophene for actinide material sensing as compared to graphene as the values in the case of borophene exceed the previously reported values for adsorption on graphene where a maximum adsorption energy value of 2.1 eV has been reported for the adsorption of U(VI) on carboxylated graphene oxide (HOOC-GOs)[57].

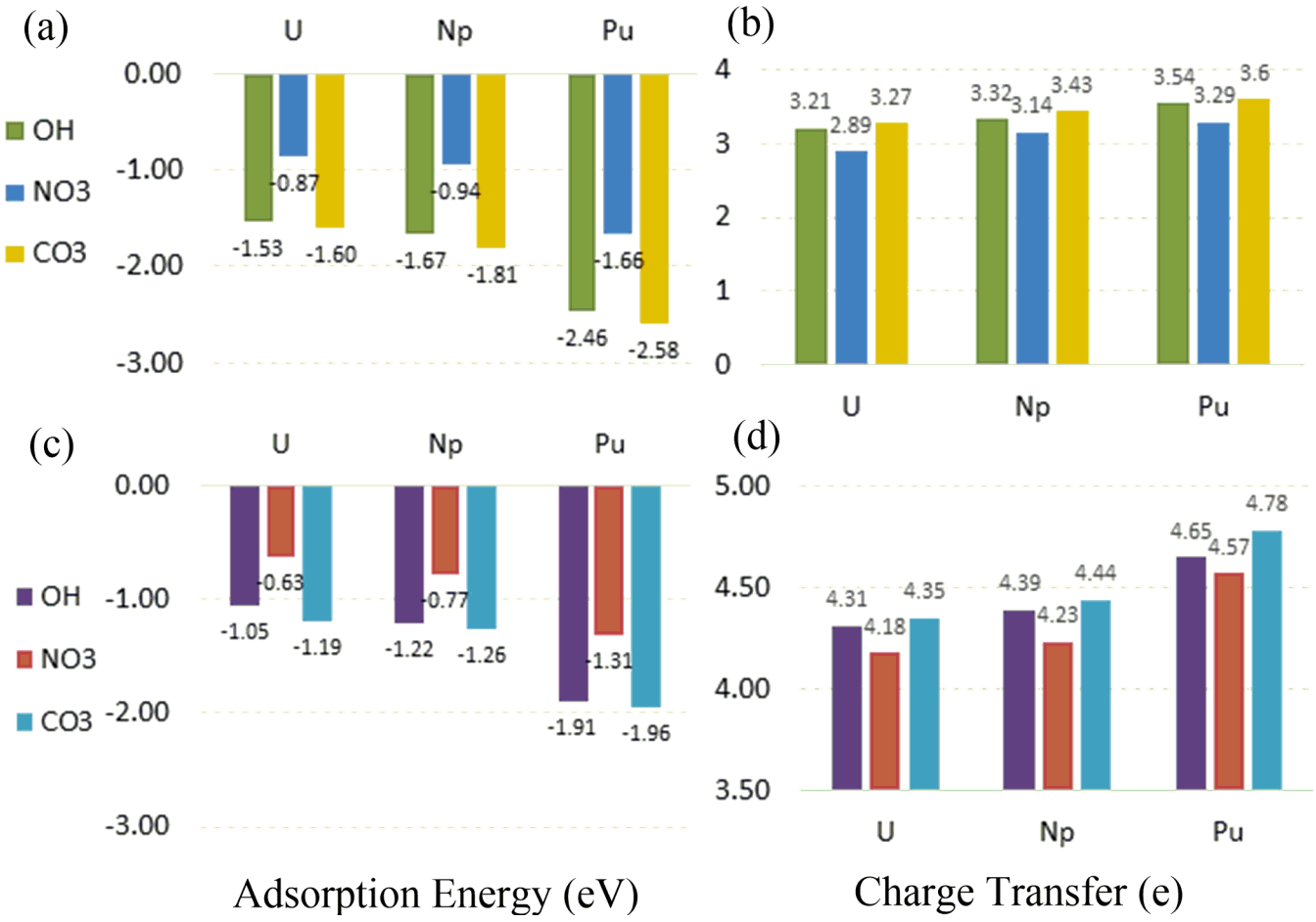

Figure 4.3 Adsorption energy and charge transfer for the most stable cases of Ac- complexes adsorbed on N1 borophene (a), (b) and N2 borophene (c), (d) respectively.

The geometrical parameters of N1 and N2 borophene have undergone a lot of alteration upon adsorption, see Tables 4.1 and 4.2, which indicates the presence of some kind of interactions

between adsorbed complex and the borophene sheet. In Table 4.1, d (Å) is the distance between the adsorbed central metal atom of Ac-complex and the borophene sheet, Θ (deg) is the hexagonal angle between three adjacent B atoms, a1-a2 is the B—B bond length between B atoms that are both lower or higher, respectively, a3 is the bond length between one lower and one higher B, and Δ (Å) is the buckling parameter for N1 borophene. The presence of two newly formed bonds between B and the oxo ligands of the actinide complex is evidence for strong adsorption interactions in the N1 borophene system. However, for N2 borophene, the structures with only one newly formed B—O bond are more stable than those with two B—O bonds except for $[PuO_2(OH)_2]$ and $[PuO_2(CO_3)]$ where we still observe two B—O bonds (see Appendix Figure B2) to be more favorable. Due to the presence of such bonding in both systems, adsorption of the actinide complexes results in distinct distortion of the structure of borophene. Similar effects have also been observed in a previous study of the adsorption of small gas molecules on borophene[58] where it was termed as the development of wrinkles in the structure.

System	d (Å)	Θ (deg)		B—B (Å)		Δ (Å)
		Θ_1	Θ_2	a1-a2	a3	
Borophene	--	100-101	116-117	1.64-1.67	1.88	0.91
$UO_2(OH)_2$	2.99	97-98	104-122	1.67-1.80	1.78-1.96	1.15
$UO_2(NO_3)_2$	3.45	84-90	121-142	1.69-1.80	1.85-2.60	1.69
$UO_2(CO_3)$	2.92	97-98	105-121	1.66-1.80	1.79-2.04	1.19
$NpO_2(OH)_2$	3.17	98-101	94-131	1.63-1.80	1.84-2.34	1.34
$NpO_2(NO_3)_2$	3.61	90-106	90-143	1.61-1.82	1.73-2.57	1.59
$NpO_2(CO_3)$	2.86	98-99	103-123	1.67-1.80	1.77-1.98	1.13
$PuO_2(OH)_2$	3.97	99-102	98-122	1.67-1.83	1.71-2.03	1.20
$PuO_2(NO_3)_2$	4.05	100-101	98-121	1.67-1.84	1.70-1.96	1.19
$PuO_2(CO_3)$	3.26	97-102	98-122	1.66-1.82	1.70-2.04	1.39

Table 4.1 Optimized geometrical parameters for actinide complexes adsorbed on N1 borophene where d (Å) is the distance between the adsorbed Ac-complex and borophene sheet, Θ_1 (deg) is the angle of the hexagonal motif with two adjacent lower/higher B atoms and one higher/lower B, Θ_2 (deg) is hexagonal angle for one higher-one lower-one higher B, bond length of B—B in Å, and Δ (Å) is the average perpendicular distance between adjacent B atoms.

The average distance of the complex binding to the N1 sheet is 3.36 Å, whereas, for N2 borophene, the complexes were found to be closer to the sheet with an average distance of 2.53 Å (see Table 4.2). In both cases, there is a lot of variation in the hexagonal angle. In case of N1 borophene, the pristine borophene shows angle range of 100-101° for Θ_1 and 116-117° for Θ_2 which have been modified hugely to a minimum value of 84° (Θ_1) and a maximum of 143° (Θ_2) (see Table 4.1), whereas, for N2 borophene, this variation is somewhat smaller and has the range of 105°-123°. There is shortening as well as elongation of B—B bond lengths in the borophene sheets pointing towards the presence of some kind of interactions with the different adsorbates. The most

interesting change is seen in the buckling parameter. Due to the bonding between B and the oxo ligand, the boron atoms from the sheets rise, thus leading to alterations in the buckling. The pristine planar N2 borophene which earlier had no buckling now exhibited a range from 0.61 to 0.78 Å whereas, for buckled N1 borophene, this parameter further increases to a maximum of 1.69 Å.

System	d (Å)	Θ (deg)	B—B (Å)	Δ (Å)
Borophene	--	120-121	1.64-1.75	0.00
$UO_2(OH)_2$	2.48	107-121	1.65-1.82	0.64
$UO_2(NO_3)_2$	2.62	107-122	1.64-1.81	0.71
$UO_2(CO_3)$	2.45	106-123	1.65-1.83	0.69
$NpO_2(OH)_2$	2.32	107-123	1.66-1.82	0.65
$NpO_2(NO_3)_2$	2.57	106-123	1.64-1.83	0.67
$NpO_2(CO_3)$	2.30	108-123	1.65-1.83	0.72
$PuO_2(OH)_2$	2.63	107-119	1.66-1.89	0.78
$PuO_2(NO_3)_2$	2.65	105-123	1.65-1.85	0.72
$PuO_2(CO_3)$	2.75	106-118	1.67-1.88	0.61

Table 4.2 Structural parameters for pristine N2 borophene supercell and actinide complexes adsorbed on N2 borophene sheet.

The variation in the bond length of Ac—O from the relaxed structure due to complexation alongwith the bond lengths of newly formed B—O bonds in each case has been summarized in Figure B3 (Appendix) for N1 and N2 borophene. The variation for the strongly adsorbed carbonate complexes is also shown in Figure 4.4. The Ac—O bond (Ac= U, Np, Pu) gets weakened and longer as we move from U to Pu. This trend contrasts the normal actinide contraction that is seen, for instance, in the free complexes, and thus, supports the presence of particularly strong adsorption interactions (including strong B–O bonds) in case of Pu. High adsorption energies

together with short atomic distances as well as large charge transfers indicate that a new chemical bond (B—O) is formed for all actinide complexes.

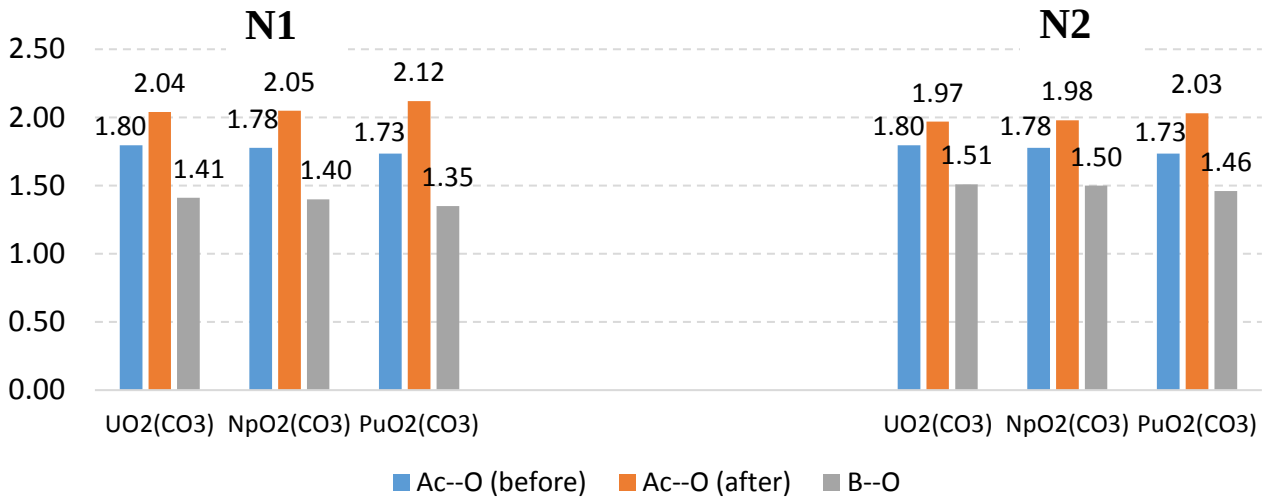

Figure 4.4 Bond length (in Å) comparison of Ac—O bonds in carbonate complexes before (blue color) and after (red color) adsorption on N1 and N2 borophene where Ac= U, Np, and Pu. The green color indicates the bond length of the newly formed B—O for each complex adsorbed on borophene sheet.

Electronic band structures of the pristine borophene supercell have been evaluated by including spin-orbital coupling for both N1 and N2, see Appendix (Figure B4). The contribution of the complexes to the electronic properties of borophene can be seen in Figures S5 and B6 (Appendix). After the adsorption of actinide complexes, the conduction bands have moved towards the Fermi level thus making the system more metallic. Similar types of band diagrams have been seen in previous studies for adsorption of NO and NO_2 on borophene[59]. The electronic band structure diagrams for the carbonate complexes of U to Pu for N1 and N2 are shown here as well in Figure 4.5.

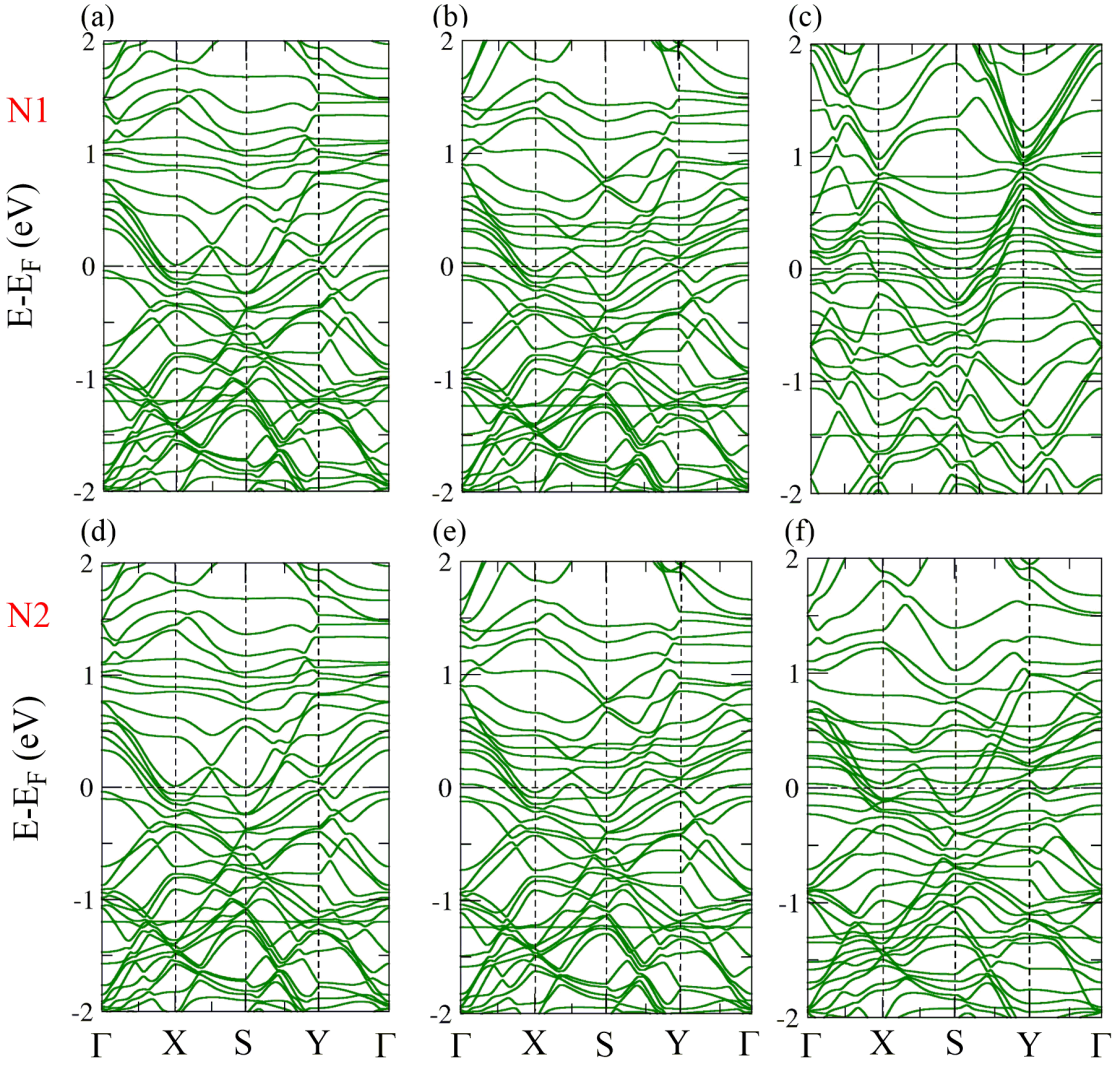

Figure 4.5 The electronic band structure diagrams for (a) [$UO_2(CO_3)$], (b) [$NpO_2(CO_3)$], (c) [$PuO_2(CO_3)$] adsorbed on N1, and (d) [$UO_2(CO_3)$], (e) [$NpO_2(CO_3)$], (f) [$PuO_2(CO_3)$] on N2 borophene without spin-orbital effects.

Detailed insight into the electronic structures of the adsorbate-adsorbent system can be obtained from the Density of States (DOS) which is an important technique to analyze the bonding among atoms as it describes the number of states with a particular energy. The total DOS plots for the N1 borophene system with different adsorbates are shown in Figure 4.6. It can be clearly seen that the contributions of carbonate complexes are closer to the Fermi level as compared to the hydroxide complexes which are further followed by nitrate complexes. This can again be related to the

relative binding strengths of these ligands, as discussed above. In terms of periodic trends, in the U-complexes the states from the complexes localize at lower energy levels near the valence band and they have started moving up toward the Fermi energy as we go to Np and further to Pu complexes. Similarly, the conduction band which is at higher levels in the U-complexes has transitioned down towards the valence band states in Pu-complexes. Such a higher contribution from the adsorbate complexes affects the transport behavior of N1 borophene by changing the band gap in the electronic structure. In fact, the DOS of borophene with an adsorbed actinide complex has been hugely modified from the pristine borophene case. Equivalent behavior has been observed in the case of N2 borophene (see Figure B7, Appendix). Comparison between the DOS plots of N1 and N2 borophene with adsorbates shows more contributions from the states of the different actinide complexes closer to the Fermi level in case of N1 borophene thus further supporting our results from the adsorption energy calculations. The partial density of states plots for the strongly adsorbed carbonate complexes of U, Np, and Pu bonded on the N1 layer are shown in the Appendix (Figure B8), illustrating the contributions from 6d and 5f orbitals. There is more contribution from 5f orbitals in case of $[PuO_2(CO_3)]$ as followed by $[NpO_2(CO_3)]$ and $[UO_2(CO_3)]$ which are having stronger 6d contributions. These results can be further analyzed for energy-degeneracy-driven covalency in actinide bonding[60] for which Jing Su et al. reported an increase in 5f orbital mixing on moving from Th to Pu[61] which is quite similar in the present case as we see higher f-contribution in the lower occupied bands for Pu-complexes as compared to U and Np-complexes.

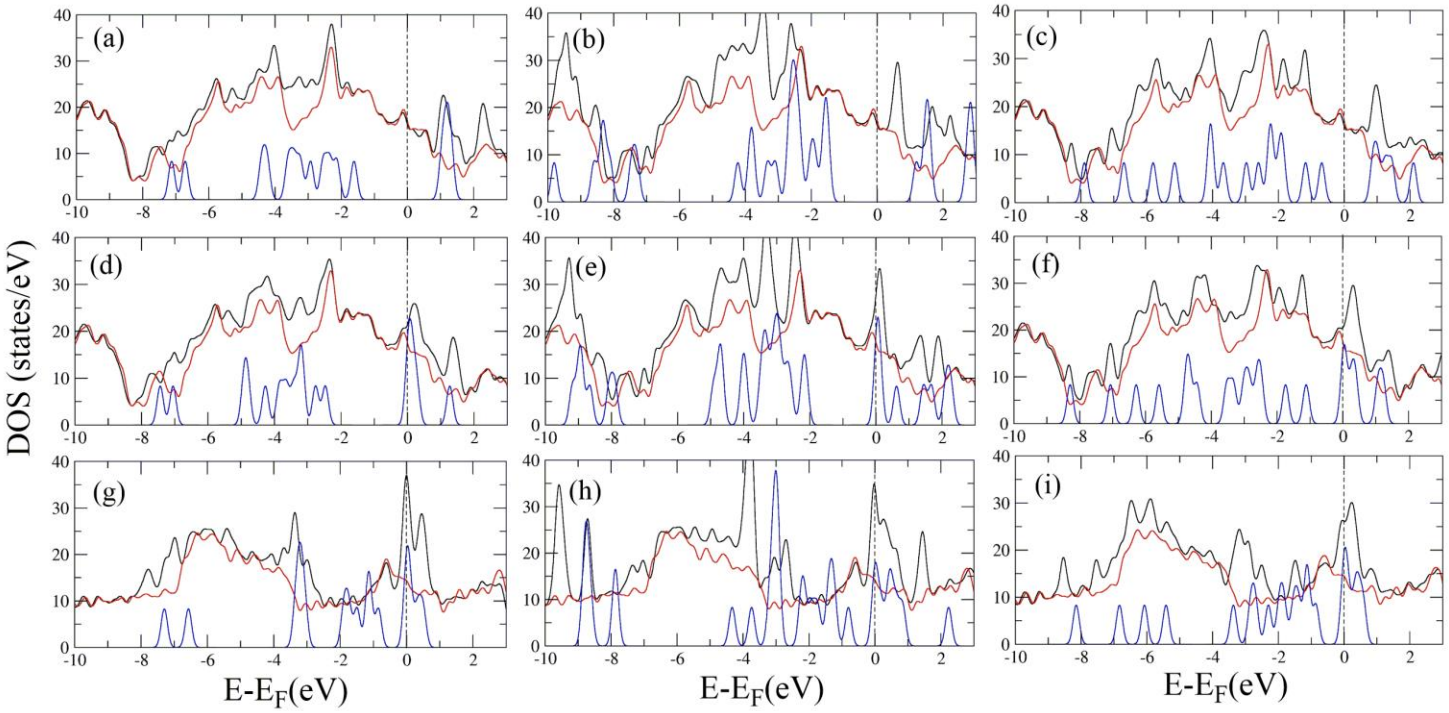

Figure 4.6 Density of states for (a) $[UO_2(OH)_2]$, (b) $[UO_2(NO_3)_2]$, (c) $[UO_2(CO_3)]$, (d) $[NpO_2(OH)_2]$, (e) $[NpO_2(NO_3)_2]$, (f) $[NpO_2(CO_3)]$, (g) $[PuO_2(OH)_2]$, (h) $[PuO_2(NO_3)_2]$, and (i) $[PuO_2(CO_3)]$ on N1 borophene. The black color stands for pristine N1 borophene supercell, red color represents N1 borophene with adsorbed actinide complex, and blue color shows contribution from adsorbed actinide complex. The Fermi level is set to zero.

4.5 Conclusions

In conclusion, we performed a first-principles study of adsorption of radioactive actinide complexes on borophene to discuss the possibility and consequences of the interaction with planar as well as buckled borophene. The preferable adsorption sites, structural parameters, adsorption strengths as well as electronic properties have been determined. Our results indicate that the two most favorable sites are the B1-site and O-site for adsorption on N1 borophene whereas the hollow sites (H1 and H2) are more suitable for N2 borophene. The carbonate complexes have the largest adsorption energies followed by hydroxide and nitrate complexes. This can be rationalized with simple arguments about steric factors and ligand binding strength. Periodic trends have been

demonstrated with the strongest adsorption interactions shown by Pu complexes such as $[PuO_2(CO_3)]$ with an adsorption energy of -2.584 eV on N1 borophene. The formation of B—O bonds results in strong interactions which further leads to the reduction of the central metal from +6 to +4 oxidation state. We also systematically compared N1 and N2 borophene to investigate the effect of the presence of buckling on the binding interactions. According to our results, the presence of buckling in two-dimensional materials is a boost for strong adsorption interactions which is further useful for sensing technology. Our results are comparable with similar studies done on (buckled) silicene where strong adsorption interactions are present in case of silicene due to the presence of even stronger Si—O bonds. Remarkably high adsorption energies with large charge transfer from borophene to actinide complexes demonstrate the excellent ability of borophene to act as a sensor for radioactive material. On the other hand, the distortions occurring in the two-dimensional borophene because of strong adsorption reduce the reusability of borophene sheets due to large structural changes as well as difficult removal of strongly adsorbed complexes and thus, require further detailed investigation.

Bibliography

1. Clark, D. L., Hobart, D. E. & Neu, M. P. Actinide carbonte complexes and their importance in actinide environmental chemistry. *Chem. Rev.* **95**, 25–48 (1995).
2. M.Thomson, B., A.Longmire, P. & G.Brookins, D. Geochemical constraints on underground disposal of uranium mill tailings. *Appl. Geochemistry* **1**, 335–343 (1986).
3. Magill, J. *et al.* Impact limits of partitioning and transmutation scenarios on the radiotoxicity of actinides in radioactive waste *. *Nucl. Energy* **42**, 263–277 (2003).
4. Baohua Gu, *, Yee-Kyoung Ku, A. & Jardine, P. M. Sorption and binary exchange of nitrate, sulfate, and uranium on an anion-exchange resin. (2004). doi:10.1021/ES034902M
5. Zhang, Q., Wang, N., Zhao, L., Xu, T. & Cheng, Y. Polyamidoamine dendronized hollow fiber membranes in the recovery of heavy metal ions. *ACS Appl. Mater. Interfaces* **5**, 1907–1912 (2013).
6. Fu, F., Xie, L., Tang, B., Wang, Q. & Jiang, S. Application of a novel strategy—advanced Fenton-chemical precipitation to the treatment of strong stability chelated heavy metal containing

wastewater. *Chem. Eng. J.* **189**–**190**, 283–287 (2012).

7. Mashtalir, O. *et al.* Dye adsorption and decomposition on two-dimensional titanium carbide in aqueous media. *J. Mater. Chem. A* **2**, 14334–14338 (2014).

8. Kerisit, S. & Liu, C. Molecular dynamics simulations of uranyl and uranyl carbonate adsorption at aluminosilicate surfaces. *Environ. Sci. Technol.* **48**, 3899–3907 (2014).

9. Wu, Q.-Y. *et al.* Understanding the bonding nature of uranyl ion and functionalized graphene: a theoretical study. *J. Phys. Chem. A* **118**, 2149–2158 (2014).

10. Liu, X., Li, J., Wang, X., Chen, C. & Wang, X. High performance of phosphate-functionalized graphene oxide for the selective adsorption of U(VI) from acidic solution. *J. Nucl. Mater.* **466**, 56–64 (2015).

11. Sun, Y., Ding, C., Cheng, W. & Wang, X. Simultaneous adsorption and reduction of U(VI) on reduced graphene oxide-supported nanoscale zerovalent iron. *J. Hazard. Mater.* **280**, 399–408 (2014).

12. Novoselov, K. S. *et al.* Electric field effect in atomically thin carbon films. *Science (80-.).* **306**, 666 LP – 669 (2004).

13. Nan, H. Y. *et al.* The thermal stability of graphene in air investigated by Raman spectroscopy. *J. Raman Spectrosc.* **44**, 1018–1021 (2013).

14. Morozov, S. V. *et al.* Giant intrinsic carrier mobilities in graphene and its bilayer. *Phys. Rev. Lett.* **100**, 016602 (2008).

15. Castro Neto, A. H., Guinea, F., Peres, N. M. R., Novoselov, K. S. & Geim, A. K. The electronic properties of graphene. *Rev. Mod. Phys.* **81**, 109–162 (2009).

16. Yang, W., Gan, L., Li, H. & Zhai, T. Two-dimensional layered nanomaterials for gas-sensing applications. *Inorg. Chem. Front.* **3**, 433–451 (2016).

17. Kannan, P. K., Late, D. J., Morgan, H. & Rout, C. S. Recent developments in 2D layered inorganic nanomaterials for sensing. *Nanoscale* **7**, 13293–13312 (2015).

18. Jemmis, E. D. & Jayasree, E. G. Analogies between boron and carbon. *Acc. Chem. Res.* (2003).

19. Tai, G. *et al.* Synthesis of atomically thin boron films on copper foils. *Angew. Chemie Int. Ed.* **54**, 15473–15477 (2015).

20. Mannix, A. J. *et al.* Synthesis of borophenes: Anisotropic, two-dimensional boron polymorphs. *Science (80-.).* **350**, 1513 LP – 1516 (2015).

21. Feng, B. *et al.* Experimental realization of two-dimensional boron sheets. *Nat. Chem.* **8**, 563–568 (2016).

22. Sun, H., Li, Q. & Wan, X. G. First-principles study of thermal properties of borophene. *Phys. Chem. Chem. Phys.* **18**, 14927–14932 (2016).

23. Peng, B. *et al.* The electronic, optical, and thermodynamic properties of borophene from first-principles calculations. *J. Mater. Chem. C* **4**, 3592–3598 (2016).

24. Yuan, J., Yu, N., Xue, K. & Miao, X. Ideal strength and elastic instability in single-layer 8-Pmmn borophene. *RSC Adv.* **7**, 8654–8660 (2017).

25. Mortazavi, B., Rahaman, O., Dianat, A. & Rabczuk, T. Mechanical responses of borophene sheets:

a first-principles study. *Phys. Chem. Chem. Phys.* **18**, 27405–27413 (2016).

26. Padilha, J. E., Miwa, R. H. & Fazzio, A. Directional dependence of the electronic and transport properties of 2D borophene and borophane. *Phys. Chem. Chem. Phys.* **18**, 25491–25496 (2016).

27. Liang, P. *et al.* Is borophene a suitable anode material for sodium ion battery? *J. Alloys Compd.* **704**, 152–159 (2017).

28. Bodie, D. & Shi-Ming, B. *Structure and chemistry of crystalline Solids*. *Springer* (Springer New York, 2006).

29. Ogitsu, T., Schwegler, E. & Galli, G. β-Rhombohedral boron: at the crossroads of the chemistry of boron and the physics of frustration. *Chem. Rev.* **113**, 3425–3449 (2013).

30. Kolmogorov, A. N. & Curtarolo, S. Theoretical study of metal borides stability. *Phys. Rev. B* **74**, 224507 (2006).

31. Carenco, S., Portehault, D., Boissière, C., Mézailles, N. & Sanchez, C. Nanoscaled metal borides and phosphides: recent developments and perspectives. *Chem. Rev.* **113**, 7981–8065 (2013).

32. Oganov, A. R. *et al.* Ionic high-pressure form of elemental boron. *Nature* **457**, 863–867 (2009).

33. Li, W.-L. *et al.* The B 35 cluster with a double-hexagonal vacancy: a new and more flexible structural motif for borophene. *J. Am. Chem. Soc.* **136**, 12257–12260 (2014).

34. Penev, E. S., Bhowmick, S., Sadrzadeh, A. & Yakobson, B. I. Polymorphism of two-dimensional boron. *Nano Lett.* **12**, 2441–2445 (2012).

35. Piazza, Z. A. *et al.* Planar hexagonal B_{36} as a potential basis for extended single-atom layer boron sheets. *Nat. Commun. 2014 5* **5**, 3113 (2014).

36. Huang, C.-S., Murat, A., Babar, V., Montes, E. & Schwingenschlögl, U. Adsorption of the gas molecules NH 3 , NO, NO 2 , and CO on borophene. *J. Phys. Chem. C* **122**, 14665–14670 (2018).

37. Liu, T. *et al.* A first-principles study of gas molecule adsorption on borophene. *AIP Adv.* **7**, 125007 (2017).

38. Mortazavi, B., Dianat, A., Rahamana, O., Cuniberti, G. & Rabczuk, T. Borophene as an anode material for Ca, Mg, Na or Li ion storage: a first-principle study. *J. Power Sources* **329**, 456–461 (2016).

39. Patel, K., Roondhe, B., D.Dabhi, S. & K.Jha, P. A new flatland buddy as toxic gas scavenger: a first principles study. *J. Hazard. Mater.* **351**, 337–345 (2018).

40. Giannozzi, P. *et al.* Quantum Espresso: a modular and open-source software project for quantum simulations of materials. *J. Phys. Condens. Matter* **21**, 395502 (2009).

41. Perdew, J. P., Burke, K. & Ernzerhof, M. Generalized gradient approximation made simple. *Phys. Rev. Lett.* **77**, 3865–3868 (1996).

42. Grimme, S., Antony, J., Ehrlich, S. & Krieg, H. A consistent and accurate *ab initio* parametrization of density functional dispersion correction (DFT-D) for the 94 elements H-Pu. *J. Chem. Phys.* **132**, 154104 (2010).

43. Grimme, S., Ehrlich, S. & Goerigk, L. Effect of the damping function in dispersion corrected density functional theory. *J. Comput. Chem.* **32**, 1456–1465 (2011).

44. Grimme, S., Antony, J., Schwabe, T. & Mück-Lichtenfeld, C. Density functional theory with

dispersion corrections for supramolecular structures, aggregates, and complexes of (bio)organic molecules. *Org. Biomol. Chem.* **5**, 741–758 (2007).

45. Goerigk, L. *et al.* A look at the density functional theory zoo with the advanced GMTKN55 database for general main group thermochemistry, kinetics and noncovalent interactions. *Phys. Chem. Chem. Phys.* **19**, 32184–32215 (2017).

46. Blöchl, P. E. Projector augmented-wave method. *Phys. Rev. B* **50**, 17953–17979 (1994).

47. Monkhorst, H. J. & Pack, J. D. Special points for brillouin-zone integrations. *Phys. Rev. B* **13**, 5188–5192 (1976).

48. Peng, B. *et al.* Stability and strength of atomically thin borophene from first principles calculations. *Mater. Res. Lett.* **5**, 399–407 (2017).

49. Reed, A. E., Weinstock, R. B. & Weinhold, F. Natural population analysis. *J. Chem. Phys.* **83**, 735–746 (1985).

50. Schreckenbach, G. & Shamov, G. A. Theoretical actinide molecular science. *Acc. Chem. Res.* **43**, 19–29 (2010).

51. Shamov, G. A. & Schreckenbach, G. Theoretical study of the oxygen exchange in uranyl hydroxide.An old riddle solved? *J. Am. Chem. Soc.* **130**, 13735–13744 (2008).

52. Bühl, M. & Schreckenbach, G. Oxygen exchange in uranyl hydroxide via two "nonclassical" ions. *Inorg. Chem.* **49**, 3821–3827 (2010).

53. Grover, P., Ferch, L. & Schreckenbach, G. Adsorption of actinide (U-Pu) complexes on the silicene surface – a theoretical study. *Unpubl. Work* (2019).

54. Hu, W., Xia, N., Wu, X., Li, Z. & Yang, J. Silicene as a highly sensitive molecule sensor for NH3, NO and NO2. *Phys. Chem. Chem. Phys.* **16**, 6957 (2014).

55. Lin, X. & Ni, J. Much stronger binding of metal adatoms to silicene than to graphene: a first-principles study. *Phys. Rev. B* **86**, 075440 (2012).

56. Kaloni, T. P., Schreckenbach, G. & Freund, M. S. Large enhancement and tunable band gap in silicene by small organic molecule adsorption. *J. Phys. Chem. C* **118**, 23361–23367 (2014).

57. Sun, Y. *et al.* Adsorption and desorption of U(VI) on functionalized graphene oxides: a combined experimental and theoretical Study. *Environ. Sci. Technol.* **49**, 4255–4262 (2015).

58. Sun, Y. *et al.* Adsorption and desorption of U(VI) on functionalized graphene oxides: a combined experimental and theoretical study. *Environ. Sci. Technol.* **49**, 4255–4262 (2015).

59. Huang, C.-S., Murat, A., Babar, V., Montes, E. & Schwingenschlögl, U. Adsorption of the gas molecules NH 3 , NO, NO 2 , and CO on borophene. *J. Phys. Chem. C* **122**, 14665–14670 (2018).

60. Neidig, M. L., Clark, D. L. & Martin, R. L. Covalency in f-element complexes. *Coord. Chem. Rev.* **257**, 394–406 (2013).

61. Su, J. *et al.* Energy-degeneracy-driven covalency in actinide bonding. *J. Am. Chem. Soc.* **140**, 17977–17984 (2018).

Chapter 4 Appendix

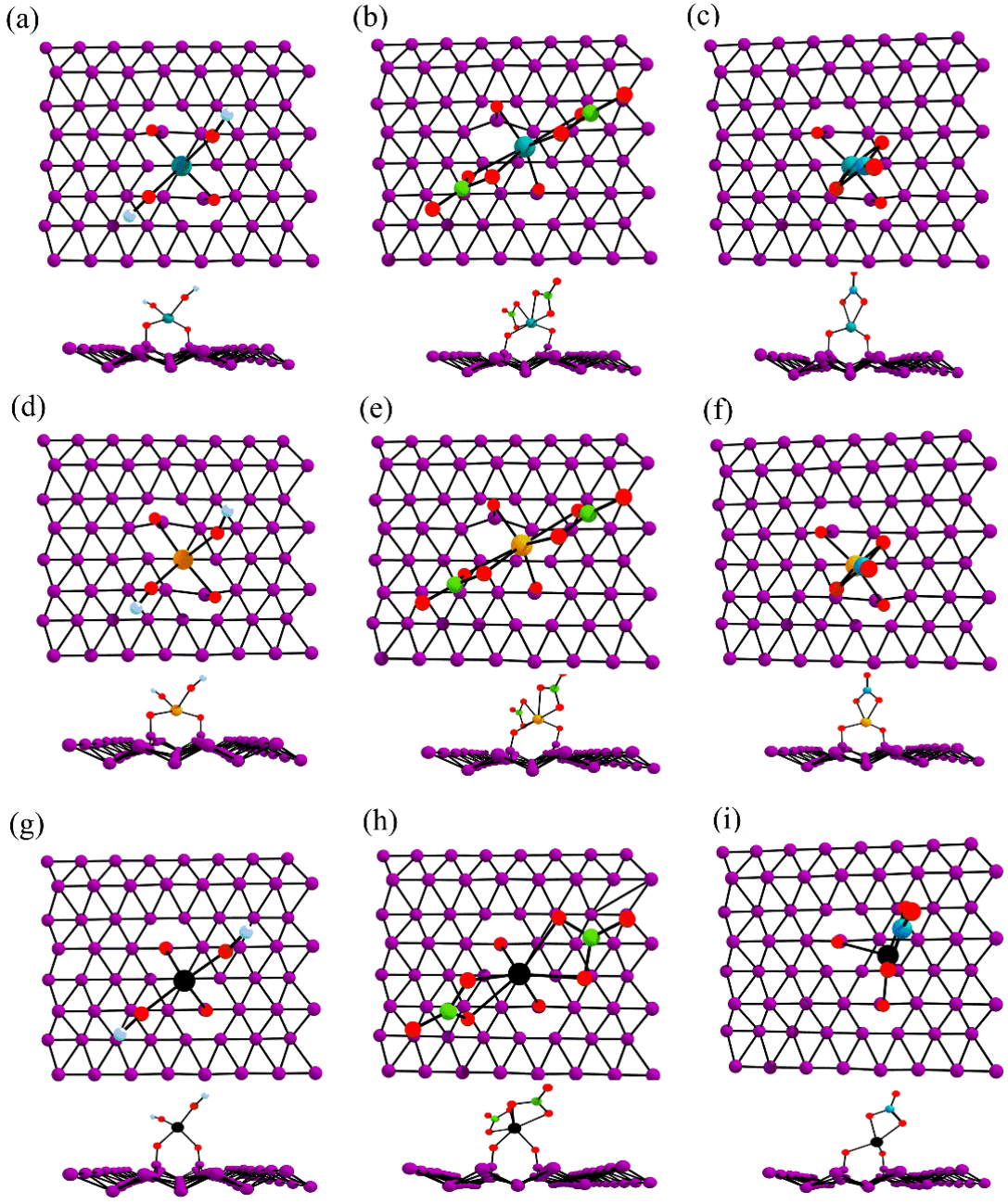

Figure B1 Side and top view of the most favoured sites for (a) $[UO_2(OH)_2]$, (b) $[UO_2(NO_3)_2]$, (c) $[UO_2(CO_3)]$, (d) $[NpO_2(OH)_2]$, (e) $[NpO_2(NO_3)_2]$, (f) $[NpO_2(CO_3)]$, (g) $[PuO_2(OH)_2]$, (h) $[PuO_2(NO_3)_2]$, and (i) $[PuO_2(CO_3)]$ adsorbed on N1 borophene.

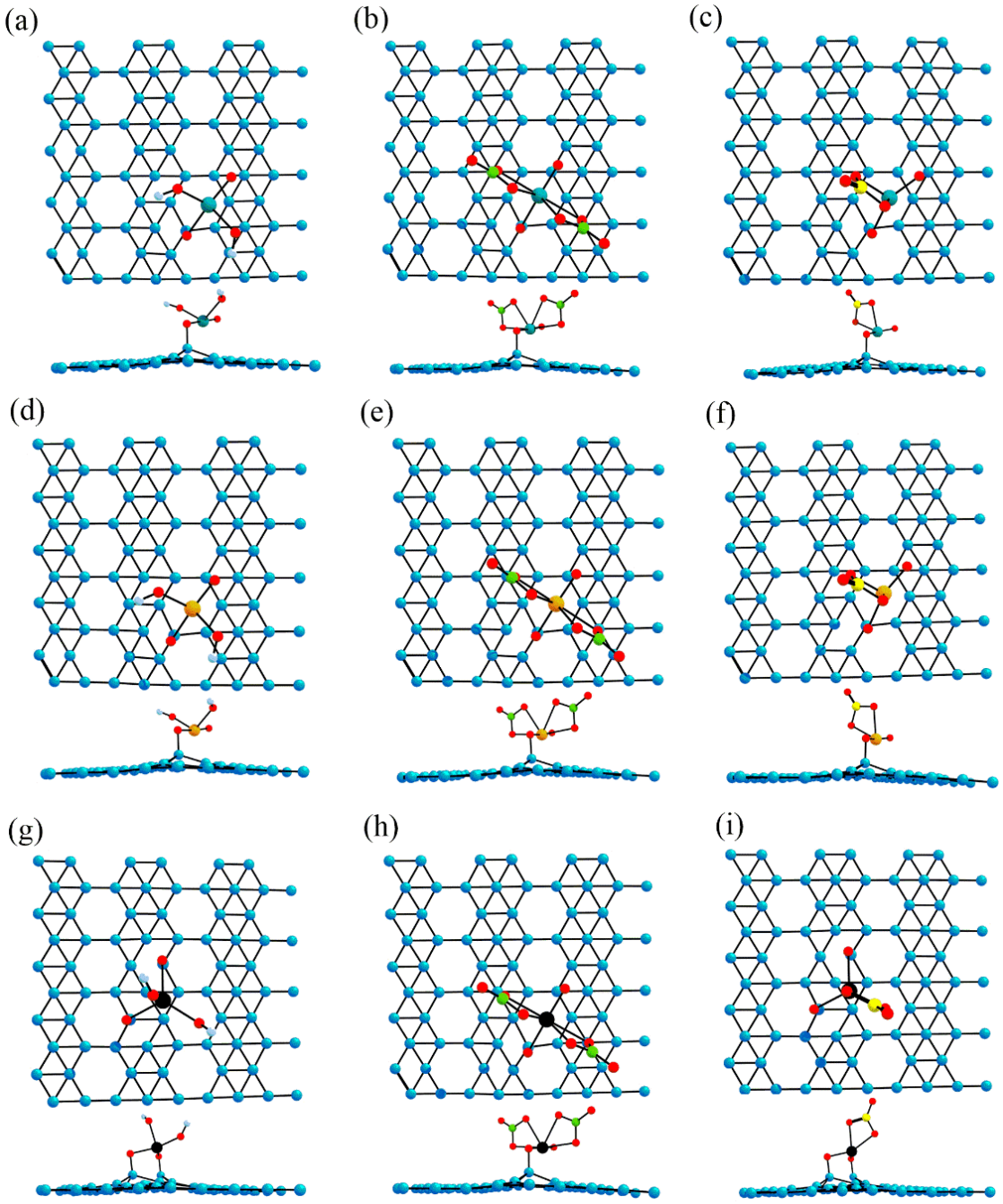

Figure B2 Side and top view of the most favoured sites for (a) $[UO_2(OH)_2]$, (b) $[UO_2(NO_3)_2]$, (c) $[UO_2(CO_3)]$, (d) $[NpO_2(OH)_2]$, (e) $[NpO_2(NO_3)_2]$, (f) $[NpO_2(CO_3)]$, (g) $[PuO_2(OH)_2]$, (h) $[PuO_2(NO_3)_2]$, and (i) $[PuO_2(CO_3)]$ adsorbed on N2 borophene.

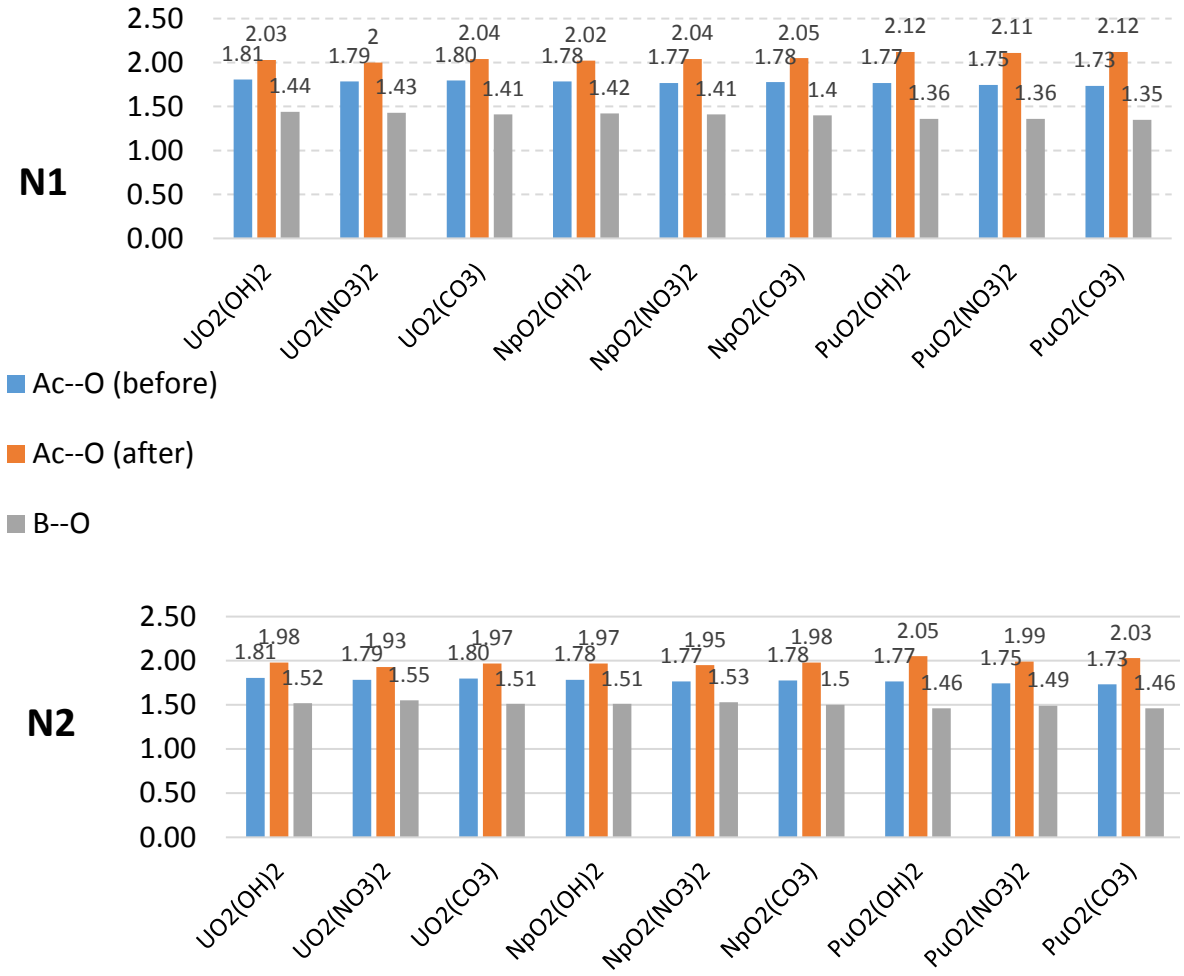

Figure B3 Bond length (in Å) comparison of M—O bonds before (blue) and after adsorption (red) where Ac = U, Np and Pu for N1 and N2 borophene. The bond lengths (in Å) of newly formed bonds between B and the oxo ligands of actinide complex are also included (green).

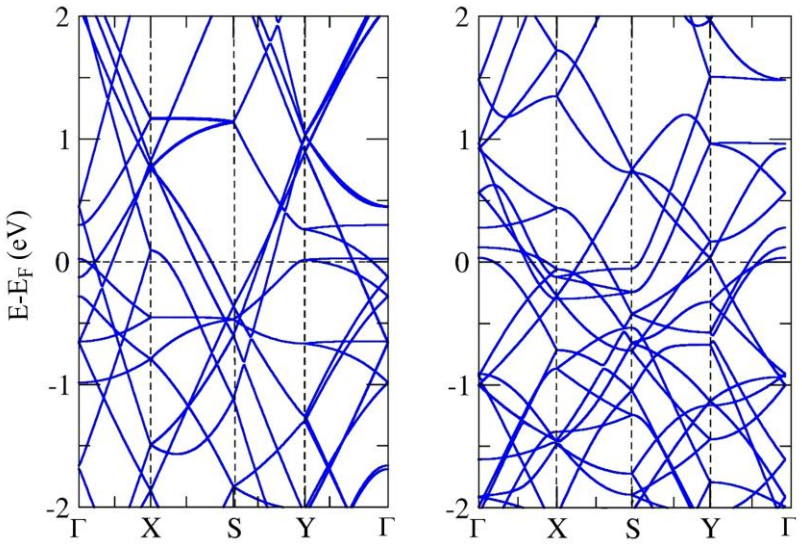

Figure B4 The electronic band structure diagrams for N1 (left) and N2 (right) pristine borophene supercell respectively at the GGA/PBE-D3BJ level with spin orbital coupling included.

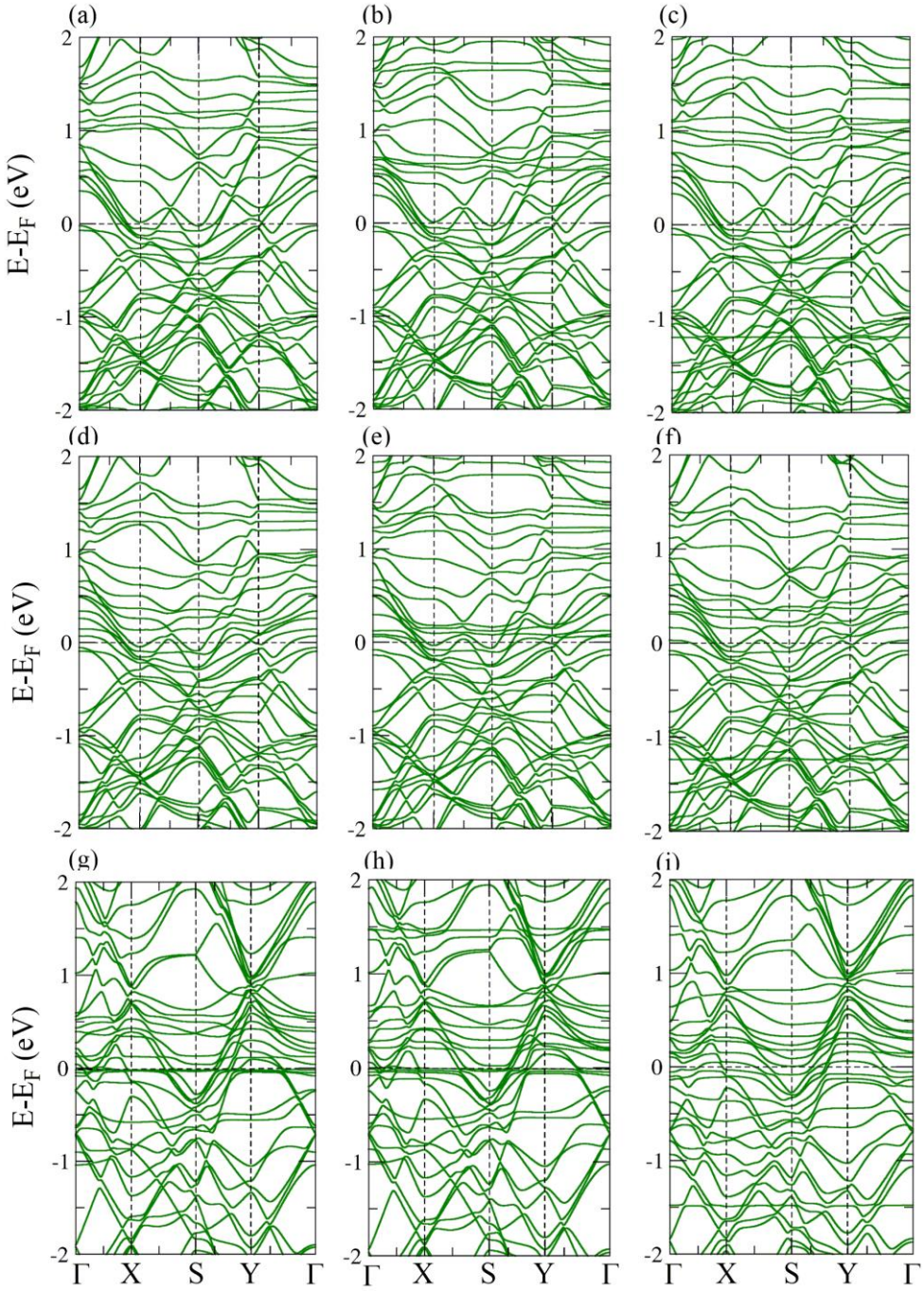

Figure B5 The electronic band structure diagram for the adsorption of (a) [$UO_2(OH)_2$], (b) [$UO_2(NO_3)_2$], (c) [$UO_2(CO_3)$], (d) [$NpO_2(OH)_2$], (e) [$NpO_2(NO_3)_2$], (f) [$NpO_2(CO_3)$], (g) [$PuO_2(OH)_2$], (h) [$PuO_2(NO_3)_2$], and (i) [$PuO_2(CO_3)$] on N1 borophene without spin-orbital coupling.

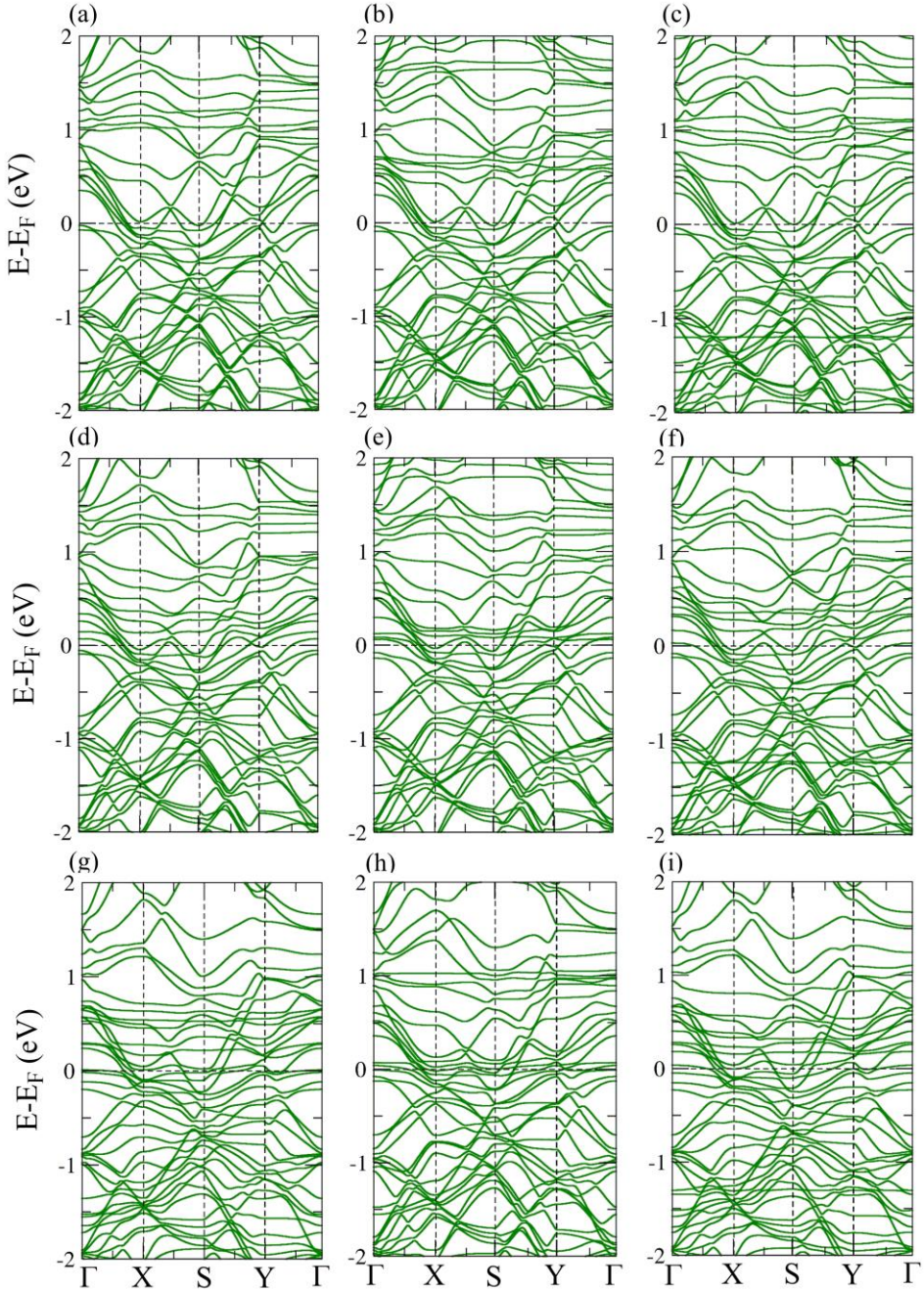

Figure B6 The electronic band structure diagram for the adsorption of (a) $[UO_2(OH)_2]$, (b) $[UO_2(NO_3)_2]$, (c) $[UO_2(CO_3)]$, (d) $[NpO_2(OH)_2]$, (e) $[NpO_2(NO_3)_2]$, (f) $[NpO_2(CO_3)]$, (g) $[PuO_2(OH)_2]$, (h) $[PuO_2(NO_3)_2]$, and (i) $[PuO_2(CO_3)]$ on N2 borophene.

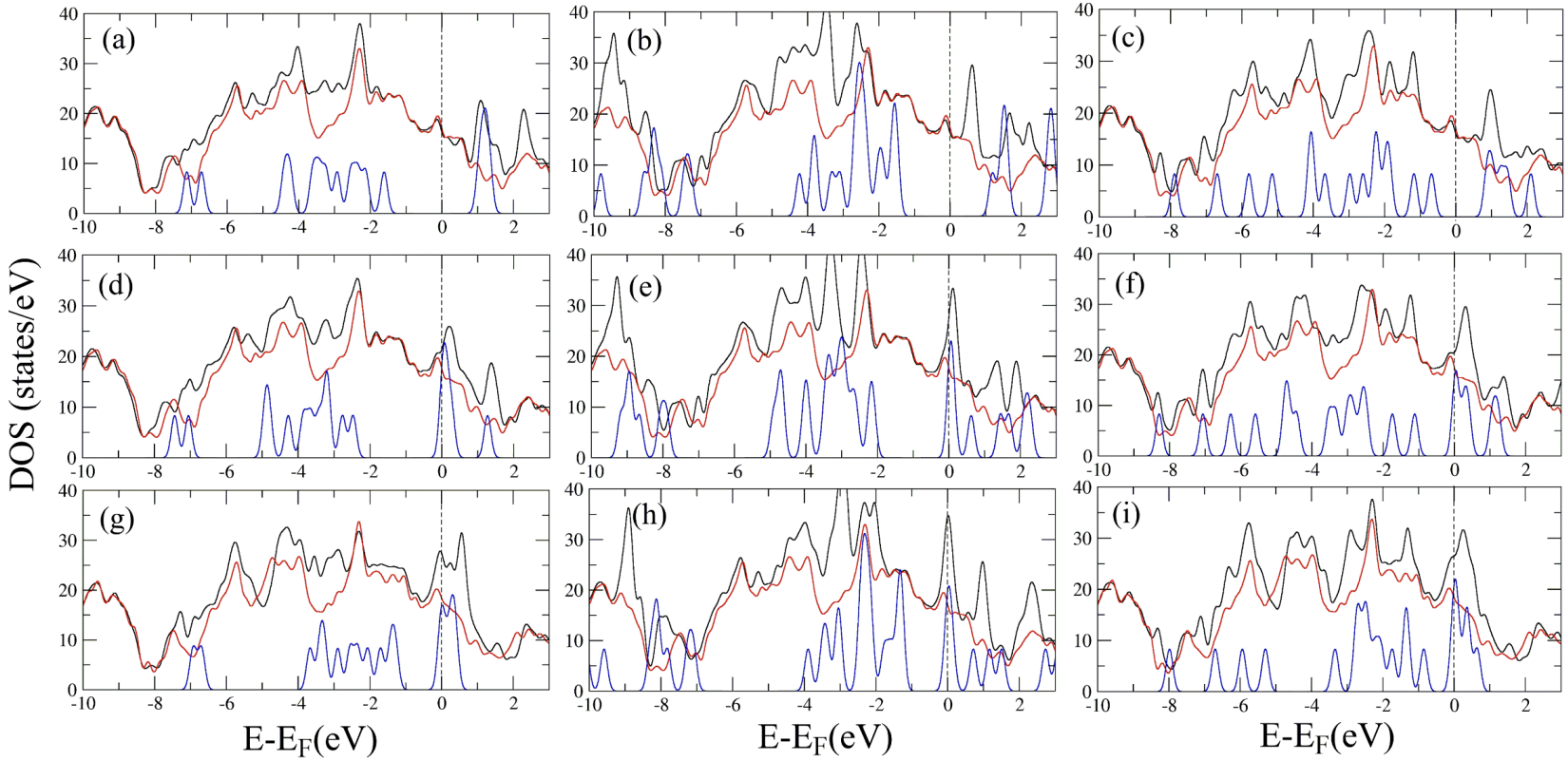

Figure B7 Density of states for (a) $[UO_2(OH)_2]$, (b) $[UO_2(NO_3)_2]$, (c) $[UO_2(CO_3)]$, (d) $[NpO_2(OH)_2]$, (e) $[NpO_2(NO_3)_2]$, (f) $[NpO_2(CO_3)]$, (g) $[PuO_2(OH)_2]$, (h) $[PuO_2(NO_3)_2]$, and (i) $[PuO_2(CO_3)]$ on N1 borophene. The black color stands for pristine N1 borophene supercell, red color represents N1 borophene with adsorbed actinide complex, and blue color shows contribution from adsorbed actinide complex. The Fermi level is set to zero.

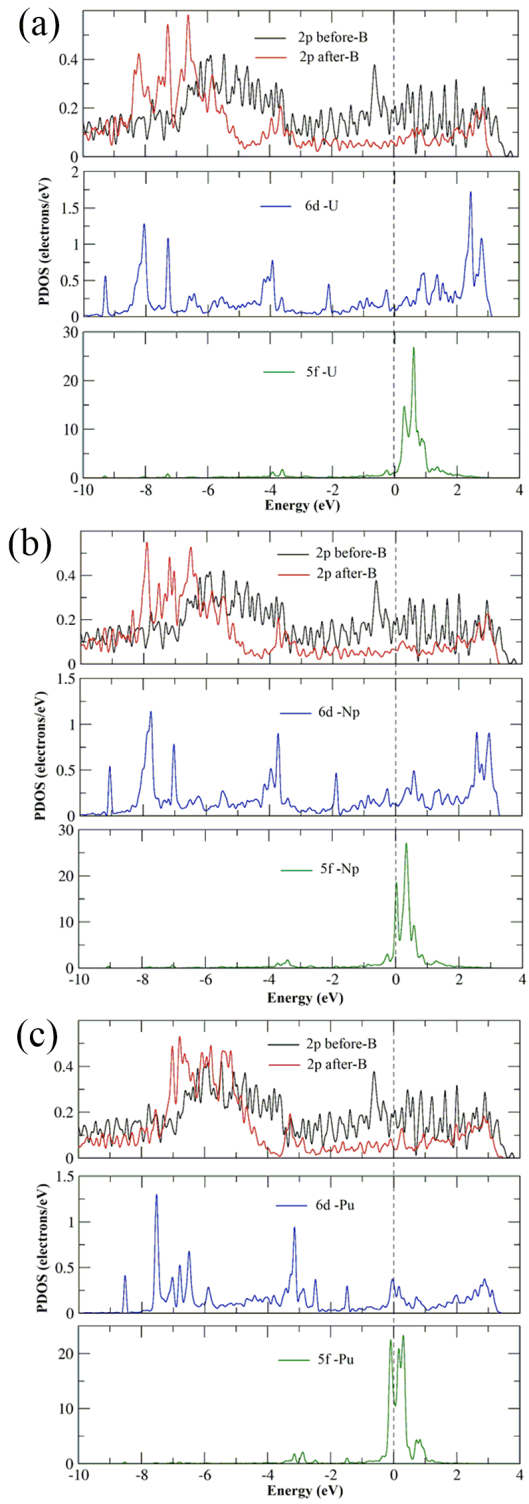

Figure B8 The partial density of states plots for the adsorption of (a) [$UO_2(CO_3)$], (b) [$NpO_2(CO_3)$], (c) [$PuO_2(CO_3)$] on N1 borophene.

N1 –Actinide complex	H-site	B1-site	O-site	A-site	Q
$UO_2(OH)_2$	-1.480	-1.459	-1.529	-1.432	3.21
$NpO_2(OH)_2$	-1.621	-1.605	-1.669	-1.579	3.32
$PuO_2(OH)_2$	-2.404	-2.393	-2.456	-2.362	3.54
$UO_2(NO_3)_2$	-0.824	-0.866	-0.809	-0.789	2.89
$NpO_2(NO_3)_2$	-0.906	-0.937	-0.890	-0.865	3.14
$PuO_2(NO_3)_2$	-1.609	-1.621	-1.663	-1.580	3.29
$UO_2(CO_3)$	-1.551	-1.539	-1.600	-1.510	3.27
$NpO_2(CO_3)$	-1.770	-1.758	-1.810	-1.735	3.43
$PuO_2(CO_3)$	-2.553	-2.584	-2.532	-2.508	3.60

Table B1 The adsorption energy in eV at the optimal sites of adsorption on N1 borophene after optimization in terms of position of central metal atom (H-site, B1-site, O-site, and A-site); amount of charge transfers Q (in electrons) from adsorbent to adsorbate for the most favourable cases.

N2 -Actinide complex	H1-site	B-site	P2-site	P3-site	Q
$UO_2(OH)_2$	-1.053	-1.028	-1.001	-0.974	4.31
$NpO_2(OH)_2$	-1.217	-1.176	-1.163	-1.131	4.39
$PuO_2(OH)_2$	-1.905 **H2**	-1.875	-1.854	-1.834	4.65
$UO_2(NO_3)_2$	-0.631	-0.595	-0.571	-0.543	4.18
$NpO_2(NO_3)_2$	-0.774	-0.735	-0.717	-0.684	4.23
$PuO_2(NO_3)_2$	-1.314	-1.272	-1.253	-1.228	4.57
$UO_2(CO_3)$	-1.185	-1.151	-1.135	-1.108	4.35
$NpO_2(CO_3)$	-1.257	-1.215	-1.192	-1.173	4.44
$PuO_2(CO_3)$	-1.955 **H2**	-1.914	-1.897	-1.867	4.78

Table B2 The adsorption energy in eV at the optimal sites of adsorption on N2 borophene after optimization named according to the position of central metal atom (H1-site, B-site, P2-site, and P3-site). There are two cases observed at H2-site for [$PuO_2(OH)_2$] and [$PuO_2(CO_3)$]; amount of charge transfers Q (in electrons) from adsorbent to adsorbate in the strongly adsorbed cases.

Chapter 5: Conclusions and Future Studies

5.1 Conclusions

Quantum chemistry methods such as DFT and band structure approaches were used to study and understand the interaction of heavy elements (actinides) with 2D materials (silicene, borophene, and germanene). The structural parameters, adsorption strengths and electronic properties of the systems were systematically investigated. For the complexes of the actinide elements uranium (U), neptunium (Np) and plutonium (Pu), ligands like CO_3^{2-}, NO_3^-, OH^- and the oxo ligand were chosen by considering the environment relevancy, as well as coordination number. Model systems were chosen in a way to have neutral complexes. Two models were investigated, the cluster model and the periodic model, to study the short-range and long-range interactions.

In the present studies, two different sizes of clusters for silicene were compared in Chapter 3 and only very minute differences in adsorption energies were observed so only one cluster size was considered for germanene. The inclusion of a cluster model with flake-size silicene i.e. $Si_{42}H_{16}$ and $Si_{64}H_{20}$ provided detailed information for the presence of bonding between Si and the -yl oxo ligands which leads to the reduction of the central metal from oxidation state +6 to +4. Because of the s charge transfer between the complexes and silicene, the formed Si—O bonds possess mainly an ionic character. For the germanene cluster, i.e. $Ge_{42}H_{16}$, weaker interactions between Ge and the –yl oxo ligand were observed in comparison to the other two surfaces included in this study. In silicene, there were two Si—O bonds present after adsorption whereas, in germanene only one weak Ge—O bond was seen. For silicene, the B-site is most favorable for carbonate complexes as well as for hydroxide complexes of Ac = U-Pu whereas the H-site is most suitable for strong

interactions for nitrate complexes of Ac = U-Pu (see Figure 3.2 for details). The H-site is highly stable for all the complexes adsorbed on germanene cluster. In a periodic model, the Si atom which is on the plane of silicene, i.e. the OP-site, has been found to have the strongest binding with the silicene in the case of hydroxide and carbonate complexes. The nitrate complexes show an affinity towards the sheet at the H-site again (see Table 3.5). The complexes adsorbed on the germanene supercell showed stable interactions at different sites without forming any specific pattern in terms of ligands. The B-site is most favorable for $[NpO_2(OH)_2]$, $[UO_2(NO_3)_2]$, $[NpO_2(NO_3)_2]$, and $[NpO_2(CO_3)]$. Only $[UO_2(OH)_2]$ binds strongly at OP-site whereas, $[PuO_2(OH)_2]$, $[PuO_2(NO_3)_2]$, $[PuO_2(CO_3)]$, and $[UO_2(CO_3)]$ showed most stable adsorption at H-site (see Figure 3.5).

In both types of models for silicene and germanene, the carbonate complexes show the strongest interactions with silicene/germanene followed by hydroxide complexes and nitrate complexes of actinides, which is a result of a combination of steric factors and ligand properties. In terms of periodic trends, Pu complexes are more strongly adsorbed as compared to Np and U complexes.

Electronic structure calculations were performed which result in a bandgap range from 0.130 to 0.300eV for the adsorption of actinide complexes on silicene. A comparatively smaller band gap opening was observed for the germanene surface with the range from 0.042 to 0.218 eV, whereas the band gap values in pristine silicene and germanene are 1.93 meV and 24.4 meV respectively. Density of States calculations show that the contribution of the nitrate complexes is small near the Fermi level but it is larger for the carbonate complexes in silicene's case. The strong adsorption and opening of a large gap at the Dirac point that has been found are of great potential for the use of silicene as a sensor for radioactive materials, although selectivity may still cause an issue.

The cluster model and periodic model are complementary to each other and hence, are of great importance. The cluster model includes a finite flake of 2D material which is useful to study short-

range interactions whereas the periodic model has an infinite sheet of 2D surface which accounts for long-range interactions. All kinds of analysis tools that exist in different molecular codes can be used for the cluster model. Also, the cluster model allows the bending of the 2D material which is not quite possible in the periodic model due to extremely large size (and hence, unfeasible) supercells. The inclusion of these two models in the present study has proven quite useful to check size dependency for the adsorption interactions. Importantly, the cluster model has generally not been as widely used for 2D materials.

For borophene, we performed a first-principles study to discuss the possibility and consequences of the interaction of actinide complexes with planar as well as buckled borophene in Chapter 4. Our results indicate that the two most favorable sites are the B1-site and O-site for adsorption on buckled (N1) borophene whereas the hollow sites (H1 and H2) are more suitable for planar (N2) borophene. The carbonate complexes have the largest adsorption energies followed by hydroxide and nitrate complexes. This can be again rationalized with simple arguments about steric factors and ligand binding strength. Periodic trends have been demonstrated with the strongest adsorption interactions shown by Pu complexes such as $[PuO_2(CO_3)]$ with an adsorption energy of -2.584 eV on N1 borophene. The formation of B—O bonds results in strong interactions which further leads to the reduction of the central metal from +6 to +4 oxidation state just like we observed on the silicene surface. We also systematically compared N1 and N2 borophene to investigate the effect of the presence of buckling on the binding interactions. According to our results, the presence of buckling in two-dimensional materials is a boost for strong adsorption interactions which is further useful for sensing technology.

These results are comparable with similar studies done on (buckled) silicene where strong adsorption interactions are present in case of silicene due to the presence of even stronger Si—O

bonds. In both silicene and borophene, similar trends in terms of central metal atom and ligands were observed. Remarkably high adsorption energies with large charge transfer from borophene to actinide complexes demonstrate the excellent ability of borophene to act as a sensor for radioactive material. On the other hand, the distortions occurring in the two-dimensional materials because of strong adsorption reduce the reusability of these sheets due to large structural changes as well as difficult removal of strongly adsorbed complexes and thus, require further detailed investigation. For the two dimensional sheets under study, silicene and borophene could potentially be employed for separation of radioactive waste, extraction of uranium from seawater, and similar applications.

5.2 Future Studies

The research in this particular field can be continued by considering the following possible ways:

1. Since our aim is to investigate the application of two-dimensional materials for the separation of radioactive waste as well as for the extraction of uranium from seawater in terms of strength of adsorption, the selectivity becomes really important. As only four ligands have been considered in the present study, this area can be expanded further by taking other types of ligands present in seawater or radioactive waste barrels into account. Results can be compared with the present calculations and trends can be modified.
2. In literature, almost 700 two-dimensional materials have been predicted to be stable and not all of them have been synthesized yet[1,2]. By using similar types of computational studies with the same complexes, other types of 2D materials such as stannene, phosphorene, antimonene, etc. can be tested and compared. They might have stronger chemisorption interactions compared to what we have obtained for silicene and borophene.

In addition, one could also go to completely different metals as well, again with the goal of sensing, or else for bandgap modulation.

3. In terms of functionals, we have investigated models with GGA-PBE. Other functionals such as hybrid-GGA or hybrid meta GGAs can be tested due to their relative good accuracy and efficiency, although, the computational cost will be really high as the systems are quite large.
4. For the cluster model, ionic complexes can be considered and compared with neutral complexes in terms of strength of binding. In the present case, only neutral complexes were taken as we were dealing with the periodic model as well.

Bibliography

1. Ashton, M., Paul, J., Sinnott, S. B. & Hennig, R. G. Topology-Scaling Identification of Layered Solids and Stable Exfoliated 2D Materials. *Phys. Rev. Lett.* **118**, 106101 (2017).
2. Mounet, N. *et al*. Two-dimensional materials from high-throughput computational exfoliation of experimentally known compounds. *Nat. Nanotechnol.* **13**, 246–252 (2018).